Characterization of Stress Gradients in Electroplated Nickel Thin Films

by

Yasin KILINÇ

A Thesis Submitted to the

Graduate School of Engineering

in Partial Fulfillment of the Requirements for

the Degree of

Master of Science

in

Mechanical Engineering

KOC University

August 2012

Koç University
Graduate School of Sciences and Engineering

This is to certify that I have examined this copy of a master's thesis by

Yasin KILINÇ

and have found that it is complete and satisfactory in all respects,
and that any and all revisions required by the final
examining committee have been made.

Committee Members:

_____
Dr. Erdem Alaca, (Advisor)

_____
Dr. Murat Sözer

_____
Dr. Uğur Ünal

Date: 15.08.2012

ABSTRACT

Nickel is a widely employed and thus well-studied material in the MEMS field due to its superior mechanical properties such as its high modulus of elasticity and corrosion resistance and magnetic properties. Among different deposition techniques of nickel, electroplating, as a well-studied and commercialized technique used in the fabrication process of macro- and as well as micro-devices, has various advantages including the ability to manipulate mechanical properties such as the modulus of elasticity and residual stress simply with deposition parameters.

Determination of residual stresses in thin films is necessary to optimize device performance and to lower fabrication costs. In addition to well-studied uniform residual stresses in thin films that control in-plane displacements, stress gradients that determine out-of-plane deflections of components need to be characterized to obtain straight microstructures designed as a moving part in a MEMS application.

The main contribution of this study to the literature is the systematic characterization of residual stress gradients of electroplated 1-μm-thick nickel films using microcantilevers as a measurement tool. This is achieved by varying electroplating parameters of applied current density and solution temperature in the range of 1 – 20 mA/cm^2 and 30 – 60 °C, respectively. Determination of cantilever tip deflections together with modulus of elastic measurements is performed to evaluate the residual stress gradients in nickel films. The modulus of elasticity of nickel is found to be in the range of 128,2 – 175,9 GPa, which is smaller than that of bulk nickel, approximately 200 GPa. Then the stress gradient of DC plated cantilevers is calculated to vary from 129.95 to -67.91 MPa/μm. Measurements indicate zero residual stress gradient, *i.e.* straight cantilevers, can be achieved at approximately 8 and 14 mA/cm^2 for the electroplating temperatures of 30 and 45 °C, respectively. However, there is no available current density within the investigated current density range leading to straight cantilevers at 60 °C electroplating temperature.

Microstructural analyses, consisting of XRD measurements of samples having different nickel film thicknesses and SEM morphology analysis of film surface and cross section are also employed to explore growing film characteristics.

ÖZET

Nikel elastisite modülü, korozyon direnci gibi üstün mekanik ve ayrıca manyetik özellikleri dolayısıyla MEMS alanında çok kullanılan ve çalışılan bir malzemedir. Birçok farklı nikel biriktirme tekniği içerisinde, elektrokimyasal kaplama makro ve mikro seviyede üretim aşamalarında kullanılabilen, iyi çalışılmış ve ticarileşmiş bir yöntem olarak birçok avantajının yanında üretim parametrelerini değiştirerek elastisite modülü ve artık gerilmeleri gibi mekanik özellikleri basitçe ayarlama yeteneği avantajına sahiptir.

İnce filmlerdeki artık gerilmelerin belirlenmesi, cihaz performansının optimizasyonu ve üretim maliyetlerinin düşürülmesi için gereklidir. İnce filmlerdeki düzlem içi yer değiştirmeleri kontrol eden düzgün artık gerilmelere ek olarak, parçaların düzlem dışı eğilmelerini belirleyen artık gerilme gradyanlarının karakterizasyonu, MEMS uygulamalarında hareketli parça olarak tasarlanan mikro-yapıların dosdoğru olarak üretilmesinde gereklidir.

Bu çalışmanın literatüre ana katkısı, bir ölçüm aracı olarak mikro-çubukları kullanarak, elektrokimyasal kaplanmış 1 μm kalınlığındaki nikel filmlerin artık gerilme gradyanlarının sistematik karakterizasyonudur. Bu ise, elektrokimyasal kaplama parametrelerinden akım yoğunluğu ve çözelti sıcaklığının sırasıyla 1 – 20 mA/cm^2 ve 30 – 60 °C aralığında değiştirilmesi ile sağlanmıştır. Nikel filmlerdeki artık gerilme gradyanlarının elde edilmesi, çubuk uç eğilmelerinin belirlenmesi ve elastisite modülü ölçümleri ile gerçekleştirilmiştir. Nikel elastisite modülü, yaklaşık 200 GPa olan yığın elastik modülünden küçük olarak 128,2 – 175,9 GPa aralığında bulunmuştur. Daha sonra DC-kaplanmış çubukların artık gerilme gradyanlarının, 129.95 ile -67.91 MPa/μm aralığında değiştiği hesaplanmıştır. Ölçümler, 30 ve 45 °C elektrokaplama banyo sıcaklıkları için sırasıyla 8 ve 14 mA/cm^2 akım yoğunluklarında sıfır artık gerilme gradyanına yani düzgün çubuklara ulaşılabileceğini göstermektedir. Buna karşılık, 60 °C elektrokaplama banyo sıcaklığı için çalışılan akım yoğunluğu aralığında düzgün çubuk üretilmesine yol açan uygun bir akım yoğunluğu bulunamamıştır.

Farklı nikel film kalınlığına sahip numunelerin XRD ölçümlerini ve film yüzeylerinin ve ara kesitlerinin SEM morfoloji analizlerini içeren mikro-yapı analizleri büyüyen nikel film karakteristiklerinin araştırmak için kullanılmıştır.

TABLE OF CONTENTS

ACKNOWLEDGEMENT

I should first express my gratitude to Dr. Erdem Alaca as my primary mentor for his continuous support and guidance with his famous encouraging, ever-positive attitude. I am also thankful to Dr. Murat Sözer and Dr. Uğur Ünal for taking a part in my thesis committee.

I consider myself lucky to study in the Biosensor project beginning right after my graduate studies together with Dr. Erdem Alaca, Dr. Hakan Ürey, Dr. Halil Kavaklı, Dr. Çağlar Elbüken, Dr. İbrahim Barış, Erhan Ermek, Onur Çakmak and other past and present members of the project. It was always a pleasure for me to take part in the Biosensor project and discuss mechanical, electrical and biological aspects of MEMS in weekly meetings.

I should especially present my thanks to Erhan Ermek for his ever-kind behaviors and his help to constitute the modulus of elasticity measurement setup up-and-running in the OML lab. Erhan's assistance together with Sven to familiarize myself to the WLI device to perform cantilever deflection measurements is also greatly appreciated.

Assistances of Dr. Melis Şerefoğlu and Dr. Uğur Ünal in preparation and examination of samples for microstructural analyses are needed to be highlighted too. Dr. Özgür Birer's help in EDS analysis of nickel films should also be mentioned. I am also grateful to Dr. Levent Demirel and Dr. Annamaria Miko for their counsels on electroplating and letting me use the pulse plating equipment.

Assistances of my colleagues from Mechanical Characterization Lab including Evren Arkan, Serhat Yavuz, Gökhan Nadar, İsmail Yorulmaz, Berkay Gümüş, Zuhal Taşdemir are always greatly welcomed.

KUYTAM facilities were employed to perform microstructural analyses of nickel films using XRD, SEM, metallographic polishing machine and diamond saw equipment.

Last but not least, doubtless and continuous support and belief of my family in me are beyond any gratitude.

This work was supported by TUBITAK under grant number 109E222 and 111E184.

LIST OF FIGURES

Chapter 1: Introduction

The evolution of microelectromechanical systems (MEMS) and devices accelerated with novel design concepts and new processing techniques together with the expansion of the set of MEMS materials introduces the increased functionality (such as mechanical, electronic, magnetic, optical, electrochemical, and biological) and enhanced performance of MEMS devices. These materials include metals and alloys (nickel, aluminum, gold, copper, chromium, shape memory alloys etc.), ceramics (silicon carbide [10], zirconia, zinc oxide, SiCN etc.), and polymers (such as polyimide [11]) in addition to traditional frequently used silicon [12-16].

The employment of a material requires the accurate knowledge of its properties. A sufficiently comprehensive understanding of length-scale-dependent and process-dependent mechanical properties of microstructures ensures the successful fabrication and reliable operation of them. This understanding is built on the accurate measurements of material properties of these microscale structures.

The mechanical properties of interest of microscale structures and materials include the modulus of elasticity (E), the Poisson's ratio (υ), the yield strength (σ_Y), and the fracture strength (σ_F), residual stresses (σ_R) and residual stress gradients ($\nabla\sigma_R$).

In contrast to the standard techniques developed for macroscale mechanical tests, there is no prevailing method for the characterization of microstructures. As a result, many different microscale mechanical test techniques including the tension test, bending tests (such as axisymmetric plate bending, microbeam bending, bulge test, M-test and wafer curvature tests), dynamic (resonant) tests and the fabrication of passive strain sensors, nanoindentation, Raman spectroscopy etc. as described in several review articles [17-21] are employed to identify the material properties of interest.

Though MEMS structures form a huge and expanding design space, it is convenient to categorize structures as being either freestanding (single or double clamped beams, free-free beams etc.) or constrained. The scope of this work is limited only to the metallic or metal alloyed, single or multiple layered, single clamped (one-end-fixed) micro-beams, *i.e.* cantilevers.

Since our research is focused on dynamic-mode operation of Ni microcantilevers employed as a mass sensor for the detection of biomolecules on air or in liquid media, thus this chapter investigates the applications of metallic cantilevers with a special emphasis on Ni cantilevers.

Thus this part further divided into following four sections reviews applications of single-layer nickel and other metallic microcantilevers followed by those of nickel containing multilayer beams and other metallic cantilevers.

Each of the reviewed articles is considered with reference to: (i) experimental results of the characterization of mechanical properties of microcantilevers or MEMS microcantilever applications, (ii) fabrication method of microcantilevers, and (iii) experimental setup.

1.1 Single-Layer Ni Microcantilevers

In this subsection, some MEMS applications of single-layer nickel microcantilevers will be reviewed.

Majjad, H. *et al.* [22] characterized the modulus of elasticity of nickel microcantilevers fabricated with LIGA by measurements of resonance frequencies of in-plane and out-of-plane flexural modes with an optical setup. Resonance frequency measurements of first four in-plane and out-of-plane flexural modes were compared to an elastic finite element model. The variation of the boundary condition of the clamped part of the finite element model (FEM) was performed to match resonance frequencies of the FEM beam model to experimental values. This correlation resulted in the determination of the modulus of elasticity. The modulus of elasticity -determined to be isotropic - was computed as 195 GPa.

Nickel electrodeposition was performed at 50 ^{o}C while pH and current density were adjusted to 4 and 7 mA/cm^2. The length, width and thickness of a fabricated cantilever were 4.9 mm, 400 μm and 200 μm, respectively. A piezoelectric stage was employed to actuate fabricated beams. Deflection measurement of cantilevers was carried out using a Laser Doppler Vibrometer (LDV) setup. Experimental setup used to determine flexural resonance modes for fabricated cantilever can be seen in Figure 1.1. A laser beam scanned along a microcantilever was employed to determine resonance modes.

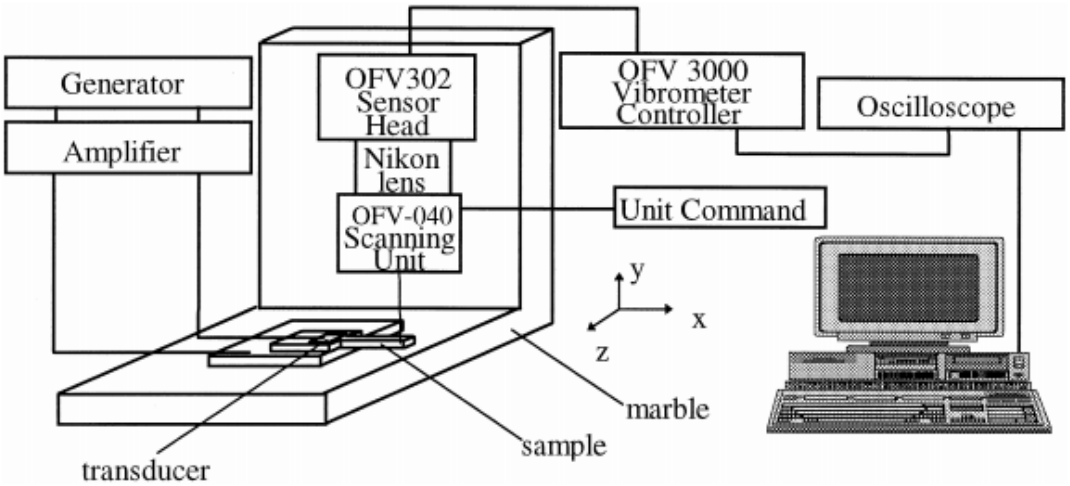

Figure 1.1: Experimental setup used to determine vibration characteristic of electroplated Ni cantilevers [22]

Fritz, T. *et al.* [23] investigated the influence of the deposition parameters and substrate layer on texture and structure of electroplated nickel layers. 15 µm thick nickel layers were characterized using pulse plating on evaporated gold or electroplated copper substrates. Nickel electroplating was employed in a nickel sulfamate-based electrolyte whose pH and temperature were adjusted to 3.2 and 40 ^{o}C, respectively. In the electrolyte, bromide instead of chloride was preferred for anode activation. Furthermore, the wetting agent of Microfab NI-110 Stressreducer of the concentration of 5 ml/l was included in the electrolyte. For comparison, dc plating was also carried out with a mean current density of 10 mA / cm^2.

X-ray diffractometry (XRD) measurements performed to determine the preferred orientation of the electroplated nickel layers demonstrated that the texture of deposited nickel layers shifted from a (110) texture at a low mean current density of 2.5 mA/cm^2 to a (100) texture at a high mean current density of 20 mA/cm^2.

Microstructural analyses carried out with scanning electron microscope (SEM) of polished and etched cross sections revealed that the structure changed from a columnar to granular nature as current density increased on the gold substrate. Unlike gold substrate, the deposited nickel layers on the copper substrate showed a granular structure even at low mean current densities. This difference in the structure of electroplated nickel layer indicates the importance of substrate on growing mechanism of thin layers. Amblard, J. *et al.* [24] provided a possible mechanism for this texture evolution in a nickel sulfate electrolyte. The preferential growth of (110) texture at low current densities is related to the inhibition mechanism caused by the adsorbed hydrogen in an electroplated layer. Diminishing of this effect with increasing current densities results in the (100) texture in electroplated layers.

According to Abel, S. [25], especially low current densities promote hydrogen absorption. Hydrogen inhibits the (110) growth direction to a less extent than any other species. Therefore the weakening of the influence of hydrogen adsorption by increasing the mean current density results in a promotion of the uninhibited growth. Inhibition mechanism claimed for Watts's type electrolyte seems reasonable for the nickel sulfamate electrolyte, too.

Fritz, T. *et al.* [23] also discussed the substrate effect on growing film characteristics. For low current densities, promotion of a strong (110) texture in the nickel layer is related to (111) oriented texture of the substrate gold due to large lattice mismatch between gold and nickel. Layer growth mechanism shifts from instantaneous nucleation and growth mechanisms at low current densities to a progressive nucleation mechanism while the current density is increasing. The influence of the substrate introduced into the initial seeds of a growing layer decays as the current density keeps rising [26].

Fritz, T. *et al.* [27] determined the modulus of elasticity of electroplated nickel using an identical fabrication setup by a comparison of different measuring techniques including laser-acoustic method, microindentation test and resonance frequency measurements of laterally and vertically swinging cantilevers. The modulus of elasticity decreases from 205 GPa to 165 GPa as the applied current density shifted from 2 mA/cm^2 to 20 mA/cm^2 was determined. This variation in the modulus of elasticity of electroplated nickel was attributed to texture effects.

For laterally swinging cantilevers, cantilevers were designed with a thickness of 25 μm, a length of about 700 μm and two widths of 19.5 or 28.5 μm. The geometry of the fabricated laterally swinging structures is shown in Figure 1.2. 10-μm-thick vertically swinging nickel cantilevers with a width of 100 μm and length varying from 380 to 1200 μm were deposited using mean current densities of 2.5 and 20 mA/cm^2. For laterally swinging cantilevers, electrostatic actuation and LDV detection were utilized. Unlike electrostatically excited laterally swinging cantilevers, vertically swinging cantilevers were acoustically excited by ultrasound of a piezo speaker. In order to investigate substrate effect on the properties of electroplated nickel, isotropic copper and <111> oriented vapor deposited gold were used. The modulus of elasticity values were found to be independent of the substrates used. Evolution of nickel microstructure and layer texture with the current density are consistent with the results of the previous work by Fritz, T. *et al.* [23] summarized above.

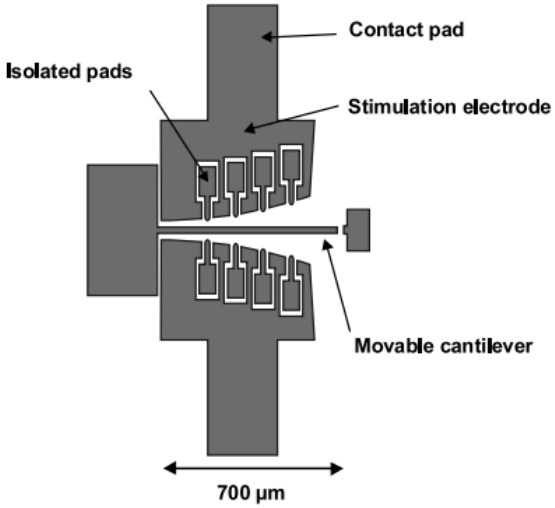

Figure 1.2: Schematic representation of an electrostatically actuated and laterally swinging nickel cantilever [27]

Larsen, K. *et al.* [28] developed in situ bending devices with integrated electrostatic actuator for fatigue test measurements by electroplating nanocrystalline nickel. Life tests considering the evolution of pull-in voltages resulted in good fatigue properties of nanocrystalline nickel. Pull-in voltage variation was considered as mechanical changes of the test beam resulted from fatigue or creep mechanism. The length of beams varied from 7 to 30 µm. Slightly trapezoid cross section resulted in variation from 2.0 to 3.5 µm in the width of beams. Ni beams with a thickness of 7 µm electroplated from a sulfamate bath at 40 ^{o} C using current density of 30 mA / cm^2 resulted in a grain size of 50 – 100 nm. Testing of the devices by a probe station resulted in pull-in voltages of approximately 250 and 190 V for beams with FEM estimated maximum stresses of 2100 and 470 MPa, respectively.

Hsu, C. *et al.* [29] investigated the modulus of elasticity of electroplated Ni thin films by a nanoindentation system used to perform microcantilever bending tests. The length of cantilevers varied from 20 µm to 150 µm while the width and thickness of them were kept constant at 8 µm and 11 µm, respectively. A microcantilever bending test was carried out at five different positions along a fabricated beam length for each 150 µm long cantilever.

Bulk silicon etching by N_2H_4 resulted in approximately 4 µm undercut of (111) planes leading to significant deviations of the boundary condition of fabricated beams from ideal clamped cantilever boundary condition. A conventional indentation test was used on an unreleased film to evaluate the penetration depth of a suspended cantilever. Boundary effect was also examined with an FEM model.

Consideration of the indentation of films during a cantilever bending test and boundary effects resulted in more accurate modulus of elasticity measurements. The range of modulus of elasticity shifted from 69 – 193 GPa to 237 – 242 GPa by considering the boundary and indentation effects. Therefore the variation of the elastic modulus with the loading location on a cantilever was minimized. Measurements of the modulus of elasticity with a conventional nanoindentation device revealed a different modulus of elasticity of 271 GPa.

1.2 Other Single-Layer Elemental or Alloy Microcantilevers

In the literature, other metallic materials such as gold, aluminum and chromium etc. are frequently reported in single-layer cantilever applications. The following text covers some of those representative studies.

One of the first works with metallic cantilevers was carried out by Nathanson, H. C. *et al.* [30]. A resonant gate transistor (RGT) having a miniature Au cantilever resonator were fabricated by means of planar integrated circuit technology. The fabricated RGT with the geometry and circuit connections are shown in the Figure 1.3. Electrostatic actuation to induce vibrations of a cantilever resonator was employed in the input transducer. Vibrations of a cantilever lead to variations in the polarization field which is perceived by a surface field effect transistor. Cantilever resonators fabricated with gold electrodeposition onto a temporary metal spacey layer that was later etched away. Availability and low electroplating stresses were among the reasons for the choice of gold as a cantilever material.

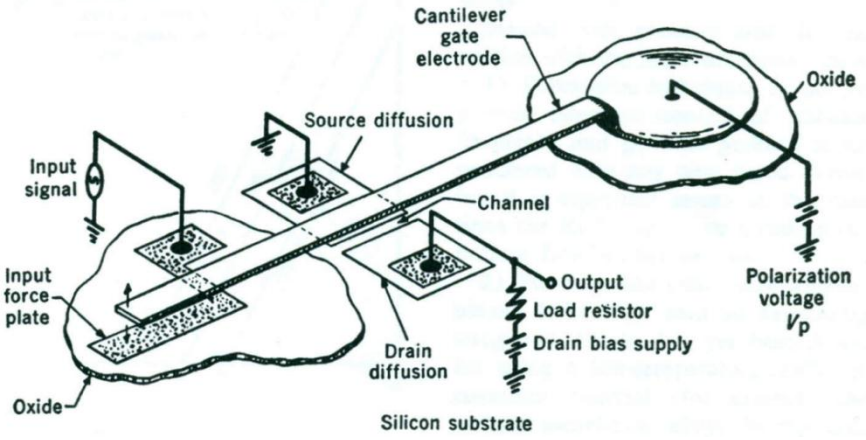

Figure 1.3: Schematic diagram of the resonant gate transistor developed by Nathanson, H. C. *et al.* [30]

Son, D. *et al.* [31] characterized the modulus of elasticity and yield strength of DC magnetron sputtered Al and e-beam evaporated Au thin films of various thicknesses and lengths by using a microcantilever beam-bending technique. Beams fabricated by silicon bulk micromachining were loaded by a nanoindenter. From simultaneously obtained displacement data, load-displacement curves were constituted. In the study, the effect of the surface on mechanical properties of a thin film was discussed and yield strength behavior was examined with a microstructure effect using a modified misfit dislocation theory.

The width of the fabricated beams was 20 μm and beams varied in length from 20 μm to 90 μm in intervals of 10 μm. The thicknesses of fabricated beams were 0.51, 1.03 and 1.50 μm for Al beams and 0.56, 0.99 and 1.26 μm for Au cantilevers. Microstructural analyses were carried out by atomic force microscopy and mean grain size was calculated.

The modulus of elasticity was found to be independent of film thickness. The average modulus of elasticity was determined in the 77.6 – 80.9 GPa range for Al films and in the 107.2 – 130.3 GPa range for Au films with an approximately 10 GPa standard deviation for each film thickness. Results implied that yield strength of the both films increased with decreasing film thickness and their values were much larger than the corresponding bulk values.

The grain sizes of the films were found proportional to their film thickness. While grain size measurements for Au films indicated a good agreement with Hall-Petch behavior, in Al films the Hall-Petch equation cannot account for the dependency of yield strength on grain size. Native oxide layer on Al beams was believed to be responsible for this deviation. The yield strength of Al thin films was explained with the modified misfit dislocation theory where the substrate effect was changed with a surface oxide effect to constrain dislocation movements.

Chakraborty, A. *et al.* [3] fabricated 40 nm thick Al and 70 nm thick Au cantilevers of lengths from 5 to 9 μm and widths in the range of 200-300 nm by thermal evaporation or sputtering. In order to release fabricated Al and Au cantilevers, DRIE was employed as a dry etching technique. A scanning electron microscope was employed to determine the deflection profiles of cantilevers.

In this work, local curvature variations according to deflection profile shifts based on surface stresses induced due to rapid thermal oxidation along the length of the short Al

cantilevers of lengths below 9 µm and oxidized spots were calculated. The fabricated Al cantilevers were subjected to rapid thermal oxidation process at 300 ^{O}C for a total time of 240 s. The thickness of the grown Al oxide was measured approximately 6 nm from ellipsometric analysis of the samples.

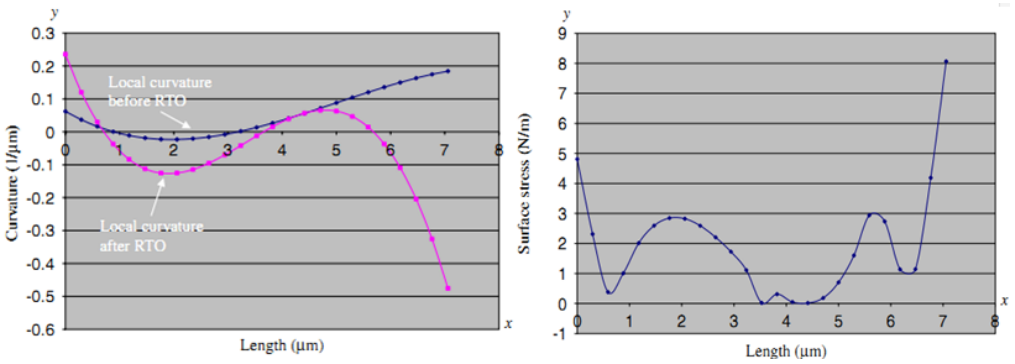

Figure 1.4: Developed oxidation induced nonlinear surface stresses together with cantilever profiles before and after oxidation process [3]

Stoney equation was employed to evaluate the oxidation induced surface stress on Al cantilevers. In the most general and expected case, the adsorption of molecules along the length of the cantilever would not be uniform. Hence knowledge of resonant frequency shift or static deflection of the cantilever's free end becomes insufficient to predict the amount of absorbed molecules precisely. The surface profiles of a cantilever utilized to determine the curvature shift at each point on the cantilever were employed to specify the surface stress as well as the oxidized spots during the oxidation. SEM pictures of cantilevers processed by pixel transformation by commercial software were used to evaluate curvature shifts.

From the comparison of deflection profiles of Al cantilevers before and after the rapid thermal oxidation process, highest local curvature shifts calculated towards the free end of the cantilever and considerable changes towards the free end of the Al cantilever were obtained. Curvature profiles before and after RTO and resulting non-uniform surface stress distribution can be seen in Figure 1.4. This non-uniform stress distribution revealed different oxide thicknesses along the length of cantilevers.

Fang, W. *et al.* [32] investigated the coefficient of thermal expansion (CTE) of thin films through analytical and experimental means using micromachined beams. The thermal expansions of the thin films were studied with both single and bilayer heat-deformed micromachined cantilevers showing out of plane deflection after subjected to temperature changes. According to results from finite element analysis, empirical representations of CTE

of a thin film for both single and bilayer cantilevers and other mechanical properties were formulated. So the CTE values of a thin single layer and bilayer film were determined with the measured angular deflection and the radius of curvature of a microcantilever respectively. As an illustrative application, the single layer microcantilever approach was utilized first to find the CTE of thermally grown SiO_2 cantilevers having lengths between 40 and 200 μm and thicknesses ranging from 1.07 to 1.13 μm. Then the bilayer microcantilever approach was employed to measure the CTE of aluminum films that formed a bilayer microcantilever with SiO_2 film. With thermal evaporation, a 0.5 μm thick aluminum film was deposited on SiO_2 cantilevers. The CTE of the SiO_2 film was determined as 0.25 10^{-6} / ^{O}C within temperature range of 30 – 100 ^{O}C. The CTE of Al film was evaluated 20.30 10^{-6} / ^{O}C within temperature range of 30 – 90 ^{O}C. The both CTE values for thin film materials were found smaller than the corresponding bulk values found in the literature.

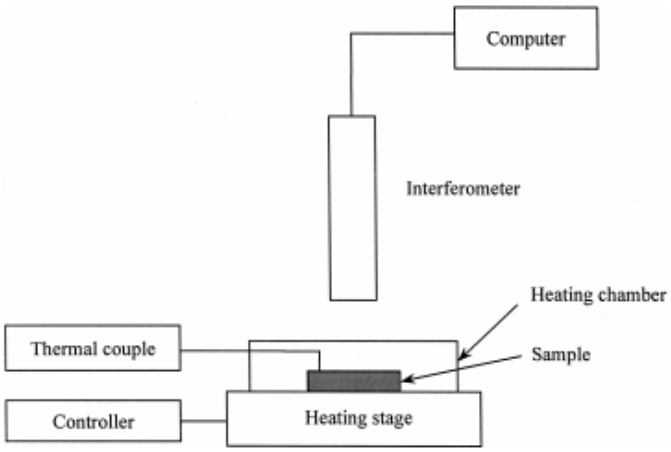

Figure 1.5: Schematic representation of the experimental setup fort CTE determination of thin films [32]

The measurement setup consisting of a heating stage with a controller keeping deviations in the sample temperatures less than 0.1 ^{O}C, a thermal couple to monitor the silicon substrate temperature and an optical interferometer identifying of the deflection profile of s microcantilever can be seen in Figure 1.5. In the study, it was also pointed out that due to creep effect resulted from residual stresses and thermal loading, deformations of a cantilever can change with time. So the measurements conducted immediately after a sample attained a designated temperature was proposed to reduce the creep effect.

Lee, S. *et al.* [33] measured elastic properties and yield strength of Al thin films with an electrostatically actuated test device shown in Figure 1.6. Loading to suspended thin films was carried out by electrostatically actuated comb drives. A high resolution optical microscope fitted with a CCD camera was employed for displacement measurements together

with an image analyzer. The extracted linear load-displacement behavior of the suspended beams analyzed to evaluate the elastic modulus of thin Al films.

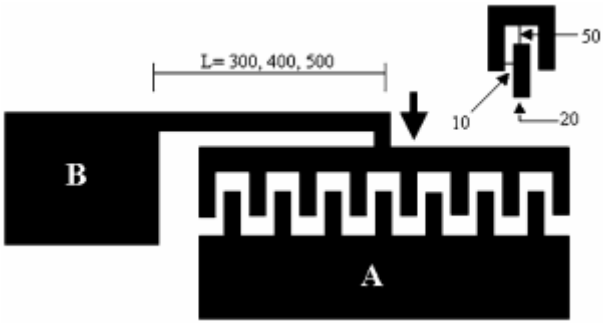

Figure 1.6: Schematic drawing of a suspended beam electrostatically actuated with comb drives [33]

Lateral movement for a suspended beam was acquired by sacrificial layer removal technique by oxygen-based dry etching with polyimide. The 2 µm thick Al layers were DC magnetron sputtered on top of the polyimide sacrificial layer. Beams with lengths of 300, 400 or 500 µm were fabricated. The load-displacement curves of DC electrostatic actuated Al beams were obtained with a probe-station system.

The elastic modulus obtained from slopes of the load-displacement curve was found as 75 ± 3 GPa and independent of the length of Al beams.

Petersen, K. E. *et al.* [34] demonstrated the application of the resonance frequency measurements to determine the elastic modulus of thin films for the first time. A number of thin cantilevers including SiO_2, S_3N_4, Corning 7059 borosilicate glass, Nb_2O_5 and Cr were fabricated by several deposition methods. Moduli of elasticity of these materials were calculated using transverse resonant frequency measurements of electrostatically actuated cantilevers. Cr beams were sputtered in an argon atmosphere with substrates at room temperature.

The experimental setup consisted of a He-Ne laser and detector. The resonant frequency was extracted from the data of the amplitude of the light as a function of frequency. The modulus of elasticity of Cr layers was found as 180 GPa.

Nilsson, S. *et al.* [35] investigated thin evaporated chromium cantilevers with sub-100 nm thickness by atomic force microscope. In the study, cantilevers having thicknesses of 68 ± 3 and 83 ± 3 nm and a length of 3 µm were fabricated. The fabrication flow consisted of electron beam lithography, metal lift off and subsequent reactive ion etching (RIE) processes.

Mechanical properties including the modulus of elasticity of the fabricated Cr nanocantilevers were determined as a function of their length by an AFM operating in contact mode. By applying incremental forces (ΔF), the corresponding incremental change in deflection (δz) was tracked.

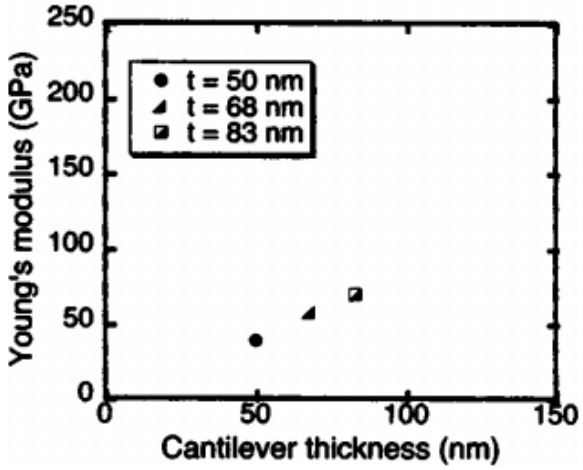

Figure 1.7: The effective modulus of elasticity as a function of Cr thickness [35]

The results imply that the effective modulus of elasticity clearly changed as a function of cantilever thickness and there was a decrease in modulus of elasticity as the thickness decreases (Figure 1.7).

Zhou, Z. M. *et al.* [36] fabricated 75 nm thick sputtered Cr microbridge and microcantilever structures to measure residual strains. According to profile of the buckled beams by using the interference technique with an optical profiling system, gradient residual strain and residual uniform strain was determined for microcantilever and microbridge samples respectively. The residual uniform and gradient strain in the Cr film were measured as 4.96 10^{-3} and -4.2967 10^{-5} respectively. The model developed by Fang and Wickert was used to evaluate a uniform strain in microbridge structures.

Zhang, J. [37] measured the modulus of elasticity of electroplated Ni/Fe microcantilevers and (110)-oriented silicon by a simple method called balance method which is seen schematically in Figure 1.8. The developed technique is a variant of bending method based on balance. UV-LIGA was employed to produce Ni/Fe cantilever beams with different Ni/Fe mole ratios.

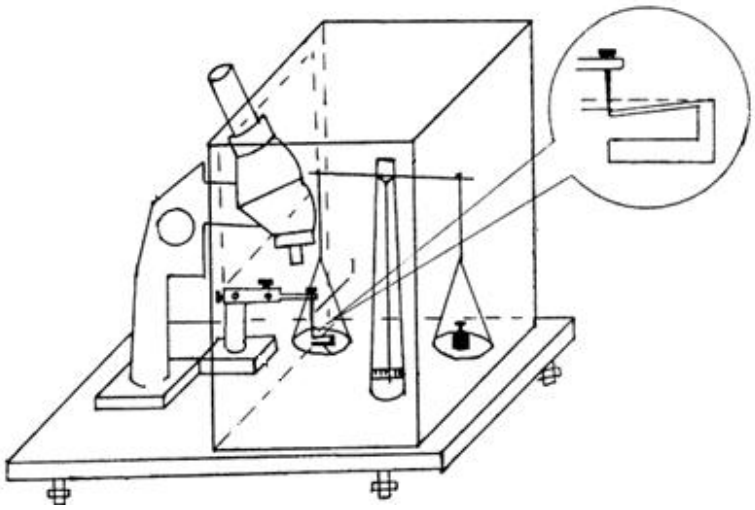

Figure 1.8: Experimental setup used to measure the elastic modulus of thin Ni/Fe microcantilevers [37]

Electroplating was carried out using a pure Fe plate as an anode in a modified Watt's type bath. The electroplating bath was operated in a temperature and current density range of 40 – 60 ^{o} C and 5 – 40 mA/cm^2 respectively while the pH of the electrolyte was kept in the range of 3 – 4. X-ray fluorescence analysis was employed to characterize the composition of electroplated Ni/Fe microcantilevers. The electroplated microcantilever beams had a constant thickness of 15 µm as the length and width were 500 and 50 µm respectively.

The measured modulus of elasticity was varied from 101 GPa to 186 GPa while nickel ratio of films was increased from 43 wt. % to 57 wt. %. This huge variation was attributed to geometrical uncertainties and the electroplating parameters.

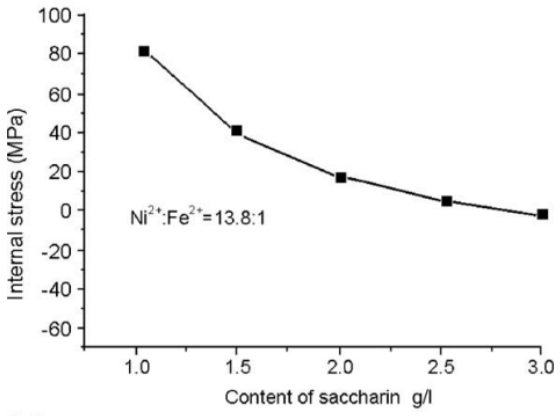

Figure 1.9: The internal stress in thin films as a function of saccharin additive content [7]

Zhang, Y. *et al.* [7] characterized the internal stress in electroplated Ni – Fe alloy with the wafer bending and spectrophotometry. The internal stress of fabricated films was decreased by reducing Fe concentration in the films and addition of saccharin additive.

Tensile stress presented in the deposited films, measured by wafer curvature method, decreased as saccharin concentration was increased as seen in the Figure 1.9 while the current density of 5 mA /cm^2 was used for the electroplating process. The decrease of tensile stresses presented in the films was again explained with the formation of compressive stresses by saccharin additive on film vacancies. It is also emphasized that saccharin had no significant effect on the composition of electroplated films.

In the study, the interrelationship among the current density, Fe content in fabricated films and internal stress was characterized for low and medium concentration of Fe in the employed electrolytes.

As a MEMS application, low stress of Ni – Fe films was validated by electroplating deformation-free cantilevers in an RF MEMS switch. Electroplating process was carried out at current density of 5 mA/cm^2 with 3.0 g/L saccharin additive added low Fe concentration (Ni/Fe=13.8:1) electrolyte.

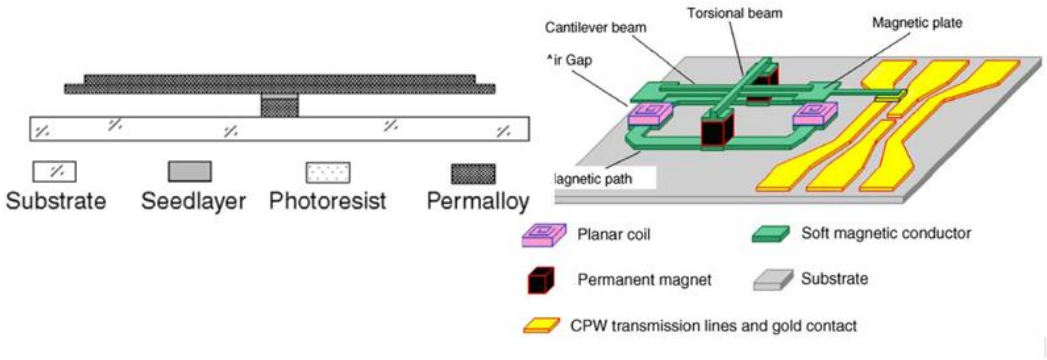

Figure 1.10: The schematic view of the cross section (on the left) and the fabricated RF MEMS switch (on the right) respectively [7]

Almost deformation-free permalloy cantilevers with a T-shaped cross section having a length and width of 700 and 40 μm respectively, as can be seen in Figure 1.10, were fabricated.

Wu, Y. B. *et al.* [8] fabricated leveraged permalloy (81 wt.% Ni – 19 wt.% Fe alloy) cantilever beams suspended in air by torsion flexures fixed at their mid-span (Figure 1.11) and featuring low stresses on the order of ±6.27 MPa with a low stiffness of 1.63 N/m. A laminated photoresist sacrificial layer process utilizing a multilayered photoresist film was employed to fabricate and release fabricated cantilevers. Furthermore, varying concentration of saccharin was added to the electroplating solution to reduce the residual stress in fabricated NiFe permalloy beams and an improved wet releasing scheme was recommended to avoid

stiction of suspended microstructures. A bistable switching mechanism was demonstrated as a possible application of developed leveraged cantilever beam.

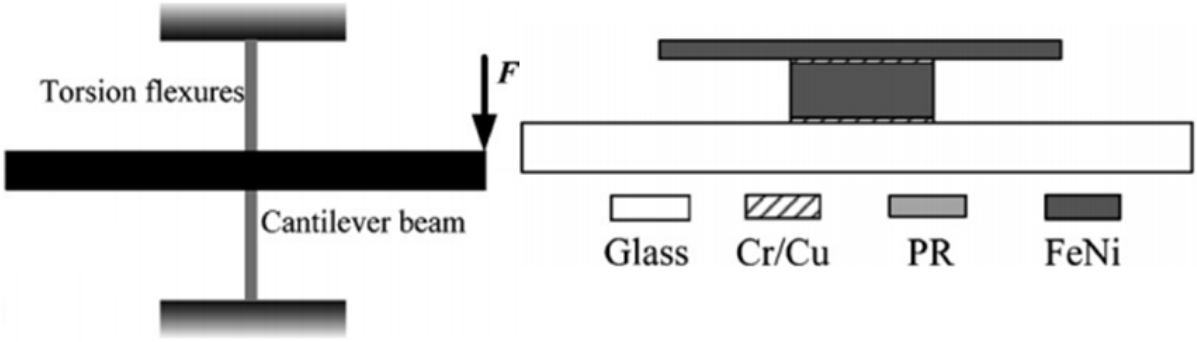

Figure 1.11: Proposed free-free cantilever (on the left) and its final structure at the end of the fabrication flow (on the right) [8]

The wafer bending method was employed to determine the residual stress as a function of additive saccharin concentration in the electroplated permalloy films. Saccharin concentration was varied from 1.0 g/L to 3.0 g/L. Electrodeposition was carried out in a modified nickel chloride bath at 30 ^{o} C while the current density and pH of the electrolyte were 5 mA / cm^2 and 2.8 ± 0.2 respectively.

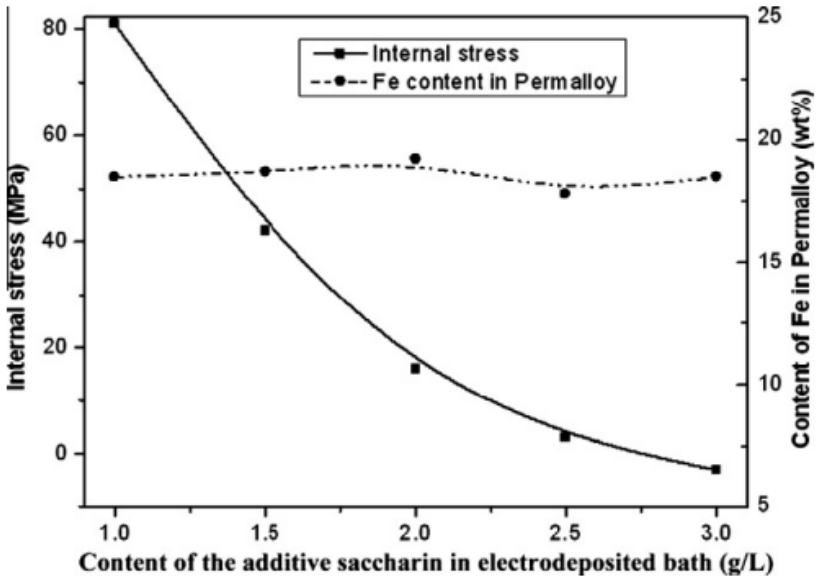

Figure 1.12: Internal stress and Fe content in fabricated films as a function of saccharin additive concentrations [8]

As it can be seen in the Figure 1.12, the decrease in stress was more emphasized at lower saccharin concentrations. However, at higher saccharin concentrations, the decrease in stress of fabricated thin films became weakened. Mechanism of stress reduction by saccharin addition was explained by dislocation theory related to vacancy. Compressive stresses

developed from a big molecule additive like saccharin on a film vacancy resulted in a decrease in initial tensile stresses of Ni-Fe films. Saccharin addition reduced tensile stress in the deposited permalloy cantilevers from 79.8 MPa to -6.27 MPa.

Validation of stress measurements with the wafer bending method was performed by comparing the deformations of the tip of the cantilevers of 1100 µm in length fabricated from either additive-free or saccharin added electrolytes. The deformations of the end of the cantilevers dropped from over ten microns to almost zero (0.2 µm) deformation by saccharin additive addition.

Figure 1.12 also indicates that addition of additive saccharin resulted in no considerable change on cantilever beam compositions. In addition, a vibrating sample magnetometer was employed to determine the magnetic properties of deposited Ni-Fe films. The measurements revealed that saccharin addition had no significant effect on the magnetic properties of deposited Ni-Fe films which also support preserving similar film compositions before or after addition of saccharin additive.

At the final step of the wet release process, cyclohexane was recommended to use over acetone, ethyl alcohol or DI water due to its better total average of vapor pressure, boil point, surface tension and flash point properties. Proposed released process comprised subsequent dipping of chips in DI water, acetone, ethyl alcohol and finally 1.1-Dimethyl cyclohexane solution respectively. A chip in a cyclohexane solution was heated on a hot plate at 60 ^{o} C until the cyclohexane solution was vaporized.

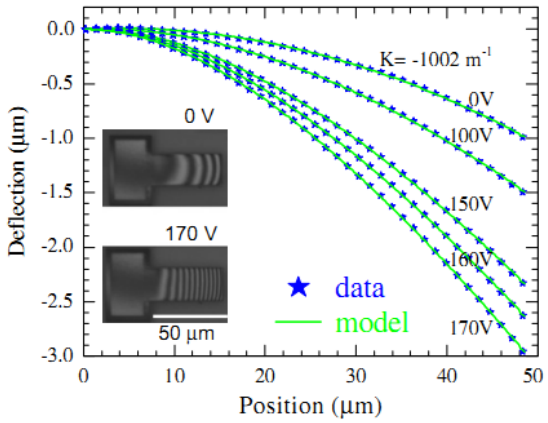

Figure 1.13: Deflection data of electrostatically actuated microcantilever together with model fits [38]

Boer, M. P. *et al.* [38] investigated the modulus of elasticity of thin films using electrostatically actuated free standing Al-0.5 wt. % Cu cantilevers. Double clamped beams

were also utilized for residual stress measurements. Strength and fatigue properties of thin films were also studied.

Metal cantilevers having lengths of 50, 150, 300, 420 μm and width of 25 μm and fixed-fixed beams having lengths of 150, 300, 500 μm and width of 25 μm were fabricated for elastic modulus and residual stress measurements using SUMMIT V^{TM} process design tools. DC magnetron sputter deposition at 175 ^{o} C was carried out to form 0.43 to 0.65 μm thick Al-0.5 wt. % Cu films. Wafer curvature experiments revealed residual stress of 300 MPa for the biaxial stress of Al-0.5 wt. % Cu layer. At the end of the fabrication process, residual stress ranging from 30 – 60 MPa was found, which was significantly lesser than the as-deposited value due to fabrication induced plastic straining. Metal structures were released with a critical point drying process. Deflection curves of samples due to electrostatic actuation were obtained using an interferometer as seen in Figure 1.13.

Cantilevers having lengths of 50 μm were used for elastic modulus measurements because cantilevers whose length was greater than 50 μm contacted the substrate.

The modulus of elasticity was determined by fitting measured deflection data of microcantilevers to the simulation deflection data by varying the elastic modulus parameter of the model. The average modulus of elasticity for Al-0.5 wt. % Cu film was evaluated as 74.4 ± 2.8 GPa which was found compatible with grain texture measurements. Here a dominant out-of-plane texture with little or no in-plane texture was obtained through EBSD orientation mapping. Grain size measurements of films ranging 0.4 – 4.5 μm revealed the average grain size of 1.75 μm with a standard deviation of 0.8 μm.

1.3 Multilayer Ni Microcantilevers

Luo, J. K. *et al.* [4] characterized the effect of electroplating process variables including the plating temperature and current density on the modulus of elasticity of nickel thin films. A sulfamate plating solution consisting of nickel sulfamate (300 g/l), nickel chloride (10 g/l) and boric acid (40 g/l) was employed for nickel electrodeposition. A magnetic pellet was utilized for stirring the solution in order to prevent the formation of hydrogen bubbles on the sample surface. The employed plating temperature and current density ranges were adjusted as 20 – 80 ^{o} C and 2 – 30 mA/cm^{2}. Fabricated 1.5 – 3 μm thick nickel layers were plated onto 60 nm thick Cu seed layer. Nickel cantilevers of length 500 μm and width 150 μm was cut by a laser machining system using UV light. Beam bending

experiments were performed by a commercial profiler of Dektak 8 to measure the transverse tip deflection. Since the curvature of beams could not correlate with the process parameters due to significant variation among fabricated cantilevers, the modulus of elasticity could not be associated with the curvature or the gradient stress.

The modulus of elasticity characterization of nickel thin films were carried out by varying current density at a constant plating temperature of 60 ^{o}C and by varying the plating solution temperatures at a constant current density of 2 mA / cm^2 as shown respectively in the Figure 1.14. Modulus of elasticity decreased from approximately 205 GPa at a temperature of less than 60 ^{o}C, which is close to the corresponding bulk value of 210 GPa, to 100 GPa at 80 ^{o} C. Inclusion of ammonium and sulfate ions by hydrolysis at above 70 ^{o}C was believed to be responsible of this drastically sharp drop. The sharp decrease of modulus of elasticity at 80 ^{o} C was found repeatable. Results indicated that the modulus of elasticity decreased linearly from a near bulk value of 205 to 85 GPa as the plating current density increases.

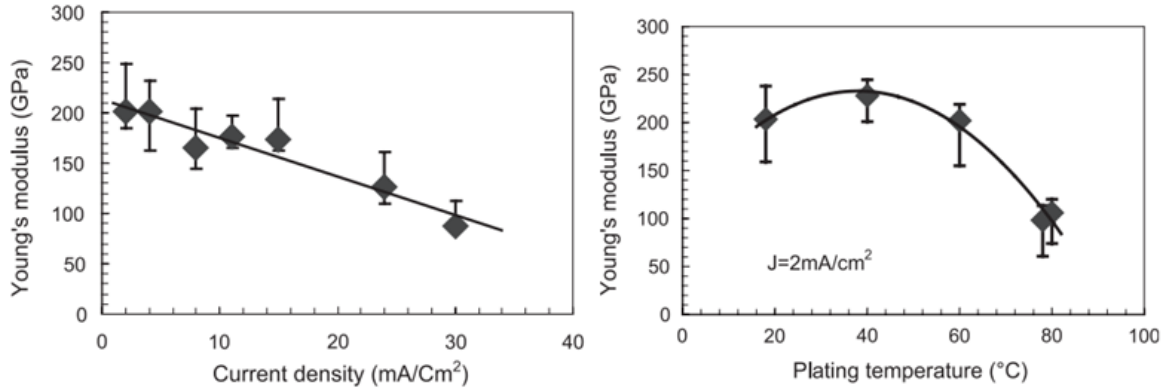

Figure 1.14: The modulus of elasticity of thin nickel beams as a function of current density and temperature [4]

Ni film roughness measurements by AFM revealed an increase from 11 nm to 25 nm as current density was increased from 2 mA/cm^2 to 20 mA/cm^2. The lowest modulus of elasticity was obtained at highest current density (30 mA / cm^2) and temperature (80 ^{o} C) values. This modulus of elasticity variation was attributed to the microstructural change from columnar structure of Ni which corresponds to a high modulus of elasticity to the fine-grained structure by increasing the current density. Usually electroplating at high temperatures and low deposition rates promotes a columnar structure in electroplating metal films.

Itoh, T. *et al.* [39] fabricated electrostatically actuated Ni microcantilever probes which were suitable for new MEMS probe cards with contact-switching function. Ni microcantilever arrays were fabricated by electroplating of two Ni layers having different

internal stress. In the work, the characteristics of contact between the electroplated probes and Al electrodes were also studied.

Low stress nickel electrodeposition followed by high stress nickel electrodeposition resulted in curl-up microcantilevers as in Figure 1.15. Sulfamic acid and nickel sulfate bathes were employed to deposit two nickel layers with different internal stress. Wet etching of sacrificial Al layer using a 20 % KOH solution at room temperature were utilized to release fabricated cantilever probes. Cantilevers with a thickness of 1.0 μm and width of 50 μm were fabricated. Lengths of cantilevers were 100, 150, 200, 250, 300 and 400 μm.

In the study, two types of cantilevers having different thickness ratio of high stress layer to low stress layer were fabricated. Therefore the effect of the thickness ratio of the high stress layer to low stress layer on cantilever tip heights were observed. Some cantilevers also had an etching slit pattern in order to investigate the effect of etching slit pattern on pull-in voltage and the pull-in voltage measurements revealed that introduction of etching slit decreased the pull-in voltage.

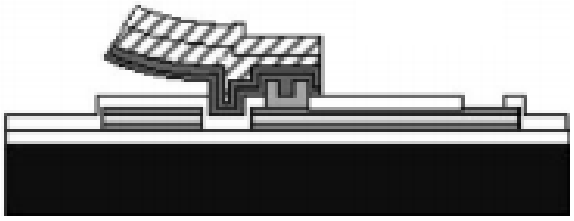

Figure 1.15: Schematic representation of fabricated curled-up cantilever probe [39]

Displacement of released cantilevers for a certain load was measured by a surface profiler. From the slopes of load-displacement curves, the effective modulus of elasticity was estimated as 140 and 200 GPa for cantilevers with different ratios of high stress layer to thickness of low stress layer thicknesses. This large scatter of modulus of elasticity values was attributed to differences in thicknesses of realized cantilever from measurement values rather than the small thickness ratio difference.

Fabricated microcantilever probes were electrostatically driven with a pull-in voltage of less than 150 V. The pull-in voltage measurements of fabricated cantilevers with various lengths showed that there was an only slight gradual decrease in pull-in voltages with increasing cantilever length. This implied that tip heights of the cantilever probes can be

easily adjusted by changing only the lever length without a significant change in pull-in voltage.

Ostasevicius, V. *et al.* [40] investigated dynamic properties of a vibrating micromechanical switch by modifying the classical time average holographic technique. Time average holography was demonstrated to determine the shape, direction and magnitude of the stress-induced displacement for a MEMS switch shown schematically in Figure 1.16. Modified time average holography as a powerful tool for analysis of microscale vibrations were employed to characterize kinetics of oscillations of a microrelay.

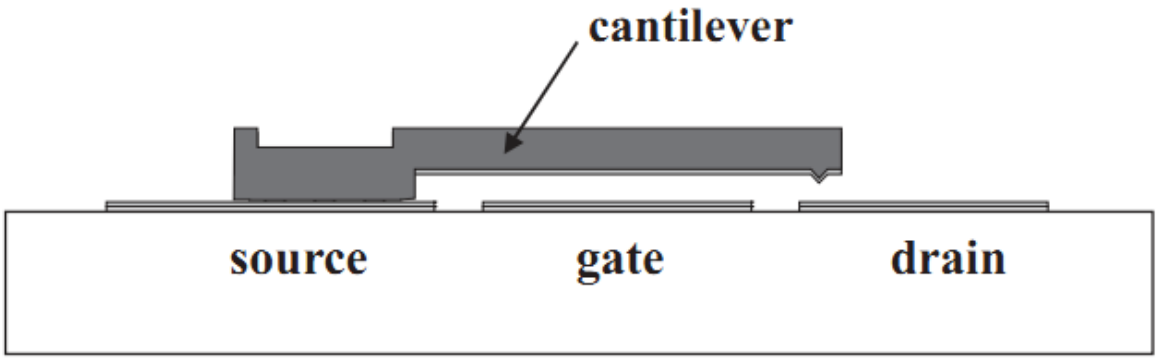

Figure 1.16: Fabricated switch configuration with 3 µm thick electroplated Ni microcantilever [40]

Cantilevers with a thickness of 3 µm were fabricated by nickel electrodeposition in a nickel sulfamate bath. The length and width of free standing cantilevers were 200 µm and 30 µm, respectively.

Kim, S. H. *et al.* [5] developed a microcantilever model accounting for mechanical behavior of cantilevers due to mismatch strain during fabrication. Verification of the model was demonstrated with Ni electrodeposition onto an atomic force microscope cantilever beam.

Modulus of elasticity of nickel films was determined by comparison of Sader's method and elementary beam theory. In situ measurement of the deflection of stepwise altered cantilever thicknesses through the optical method of AFM shown in Figure 1.17, resulted in the mismatch strain with the through thickness variation.

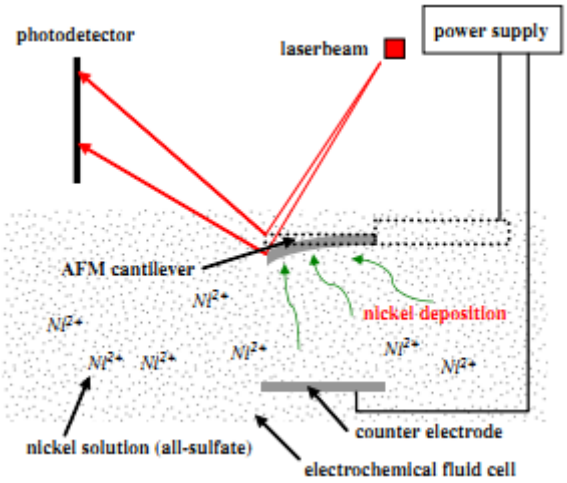

Figure 1.17: Experimental setup for Ni electrodeposition onto an AFM cantilever and in situ simultaneous profile measurements [5]

Electroplating experiments were performed with an insoluble platinum electrode and an all-sulfate nickel electrochemical fluid cell consisting of the nickel sulfate (225-400 g/l) and boric acid (30-45 g/l).

Electrical conductivity on pure cantilever surfaces for subsequent electroplating of nickel was achieved with a thin evaporated Cr/Au layer. Nominal dimensions of the cantilever used in experiments were 230 ± 5 µm in length, 40 ± 3 µm in width and 7.0 ± 0.5 µm in thickness. Standard metallic spring clips holding AFM chip in the fluid cell were employed to provide a electrical contact with gold-coated sides of cantilevers.

The total average modulus of elasticity of 155.36 GPa with a maximum standard deviation of 3.47 GPa was evaluated. The strain as a function of the out-of-plane coordinate determined for fabricated five beams revealed a decrease in the out-of-plane direction.

Ozturk, A. *et al* [41] used nickel cantilevers with integrated diffraction gratings as resonant mass sensors with a resolution of 500 femtograms to detect human opioid receptors. Simple one mask fabrication process together with microoptical readout and external electromagnetic actuation were the promising aspects of the mass sensor.

Since the grating interferometry principle was employed, the relative average roughness has of great importance. For current density of 5 to 10 mA/cm^2, obtained average roughness achieved less than 20 nm found sufficient for optical measurements by adjusting temperature, current density and electroplating duration. During the electroplating process, the temperature of a continuously stirred nickel sulfamate bath was adjusted to 40 ^{o}C and current

densities varying from 5 to 25 mA / cm^2 were employed. At the end of the fabrication flow, cantilevers being composed of electroplated nickel and Au as both the seed and functionalization layer were manufactured.

The operation and the mass responsivity of the fabricated cantilevers were examined with two different approaches. As a first approach, a known amount of gold was sputtered on the sensor and the resulting resonance frequency shift was noted. Manufactured cantilever before sputtering had thickness of 1.4 μm. In the second method, the resonance frequency shift resulted from attachment of hKor protein molecules on a length of 70 μm, width of 7 μm and 1.3 μm thick cantilever was measured. Using the same type of cantilevers fabricated with the identical fabrication flow, the similar optical detection and electromagnetic actuation with an amplifying feedback loop to enhance the mechanical quality factor in liquid, Timurdogan, E. *et al* [42] performed the label-free detection of the interaction between His-tagged human κ-opioid receptor membrane protein and anti-His antibody. A minimum detectable antibody concentration of 5.7 ng/ml for a 50 kHz device was achieved together with a sensitivity of 7 ppm/(ng/ml) and a frequency resolution of 2 Hz.

He, S. *et al.* [43] characterized the modulus of elasticity and residual stress gradient of MetalMUMPs 20 μm thick electroplated nickel film. The modulus of elasticity and residual stress gradient of the nickel film were determined in the range of 155 – 164 GPa with an average of 159 GPa and -5.49 MPa/μm to -4.30 MPa /μm with the average of -4.72 MPa /μm respectively.

Electroplating process parameters of temperature of 30 ^{o} C and current density of 20 mA/cm^2 and pH level of 4 were selected as in MetalMUMPS. The length of the fabricated beams varied from 1000 μm to 700 μm with a step of 50 μm. 100 um width was selected for all beams. Three layered beam structures consisting of plating copper base (0.55 μm), electroplated nickel (20 μm), and top gold layer (0.5 μm) were fabricated.

Actuation of cantilever beams to their first mode resonance frequencies was performed by piezoelectric transducers. Surface profiles were obtained by using a 3D optical profiler.

In order to account for the effects of non-ideal supports due to fabrication which is excluded in the analytical equation, numerical simulations were employed to extract the modulus of elasticity of films.

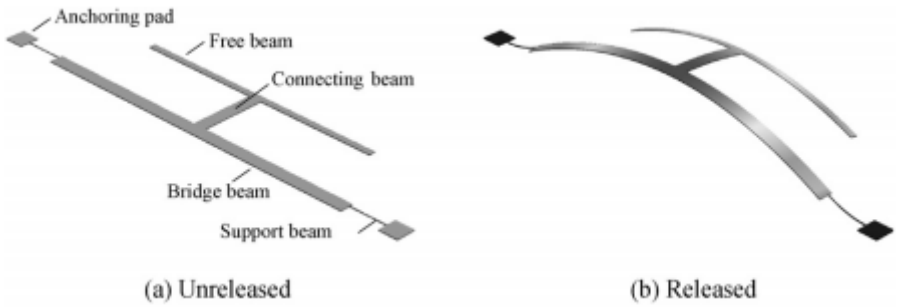

Figure 1.18: Proposed free-free beam mechanism for a more accurate stress gradient determination [43]

In this work, instead of employing single clamped cantilever structures, a stress gradient induced free-free beam mechanism schematically demonstrated in Figure 1.18 was proposed for more accurate characterization of negative residual stress gradient in thin films. A free-free beam raised by a bridge beam accommodates more bending downward displacement and a longer beam preference possibility for stress gradient characterization experiments.

The residual stress gradient was found inversely proportional to the nickel film thickness. This relation was believed to be a possible result of asymmetric structure of the beam.

1.4 Other Multilayer Metallic Microcantilevers

Baek, C. W. *et al.* [44] using UV-LIGA surface micromachined cantilever and bridge beam structures investigated the modulus of elasticity, average residual stress and stress gradient of electroplated gold thin films. From the resonance frequencies of electrostatically excited cantilever beams, the stress gradient and modulus of elasticity and from the resonance frequencies bridge beam structures, average residual stress were determined. In the experiments, for a bridge structure, the effective residual stress in the film was assumed to be uniform.

The beams of 100-1000 µm in length, in 100 µm increments, 100 µm wide and 3-4 µm thick were fabricated. Utilizing a commercial non-cyanide neutral plating solution, the gold electroplating was carried out at 65 ^{O}C at current densities of J=2 or 4 mA/cm^2 with solution agitation. Microstructures were released from Si substrates by the dry release method of oxygen plasma ashing.

Actuation of beams was accomplished by applying a DC bias voltage and small AC excitation voltage of varying frequency between the beam and the driving electrode underneath. The measurements of the resonance frequencies were performed with an optical measurement system consisting of a power amplifier, laser displacement meter and signal analyzer as it can be seen in Figure 1.19.

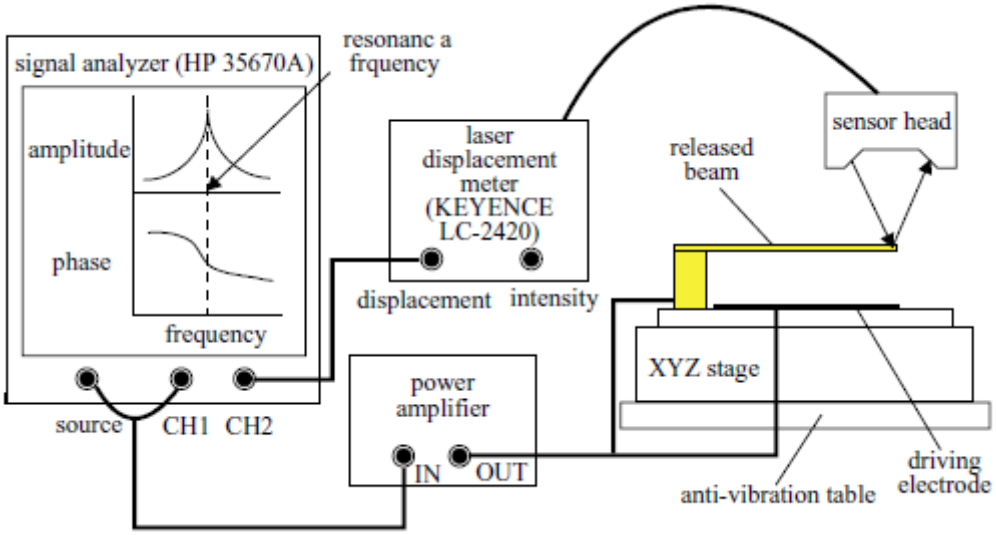

Figure 1.19: The Schematic representation of the experimental setup for the measurement of resonance frequency of Au microstructures [44]

The modulus of elasticity of fabricated Au microstructures was observed to range from 35.2 GPa to 43.9 GPa which was smaller than corresponding bulk value. As current density was increased from 2 to 4 mA / cm^2, the modulus of elasticity was slightly increased. From the cross sectional view of the electroplated gold structure, it was deduced that electroplated gold film had a columnar nature and a little finer grain size at the bottom side than the top side. Difference of measured modulus of elasticity value from the bulk value was attributed to structural anisotropy, texture effect and plasma ashing process.

Typical averaged residual stress values ranging from 40.1 MPa to 43.8 MPa were found to be tensile. Stress gradient of cantilever ranged from 4.2 MPa/µm to 12.7 MPa/µm. It was concluded that a higher deposition current density induced a much larger stress gradient in the electroplated gold film, even though the average stress in the beam found independent from the current density.

The measurements revealed that beam profiles changed with the ashing time. The anisotropy of the structure and thermal effects incurred during the plasma etching process was attributed to this behavior.

Mulloni, V. *et al.* [45] characterized the effect of dry release parameters on the shape of suspended single clamped (Figure 1.20) and double clamped gold microstructures. Electrodeposited gold microstructures were released from a sacrificial photoresist layer by oxygen plasma ashing. Most of the deviations from the ideal planar shape were believed to originate from yield and inelastic relaxation. The fabrication parameters including the initial stress value, the release temperature and the vertical structural homogeneity of the gold layer were optimized to get rid of these unwanted effects.

The temperature effects on the final deformation of gold devices can be explained by thermal stress variations and inelastic relaxation. Especially in case of gold structures, since the thermal expansion coefficient difference between gold and usual substrates like silicon or quartz, temperature effects are emphasized.

In the experiment, two series of cantilevers were used. First series consisted of cantilevers whose length varied from 50 to 280 µm and the width was 15 µm while in the second series the length went from 150 to 500 µm and the width was 120 µm. Release process was tracked by means of an optical profiler.

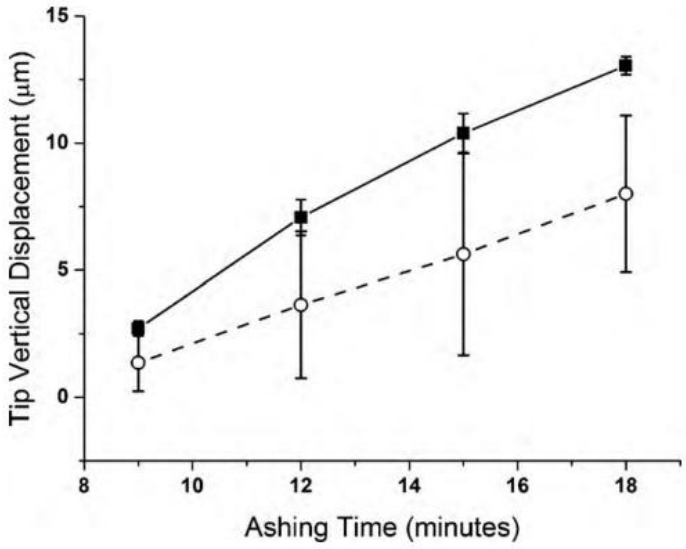

Figure 1.20: Tip deflections of gold cantilevers with (filled squares) and without (open circles) fast thermal cycling before release [45]

Cantilever beams were electroplated to a thickness of 1.8 um. For clamped-clamped structures, a control of switch actuation voltage for a real RF-switch was demonstrated by controlling of the release process.

Hong, S. H. *et al*. [46] employed nanoindentation technique and microcantilever beam bending test to determine elastic moduli of Cu thin films in perpendicular or parallel directions to film surface. Electroplating was utilized to fabricate Cu thin films having a thickness of 3 – 12 µm by varying electroplating parameters. Nanoindentation measurements through thickness in Cu thin films resulted in 123 – 99 GPa for elastic modulus of fabricated Cu films and elastic modulus was found inversely proportional with increasing film thickness. On the other hand, elastic modulus measurements by beam bending test in parallel direction of Cu thin films resulted in 121 GPa for 2.8 µm thick Cu thin film and 90 GPa for 10.5 µm thick Cu thin film.

Theoretical elastic moduli estimations in perpendicular or parallel direction to the film surface were done according to Voigt's and Hill's model based on the texture analysis by XRD technique. Theoretical estimations of elastic moduli agreed well with experimental measurements based on nanoindentation method.

Electroplating process was performed at a constant current density of 10 mA/cm^2 in a copper acid sulfate solution on a seed layer of 100 nm thick DC-magnetron-sputtered Cr layer. Variation of the electroplating deposition time led to 2.8 or 10.5 µm thick Cu cantilever beams whose lengths varied from 50 to 250 µm and had a fixed width of 50 µm.

Chow, E. M. *et al.* [47] integrated a high voltage thin film transistor (HVTFT) with a released MEMS process onto a same substrate as shown schematically in Figure 1.21. HVTFTs enables controlling high voltages (50-800 V) using a standard input voltage range (0-20 V). Released Cu cantilevers and membranes with a low temperature fabrication process of less than 350 ^{o}C on glass substrates were actuated with high voltage transistors capable of 800 V actuation voltages.

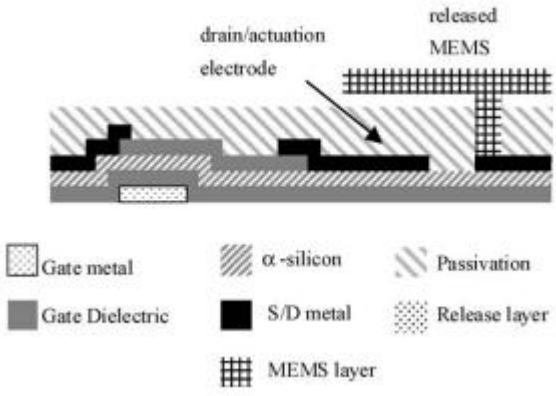

Figure 1.21: The schematic representation of the final structure of HVTFT [47]

The fabrication of HVTFT followed by the MEMS process was carried out on glass wafers. The fabrication of HVTFT utilized sputtering and plasma enhanced chemical vapor deposition (PECVD) deposition techniques. The cantilevers were fabricated by electroplating of copper with a thickness of 1.7 µm. Low peak temperature of the whole fabrication process enables using flexible substrates like glass or polyimide. The deflection of the fabricated released cantilevers as a function of applied voltage was determined with a laser interferometer. This integration led to realizing MEMS arrays with addressable drivers for high voltage required applications.

Slavcheva, E. *et al.* [2] investigated properties of electroplated Ni-W microstructures as a structural material for possible MEMS applications such as temporary contacts for IC integration. Tungsten concentration in the electrolyte, current density - tungsten content in deposited films relationship, the surface structure and morphology of deposits together with

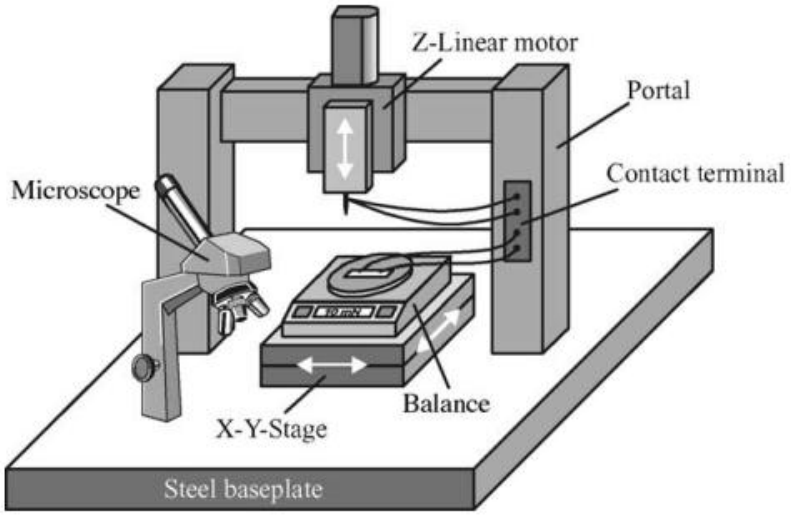

Figure 1.22: The modulus of elasticity extracted from slope of force-deflection curves determined using developed bending test device [2]

mechanical properties of thin layers were examined systematically.

A nickel sulfamate based electrolyte with addition of citric acid used to stabilize tungsten complex were employed to deposit Ni-W thin films using direct and symmetrical pulse (T_{on}=T_{off}=5 ms) current plating schemes. An inductive coupled plasma spectrometer was utilized to track the concentration of metal ions in an electroplating electrolyte. Electroplating baths were operated at a temperature of 50 ^{o} C and within pH range of 2.4 – 3.2. The mean current densities varied from 5 – 20 mA/cm^2 were used to 12 µm thick Ni-W layer with an insoluble anode. The lengths of cantilevers varied from 600 – 800 µm were

fabricated with a constant width of 100 µm. Surface morphology and nickel - tungsten contents in electroplated microstructures together with surface topography were characterized by a scanning electron microscopy (SEM) and energy dispersive X-ray spectroscopy (EDX) respectively. Crystal structures were also determined by X-ray diffraction (XRD) technique.

Modulus of elasticity of fabricated Ni-W cantilevers was extracted from force – deflection curves of beams using a home-made bending device shown in Figure 1.22. The modulus of elasticity of approximately 180 GPa was measured for all fabricated beams. Mechanical properties of fabricated Ni-W films such as micro hardness, elasticity and internal stress compared to pure nickel were improved and optimized at tungsten of 3.2 wt.%.

Kim, B. H. *et al.* [6] studied the effects of processes of ICP-DRIE and nickel-cobalt electroplating for a trench type cantilever probe for a MEMS probe card. Double step DRIE process was utilized to form the cantilever beam and cantilever probe tip inside silicon substrate and then cantilevers were fabricated by electroplating in a nickel-cobalt solution. In order to electroplate the tip of a probe in a deep trench, the existence and thickness variation of the seed layer were investigated using electron probe microanalyzers (EPMA) and SEM. Contact force of cantilever probes as a function of cobalt concentration was explored.

Since the yield strength of nickel of approximately 620 MPa is relatively small for MEMS probe applications, nickel alloys are employed to raise the yield strength and to improve its wear resistance. So the nickel-cobalt electrodeposition was carried out in a nickel sulfamate based electrolyte with some additives at 55 ^{o} C. Current density and pH of the electroplating solution ranged from 1 – 20 mA/cm^2 and 4 – 5 respectively.

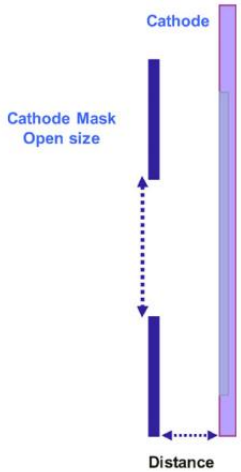

Figure 1.23: The cathode mask was employed to regulate uniformity of electroplated layer and wafer bending [6]

Electrodeposition was adopted to avoid voids and seams in the cantilever probes. In order to improve uniformity of electroplating on a 6” wafer and reduce wafer bending by the tensile stress of nickel-cobalt electrodeposition, a cathode mask shown in Figure 1.23 was employed and optimized. Voids and seams in the electroplated cantilever probes were investigated by X-rays to determine the quality of nickel-cobalt electroplating and voids and seams were found proportional to the tip aspect ratio, current density and contamination of nickel-cobalt solution.

1.5 Remarks

In the literature, metallic micro and nano cantilevers are employed to determine various mechanical properties including modulus of elasticity, yield stress and residual stress. Cantilevers of less than a few microns are mostly deposited by physical or chemical deposition methods such as DC or RF sputtering, e-beam or thermal evaporation. In the case of nickel, even less than 1-μm-thick layers are mostly electroplated due to advances in nickel electroplating and extensive employment of nickel in MEMS applications. Material mechanical characterization is performed mostly with beam bending techniques and resonance method if microcantilevers are adopted as a characterization tool. Research in thin metallic films is mostly focused on the determination modulus of elasticity and residual stresses. Elastic modulus of metallic films were determined as a function deposition parameters such as current density, temperature in case of electroplating, composition in case of alloys or film thickness in many studies presented briefly in literature review above.

Uniform residual stresses in thin films are studied extensively with many techniques using double clamped microstructures or by following wafer curvature shifts after deposition of thin films on substrates. However, unlike uniform residual stress, exploration of residual stress gradient in thin metallic films remains mostly untouched. Some studies [44, 48] determined residual stress gradient at some specific deposition condition or very limited fabrication parameter range. Those studies suffer from ignoring additional seed layers in stress gradient calculations of films thicker than 1 μm. Another problem encountered in stress gradient characterization is the effect of wet or dry release methods on cantilever deflections. Dry cantilever release by sacrificial layer removal with plasma based techniques resulted in thermal loadings and inevitably microstructural changes [45]. These problems result in gradient data distribution in a very large range.

Some studies prefer to evaluate residual strain gradients [36] for different fabrication parameters or mismatch strain [5] for different film thicknesses required to convert residual stress gradients.

Microstructural analysis, using X-ray diffraction (XRD) or scanning electron microscopy (SEM) methods, of films relatively thicker than 1 μm were performed as a function deposition conditions. Similar microstructural analysis of films with a thickness on the order of 1 μm is also required.

Therefore systematic stress gradient characterization of 1-μm-thick electroplated nickel films as a function of fabrication parameters supplemented with a microstructural analysis would be a pioneering study in this field to understand out-of-plane deformations of electroplated nickel with electroplating deposition conditions.

1.6 Motivation

Nickel has wide range of applications in MEMS field due to its attractive mechanical and magnetic properties. Considerable modifications of mechanical properties such as the modulus of elasticity and residual stress with deposition parameters make nickel electroplating attractive among various deposition methods.

Residual stress is one of the most investigated thin film mechanical properties that affects and degrades electronic and magnetic properties, performance, structural integrity and long-term stability of the thin films. Residual stress gradients that determine out-of-plane deflections in thin films needs to be characterized to better estimate performance and life-time of articles designed as a moving part in a MEMS application at initial design stages.

In the Biosensor project, label free detection of biomolecules is performed using magnetically actuated micro-resonator cantilevers. Frequency response of microcantilevers is monitored with an optical readout mechanism, based on embedded diffraction gratings as shown in Fig. 1.24. Light beams reflected either from base silicon surface or movable nickel cantilevers form the grating interferometry. Then deflections of microcantilevers are obtained from modulation of the intensity of diffraction orders. Large scatter of light beams reflected from severely bent microstructures results in low signal amplitudes, measured with the employed photodiode. In this study, tip deflections of less than 1 μm are aimed for microcantilevers having length of 100 μm.

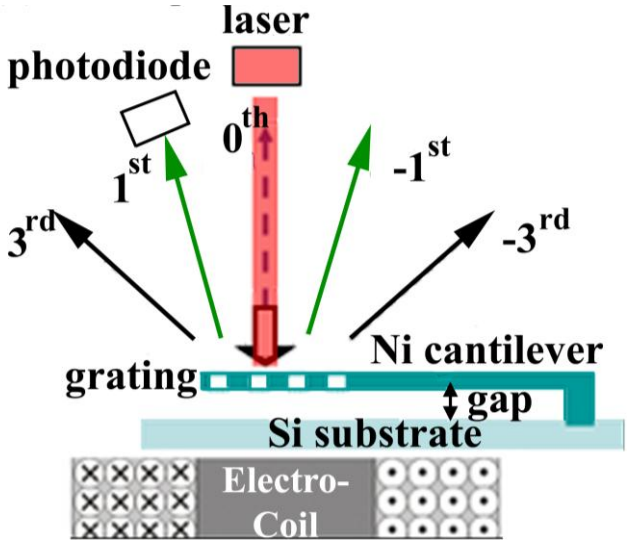

Figure 1.24: Optical readout using the grating interferometry principle employed in the Biosensor project [41]

The primary motivation of this study is to characterize the residual stress gradients in electroplated nickel films as a function of process parameters namely solution temperature and cathode current density with single-layer microcantilevers. The final goal of this work is to optimize plating parameters to obtain zero residual stress gradients so that straight beams can be produced.

Microstructural analysis of fabricated nickel films is also performed to understand nickel film characteristics and correlate them with the mechanical properties.

The organization of this thesis can be summarized in the following manner. In the second chapter, origins, measurement techniques and reduction methods of residual stresses in electroplated nickel thin films are given right after a brief introduction of the basics of nickel electroplating. Moreover, the derivation of the residual stress gradient for single layer microcantilevers is supplied. Chapter 3 starts with the discussions of the employed fabrication flow and lithography mask. Then the characterization of residual stress gradients in 1-µm-thick nickel films is performed as a function of electroplating process parameters, *i.e.* current density and electroplating temperature. In order to evaluate residual stress gradients in nickel films, microcantilever tip deflection and modulus of elasticity measurements are carried out. Nickel film thickness effect on cantilever deflections together with cantilever deflection evolution with time, is studied. Microstructural analysis, supported with XRD measurements and SEM pictures of samples having various nickel film thicknesses, are also explicated. Finally, conclusions and future works are given in last chapter.

Chapter 2: Residual Stress Development in Nickel Electroplating

2.1 Introduction to Nickel Electroplating

Electroplating is a well-studied and commercialized technique used in the fabrication process of macro- and as well as micro-devices. Higher deposition rates, no vacuum requirements, low deposition temperatures, ability to manipulate mechanical properties such as the modulus of elasticity and residual stress simply with deposition parameters, high yield and relatively cost-effective equipment are the leading advantageous of the electroplating process that make this technique widespread. However, there are also some challenges of electroplating including the requirement of strict control on the cleanliness of the electroplating solution and on the conditions of operation to produce consistent deposits with similar properties, layer uniformity and layer defects such as roughness and pitting.

The applications of nickel electroplating can be divided into three main categories; namely decorative, functional, and electroforming.

In decorative applications, bright multilayered nickel coatings applied in combination with the electrodeposited microdiscontinuous chromium have the significant corrosion resistance for extended periods of time.

Functional applications imply depositions of nickel and nickel alloys with matte or dull finishes in order to improve deposit properties such as corrosion and wear resistance, magnetic properties.

In electroforming, the electroplating can be performed either with mandrels to remove fabricated nickel structures from a custom mandrel or using masks to deposit permanent electrodeposits.

In this section of the thesis, the nickel electroplating as a subdivision of the nickel electroforming implying permanent electrodeposited microstructures by employing masks will be reviewed. Basics of electroplating process are briefly discussed by largely utilizing the following work of "Modern Electroplating" throughout this chapter [49].

2.1.1 The Development of Nickel Electroplating Solutions

Nickel electroplating by employing the first practical formulation of aqueous solution of nickel and ammonium sulfates was performed by Bottger in 1843. However, a platinum

electrode was coated with nickel using a nickel chloride or sulfate electrolyte in 1837 by Bird and Shore having the first nickel electrolyte patent for a nickel nitrate solution in 1840. Due to widespread application of Bottger's electrolyte, he is known as the originator of nickel plating. The commercialization of the nickel electroplating in USA was started with the use of pure nickel ammonium sulfate by Dr. Isaac Adams Jr. The main improvement of Adam's solution was to control the nickel deposit quality by ensuring neutral pH operation of the electrolyte. Remington introduced using small pieces of electrolytic nickel as an anode material in a platinum anode basket. Usage of boric acid component in nickel electroplating baths and the employment of nickel chloride which ensures efficient dissolution of nickel anode materials were initiated by Weston and Bancroft, respectively. In 1918, an advanced nickel electroplating electrolyte composed of nickel sulfate, nickel chloride, and boric acid components was developed and optimized by Prof. Oliver P. Watts from the University of Wisconsin. This electrolyte with its variations outperformed other rival electrolytes and it is still widely applied for the nickel electrodeposition applications. Bright nickel plating solutions which are variations of the original Watts bath by including organic and metallic compound additives such as benzene and naphthalene di- and trisulfonic acids to brighten and level the nickel deposits were introduced in 1934 by Schlotter. The major contribution of DuRose was the development of double and triple layer nickel coatings with greatly improved corrosion resistance using coumarin containing semi-bright nickel plating solutions in 1945 [49].

The dominant position of Watts' solutions is overrun on a substantial scale only by nickel sulfamate solutions for electroforming applications. Watts type baths are preferred to be used for decorative and functional applications with significant variations in the chloride contents [49].

2.1.2 Fundamentals of Nickel Electroplating

Electroforming term generally refers to the non-adherent electrodeposition of a metal on a substrate such as a mandrel or mold in order to separate it from the substrate after the electroplating process to become the final product. Mandrels having negative (reverse) shape of the fabricated product can be re-used. However unlike electroforming, electrodeposition is carried out through masks on a substrate such that the deposit is an integral part of the employed substrate.

Nickel electroplating is performed by applying direct or alternating current between two electrodes immersed in a conductive, aqueous solution of nickel salts. Nickel electroplating is carried out by dissolving of one of electrodes (the anode) to form divalent, positively charged ions (Ni^{++}) and coating of the other electrode (the cathode) with nickel as a result of the applied current. Thus the discharged nickel ions at the cathode replaced with those formed at the anode result in constant Ni concentration in the bath.

The amount of nickel deposited at the cathode or dissolved at the anode can be determined using the following expression;

$$m = 1.095\, a\, I\, t \tag{2.1}$$

where *m* is the amount of nickel deposited at the cathode or dissolved at the anode in grams, I is the mean applied current in amperes, *t* is the time of applied current in hours, and a is the current efficiency ratio. Eq. 2.1 implies that the amount of deposited nickel is directly proportional to the product of current, time and the current efficiency ratio. The proportionality constant of 1.095 corresponds to M/nF where M is the atomic weight of nickel of 58.69, n is the number of electrons in the electrochemical reaction of 2 and F is Faraday's constant of 26.799 ampere-hours or 96,500 coulombs.

While the anode current efficiency is almost 100%, that is a=1, under practical electroplating conditions, the cathode current efficiency may vary from 90% to 97%, *i.e.* a will vary 0.90 to 0.97, for different nickel plating electrolytes. This difference between anode and cathode nickel current efficiencies result in an increase of the nickel ion concentration and the pH of the solution as the solution is employed.

The efficiency of anode dissolution decreases to zero under the conditions of high solution pH and low chloride ion concentration. Under these conditions, the nickel anode becomes passive while oxygen is formed in the solution by preferential formation of hydroxyl ions instead of the dissolution of nickel.

The deviations from 100% cathode current efficiency are caused by the consumed fraction of the applied current to form hydrogen ions from water. These hydrogen ions form bubbles of hydrogen gas at the cathode surface. Consequently, an average cathode efficiency of 95.5% is employed to estimate the amount of nickel coated at the cathode.

The electroplated nickel thickness, s in µm, can be determined using the following expression;

$$s = \frac{m\ 100}{d\ A} = \frac{12.294\ a\ I\ t}{A} \tag{2.2}$$

where d is the product of the density of nickel of 8.907 g/cm^3 and A is the surface area to be electroplated. The ratio, I/A, corresponds to the current density (J). Thus Eq. 2.2 implies that the electroplated nickel thickness is a function of current density rather than current which is the case for the amount of electroplated nickel.

On the surfaces of every electroplated part, there is a certain degree of nickel thickness variation. The current distribution determined by geometric factors such as the shape of the part, the relative placement of the part with respect to the anode, how the parts are placed on plating racks and the dimensions of the system define the actual electroplating thickness for each point on a surface of an electroplated part.

The shorter anode to cathode distance and corresponding lower resistance to current flow, i.e. a higher current density, produce thicker electrodeposits at prominences than recessed areas. This inevitable electroplating thickness variation can be minimized by employing shields made of nonconductive materials or auxiliary anodes placed closer to the cathode than principal anodes. Current is lead to recessed or relatively small areas on a cathode by employing an either soluble or insoluble auxiliary anode.

Table 2.1: Nickel sulfate and nickel sulfamate based nickel electroplating baths produce nickel deposits with different properties [50]

	Electrolyte Composition (g/l)	
	Nickel Sulfamate	Nickel Sulfate
Nickel Sulfamate, $Ni(SO_3NH_2)_2$	300-450	—
Nickel Sulfate, $NiSO_4.6H_2O$	—	225-400
Nickel Chloride, $NiCl_2.6H_20$	0-30	30-60
Boric Acid, H_3BO_3	30-45	30-45
	Operating Conditions	
Temperature (°C)	32-60	44-66
Agitation	Air, Mechanical	Air, Mechanical
Cathode Current Density (mA/cm²)	5-300	30-110
Anodes	Nickel	Nickel
pH	3.5-5.0	2.0-4.5
	Mechanical Properties	
Tensile Strength (MPa)	415-610	345-485
Elongation (%)	5-30	10-30
Vickers Hardness	170-230	130-200
Internal Stress (MPa)	0-55 (tensile)	125-185 (tensile)

The compositions of the main constituents and the usual operation conditions together with typical mechanical properties of deposits are illustrated in Table 2.1 for the Watts and nickel sulfamate solutions.

An additive-free Watts type nickel electroplating solution consists of three main components; namely nickel sulfate, nickel chloride and boric acid. Nickel sulfate are employed to enhance electrolyte conductivity and deposited metal distribution.

Nickel anodes have a tendency to become passive by forming passive oxide films in nickel salt solutions that necessitates the use of halide ions such as nickel chloride, nickel bromide or nickel iodide to ensure 100 % anode dissolution efficiency. Generated passive oxide films on the surfaces of a nickel anode are dissolved by halide ions to form pits on the surface where nickel dissolution continues.

Nickel chloride prevents anode corrosion and enhances the solution conductivity, throwing power, and electroplating thickness uniformity, yet it also increase the internal stress of the deposits by refining grain size and minimizing formation of nodules and trees. The employment of nickel bromide is offered by Tsuru, Y. *et al*. [51] to reduce the internal stress rise instead of nickel chloride; however, this is a debated issue.

The introduction of boric acid which forms a mixture of borate ions and undissolved boric acid in nickel electroplating solutions is employed to stabilize the pH of the solution by dissociating of boric acid to borate ions to compensate discharged hydrogen ions. Boric acid also influences the appearance of the deposits.

Organic stress reducers can also be utilized in electroplating solutions to develop compressive stresses in nickel thin films. The constant concentration of a stress reducer during electroplating can be decreased due to drag-out losses that necessities the regular control of the stress reducer concentration.

Anionic wetting agents or surfactants, i.e. anti-pitting agents, such as sodium lauryl sulfate are used to manipulate pitting or porosity caused by clinging of air and hydrogen bubbles to the surfaces of plated parts and consequently to enhance the corrosion performance of plated articles by decreasing of the surface tension of the plating solution.

One important advantage of electroplating is that the properties of electroplated deposits can be varied in wide ranges with operating conditions such as pH, temperature,

current density and chloride content. The changes in operating conditions result in different trends for the properties of deposits electroplated from Watts or sulfamate based solutions as demonstrated in Figure 2.1. For instance, increasing the temperature in a sulfamate solution leads to a considerable decrease in internal stress of deposits, whereas there is no meaningful sensitivity of internal stress to the temperature shifts for Watts based electroplating solutions.

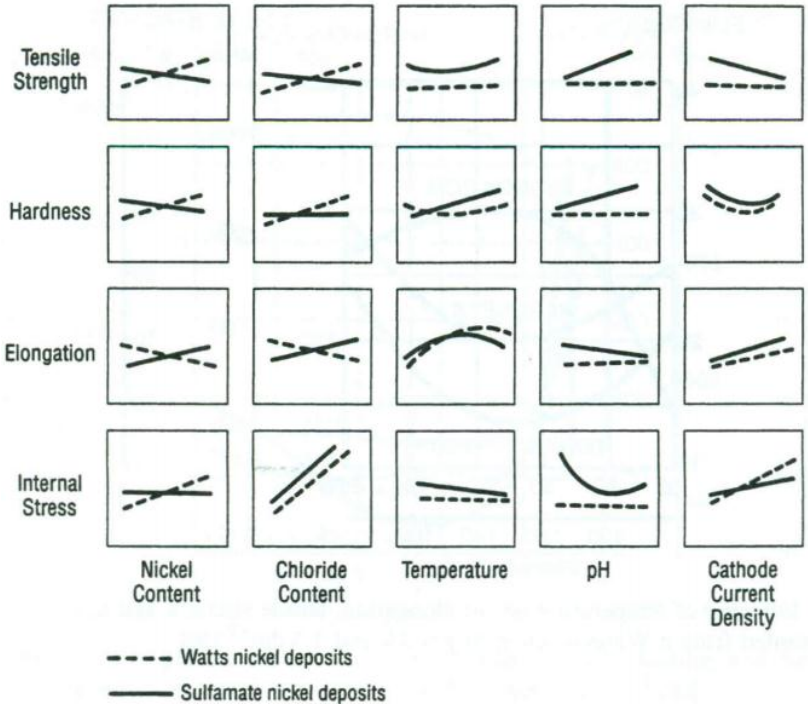

Figure 2.1: Operating conditions have different effects on mechanical properties of parts deposited from nickel sulfate and nickel sulfamate based nickel electroplating solutions (printed from [52]).

In electroplating applications, nickel sulfamate solutions with the attractive properties of low internal stress of the deposits, the high rates of deposition and the improved throwing power are preferred over Watts based nickel solutions. Watts based solutions often require the addition of stress reducing agents to control the internal stress.

Nickel sulfamate deviates from nickel sulfate with an amido group replaced with one of the hydroxyl groups. In the market, nickel sulfamate can be found either as a crystallized form having the formula of $Ni(SO_3NH_2)_2 \cdot 4H_2O$ or prepurified concentrated liquid solution state. High solubility of nickel sulfamate among nickel electroplating electrolytes ensures higher plating rates due to higher nickel metal concentration. Similar to Watts solutions, nickel sulfamate solutions include some amount of nickel chloride to increase anode efficiency especially at high current densities unless sulfur containing anode materials are employed. The operation of nickel sulfamate solutions at temperatures above 70 ^{o}C or at a pH of less than 3.0 can increase the internal tensile stress and hardness of the deposits by

hydrolyzing the nickel sulfamate to nickel ammonium sulfate to form ammonium and sulfate ions.

A concentrated nickel sulfamate process, so-called Ni-speed, containing about 500 to 650 g/l of nickel sulfamate, 5 to 15 g/l of nickel chloride hexahydrate, and 30-45 g/l boric acid was developed to produce low stress nickel electrodeposits at higher current densities without organic additives. In the process, a separate conditioning tank is employed to circulate and purify the sulfamate solution. While a non-activated, sulfur-free anode material is used in the conditioning tank, an activated sulfur-containing anode material is employed in the main tank.

Ni-speed process can produce stress-free nickel deposit using a sulfur-containing nickel anode material to eliminate use of nickel chloride in the solution and by filtering the solution continuously without the use of stress reducer agents that introduce sulfur in the growing layer resulting in embrittlement.

Thus the harsh control on the operation parameters and the concentrations of main constituents, and continuous purification are required to maintain to fabricate deposits with certain mechanical properties especially in the case of nickel sulfamate solutions.

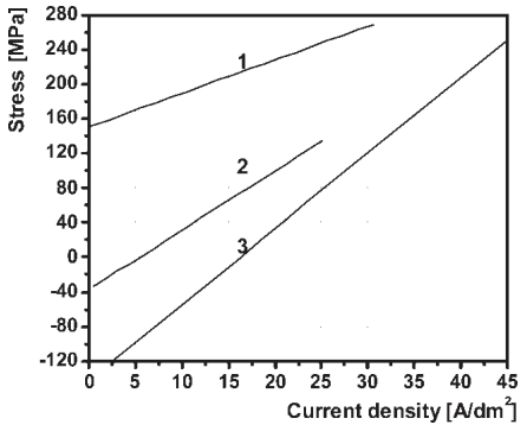

Figure 2.2: The uniform residual stress-current density relationship fort he Watts (1), nickel sulfamate (2) and Ni-speed (3) baths [1]

The uniform residual stress in a thin nickel film as a function of current density for the Watts, nickel sulfamate and concentrated nickel sulfamate solutions are demonstrated in Figure 2.2.

The current density required for fabrication of stress-free nickel thin films and the deposition rate are demonstrated as a function of the operation temperature in Figure 2.3.

Other nickel plating solutions including fluoborate, hard nickel, all-chloride, all-sulfate, sulfate/chloride, high sulfate, black nickel, nickel phosphorus solutions are also employed for functional and electroforming applications.

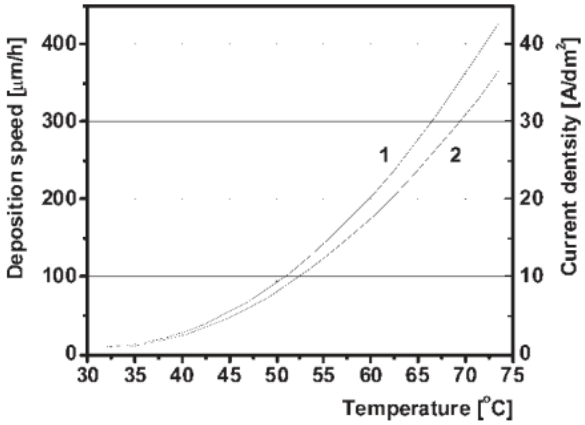

Figure 2.3: Curve 1 and Curve 2 correspond to the electroplating deposition rate and the necessary current density resulting in stress-free deposits respectively for the different operation temperatures of the Ni-speed solution. [1] [9]

Some substrates like silicon or silicon dioxide require two additional layers, namely an adhesion promoting layer such as chromium or alternatively titanium and a seed layer to carry out the electroplating process due to low adhesion and conductivity properties respectively of many metals to the mentioned substrates.

Nickel electroplating can be performed using either a soluble or an insoluble anode. Soluble anodes dissolve to ions which compensate those discharged at the cathode. Strict chemical specifications of commercially available nickel anode materials ensure the purity of electroplating baths. The thickness uniformity of electroplated articles is also enhanced by the right anode choice. Since current and consequently metal on the surfaces of an electroplated part is distributed via the employed anode.

The probable basic way to satisfy anode requirements is to use an electrolytic nickel strip. The nonuniform dissolution preferentially at the bottom and the sides of electrolytic nickel strip results in some vital disadvantages including a continuously changing anode area followed by a steady increase in anode current density and breaking of the anode before completely consumed due to fragile and spongy structure. Interruption of the process during the replacement of electrolytic nickel strip and the size limitations of nickel strip in the market are the other problems related to the use of electrolytic nickel strip in the nickel electroplating process.

The wrought depolarized nickel containing greater than 99% nickel, about 0.5% nickel oxide, and small amount of sulfur was the first anode material offered to get an enhanced performance. Wesley, W. A. [53] investigated the effect of nickel oxide on sulfur distribution was claimed to be a crucial factor in terms of the uniform dissolution and enhanced activity of wrought depolarized nickel by manipulating to the formation of nickel sulfide at grain boundaries resulting in nonuniform anode dissolution by nickel oxide.

Wrought depolarized nickel anodes result in brown nickel film. The employment of anode bags to eliminate metallic particles dissolved at the anode from the solution is recommended to decrease roughness at the cathode. The problems related to nonuniform dissolution and the interruption of the process during the anode replacements are still valid for this type of anode, whereas the manufacturing technique, *i.e.* hot-rolling, of anodes enabling the fabrication of virtually any desired size of anodes ensures the commercial large-scale electroplating applications in deep tanks. Another wrought nickel anode containing about 0.25% carbon and about 0.25% silicon introduced in 1938 leads to nickel plating with less metallic residue.

Titanium mesh baskets strengthened by titanium solid strips and loaded with small pieces of low-cost, primary nickel was developed to compensate problems arising from the use of an electrolytic nickel strip or a wrought depolarized nickel as an anode. The advantages of titanium baskets including the unchanging uniform anode area leading to constant current distribution, the constant anode to cathode distance, no size limitation, longer service life for employed anode bags and, continuous electroplating operation make them attractive in the commercial electroplating applications.

At high anodic overvoltage, the electrolytic nickel anode becomes passive by formation of the nickel oxide on surfaces of the anode leading to the nonuniform dissolution. The dissolution of the anode through pits on the surface results in breaking of the anode due to spongy structure formed at advanced stages of the electroplating.

Various nickel electroplating anode materials have different anode reduction potentials. The potential of an insoluble platinum anode of +1 volt versus saturated calomel electrode (SCE) decreases to +0.2 to +0.4 volt versus SCE when an non-activated nickel anode material is employed in the nickel sulfamate solution with the presence of chlorides. Furthermore, the activated nickel anode has -0.2 volt versus SCE reduction potential. However, the constant potential of 0.2 volt versus SCE can be assumed as the reduction

potential of pure electrolytic nickel under practical plating conditions for chloride containing nickel sulfamate solutions and the rate of dissolution is found independent of the anode potential [54].

In order to enhance the nickel activity in electroplating solutions, investigations focused on finding additives such as sulfur, selenium, tellurium, phosphorus, carbon and silicon to the primary form of nickel for use in baskets have been performed. Sulfur containing electrolytic nickel was determined to be the most active anode material commercially available such that nickel anode dissolves at 100% efficiency even in the absence of chloride ions enabling the elimination of chlorides from solution to reduce the internal stress of deposits by the addition of sulfur additive. High anodic overvoltage results in the nickel oxide film only in the absence of chlorides, whereas with chlorides presenting in the electroplating solution, there is no apparent nickel oxide formation on the surface of sulfur containing electrolytic nickel. Sulfur also reduces the dissolution potential compared to pure electrolytic nickel leading to energy conservation and lower power costs and favors the uniform dissolution. Anode bags are employed to prevent the sulfur in the anode material to get in the electroplating solution.

It is quite probable that consecutive reactions rather than $Ni \rightarrow Ni^{++} + 2e^{-}$ occur in the nickel bath during the electroplating process.

Process quality control involves maintaining the concentrations of the main constituents, *i.e.* nickel metal content, the chloride concentration, the boric acid level, and the concentration of all additional agents within specified limits, controlling pH, temperature, and current density and maintaining the purity of nickel electroplating solutions.

The preparation of an electroplating bath starts with the proper adjustment of the main constituents to the specified concentrations and then continues with the pH adjustment and purification of the solution steps. Measurements to keep the compositions of main constituents and pH of the solution within specified limits and solution purification to prevent the metallic, organic, and gaseous contamination must be performed on a regular basis. Losses of organic addition agents due to drag-out, electrolytic consumption, and the effects of carbon filtration must be compensated.

Traditional techniques for chemical analysis based on titration, precipitation and other wet chemical techniques or more increasingly instrumental techniques such as liquid

chromatography and electroanalytical methods like polarography are employed to keep the compositions of main constituents of an electroplating bath at optimum levels.

The usual rise of the pH of a nickel plating solution during normal operation of the bath is balanced by a regular addition of some amount of a certain acid to the solution. Sulfuric acid and sulfamic acid are recommended for the pH adjustment of Watts and sulfamate solutions, respectively. On the other hand, a pH decrease shows a solution processing problem probably related to a nickel ion concentration decrease.

The estimation of the surface area of the parts to be electroplated in order to calculate the current density and the required time would lead to a consistent predetermined thickness of electroplated nickel. The operation of the electroplating at a fixed voltage is not suggested. The temperature range from 40 ^{o}C to 60 ^{o}C is usually selected for the operation of most commercial nickel plating baths.

In addition to the employment of non-conducting shields and baffles or auxiliary anodes, rack design and placement of components can be optimized to get more uniform electroplating on the surfaces of articles.

Filtered demineralized water should be used to form the solution and renew water lost by evaporation in order to keep the deposition roughness resulted from the precipitation of calcium sulfate at minimum by eliminating particles. The local tap water with high calcium content especially requires this kind of process.

Normal operation of electroplating baths may lead to contamination caused by inorganic, organic and gaseous impurities that may manipulate the mechanical properties of deposits. Continuous filtration and low current density electrolysis at 2 to 5 mA/ cm^2 are employed to eliminate inorganic contaminants introduced from numerous sources such as technical grade nickel salts, hard water, acid dip tanks transfers, airborne dust, corrosion of the tank material through cracks in the lining, corrosion of anode bars, dirt from structures above the tank, and from parts that fall into the solution.

Continuous adsorption through a filter coated with small amounts of activated carbon is applied to remove organic contaminants developed from many sources including sizing from anode bags, uncured rack coatings or stop-off lacquers, adhesives on certain types of masking tape, decomposition products from wetting agents, organic stabilizers in hydrogen peroxide, paint spray etc. The formation of hazes or cloudiness occurring over a broad or

narrow current density range on the surface of a nickel deposit may happen due to organic contaminants.

Gaseous contamination of nickel plating solutions usually consists of dissolved air or carbon dioxide.

The electroplating process may introduce several kinds of defects such as roughness, pitting, blistering, high stress and low ductility, discoloration, burning at high current density areas which need to be overcame. The employment of anode bags to prevent anode residues from entering the solution and the use of purified demineralized water together with continuous filtration of the plating solution would decrease roughness problems initiated from the incorporation of insoluble particles in the deposit.

Clinging of air or hydrogen bubbles to the surface of plated articles leads to pitting. A chemically out-of-balance solution, *i.e.* a solution having too low a pH level or insufficiently agitated solution, may produce hydrogen bubbles. Thus, in addition to the control of the pH and temperature of the solution, the concentration of main constituents of the solution should be kept within specified ranges to minimize pitting.

2.2 Residual Stresses in Thin Films

Residual stress is one of the most investigated thin film mechanical properties that affects and degrades electronic and magnetic properties, performance, structural integrity and long-term stability of the thin films. Buckling, cracking, splintering and sticking problems may arise due to excessive residual stresses in thin films. From the point of view of device design and fabrication, determination of the residual stresses in thin films is necessary to optimize the device performance and to lower fabrication costs. In-plane and out-of-plane displacement of a thin film designed as a moving part in a MEMS application must be particularly controlled to ensure the performance and life-time of fabricated products.

Residual stresses in thin films can be divided into two components; namely thermal stress and intrinsic stress. In multilayered structures, the difference of the coefficient of the thermal expansion of layers results in thermal stresses. However, the employed fabrication technique, deposition conditions such as temperature, pressure, deposition rate and used substrate determine the intrinsic stress for a thin film structure. This necessitates the determination of the intrinsic stress for each film fabricated with different process parameters.

Residual stress in a thin film greatly influenced by deposition conditions and fabrication processes is quantified experimentally using various methods including the conventional wafer curvature method to determine the average stress from the Stoney equation [55], the resonant frequency technique [44, 56], nanoindentation [57], X-ray diffraction [58] and micromachining based techniques.

Among those techniques, the micromachining technique is the most widespread method [59-62]. Released micromachined beams including microbridge and microcantilever deformed by residual stresses after the removal of the underlying sacrificial layer simply provide an *in-situ* means of measurement without special equipment. Then the deformations of microstructures are correlated with residual stresses in the deposited thin films using analytical or numerical schemes.

Micromachining-based residual stress measurement methods including buckling technique, rotating technique, micro strain gauge and long short beam strain sensor were reviewed by He, Q. *et al*. [48]. Comparison of the micromachining-based residual stress measurement techniques in terms of accuracy and resolution was carried out by fabricating micromachined structures for each technique giving the best results for the micro strain gauge and the long-short beam strain sensor for the same film.

In the general case, growth process of thin films may end up with non-uniform complex residual stress distributions over the film thickness or the investigated volume which might be determined by grazing incidence X-ray techniques [63], Raman spectroscopy techniques [64] or the ion beam layer removal (ILR) method [65]. The latter technique evaluates the local residual stress distributions by monitoring the deflection of a focused ion beam (FIB) fabricated microcantilever while ion beam is used to remove thin films gradually to decrease the thickness of the fabricated cantilever.

Residual stresses in microstructures can be modeled with the combination of uniform stress (σ) and stress gradient across the thickness ($\nabla\sigma$). Uniform residual stresses are found in either tensile (contractile) or compressive (expansive) form in nature. Uniform distribution of residual stress across the cross section of a microstructure modeled with uniform residual stress results in in-plane expansion or contraction at free ends of the microstructure in the case of relief. However, relief of a residual stress gradient induces a bending moment leading to the formation of the curvature of a fabricated microstructure.

Thus the determination of the bending profiles of a microstructure can be used to evaluate the residual stress gradient in thin films. In the literature, there are also some employed algorithms such as the one developed by Fang, W. *et al.* [66] to evaluate the uniform residual stress from the profile of microcantilever.

Guckel *et al.* [67] employed the classical Euler buckling model to calculate the uniform residual stress by determining of a specific critical length of a compressively stressed microbridge existing between prebuckling and postbuckling stages. This model is improved by Fang *et al.* [68] by considering nonlinearity and imperfection to estimate the profile and the amplitude of postbuckling beam to compute the uniform residual stress in the beams. This latter model was employed to determine the uniform strain in thin postbuckled films of SiO_2 [68, 69]and Cr [62] from the beam amplitude at different length.

Although a complete theory is not yet developed to account for residual stresses in thin film, there are some proposed mechanisms in the literature that explains the residual stress generation during the film growth including electrocrsytallization (crystallite joining), impurity codeposition, lattice effects and thermal stresses [70, 71].

The electrocrsytallization mechanism assumes that the microstructure of an electrodeposited layer change from nanocrystalline state to recrystallization state with time leading to a grain boundary density decrease and consequently material volume decrease which results in tensile stress development in thin films.

Bhandari, A. *et al*. [72] correlated tensile island coalescence stress with the thin film growth stages. The solid curve in Figure 2.4 corresponds to a usual stress evolution as the thin film grows. The initial almost stress-free state of the film turns into remarkable tensile stresses when growing islands start to contact each other. This considerable tensile stress formation is related to elastic deformation of the islands. The difference in the grain and surface energies determines the magnitude of the resulting tensile stress.

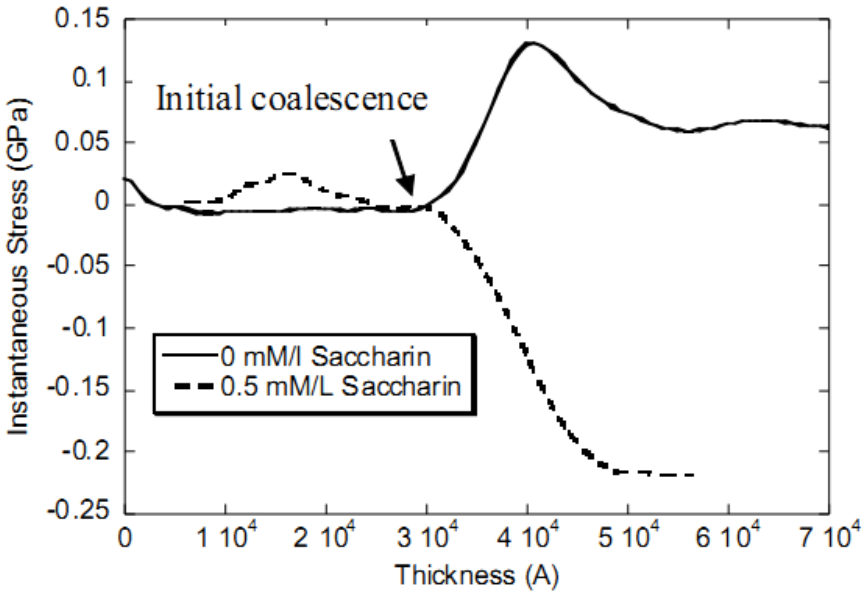

Figure 2.4: The thin nickel film residual stress profiles with/without saccharin additives as the thin film grows [72]

In addition to external sources, impurities can also be generated from internal sources. Some secondary reactions taking place in a fabrication chamber may generate by-products that are trapped in the growing film. This trapped foreign materials end up with some distortions in the crystal structure of a host material leading to residual stresses. Hydrogen is the most common impurity produced by secondary reactions in an electroplating bath. A small portion of an applied current is employed to discharge hydrogen ions from water when cathode efficiency is lower than 100%. That means inevitably there is some hydrogen formation in each electroplating bath. At first, trapped hydrogen molecules cause compressive residual stresses in thin films; however, tensile stresses are generated instead of compressive stresses as trapped hydrogen molecules diffuse out. In nickel electroplating literature, the effect of the codeposition of halide ions such as chlorine and bromide, and sulfur is particularly investigated. Studies indicate that halide ions and sulfur import tensile and compressive stresses in electroplated Ni thin films, respectively.

Thus nickel chloride concentration should be minimized or the use of nickel chloride in the bath is completely eliminated. The complete removal of nickel chloride leads to the anode passivation problem. This challenge can be overcome by employing of sulfur containing nickel anode material with about 0.01 % sulfur to eliminate anodic oxidation. However, an anode bag must be used to prevent sulfur particles dissolved from the sulfur containing anode to enter the electroplating solution.

As the lattice parameter difference between the substrate and growing film increases, the growing film is more likely to have grain boundaries or impurities leading to the residual stress formation.

The coefficient of thermal expansion difference between the substrate and the grown thin film for multilayered films or high local temperatures during the deposition introduce also residual stresses.

In the case of multilayered films in order to fabricate straight films, zero stress in each layer is not a requirement if the modulus of elasticity and the coefficient of thermal expansion of each layer are similar. Instead, the same level of residual stress in each layer also leads to straight microstructures. Matovic J. [73] utilized this approach to fabricate flat microcantilevers consisting of thermally grown SiO_2 and electroplated nickel layers.

However, mechanisms such as grain rotation induced texture changes, recrystallization or grain growth, grain boundary shifts, creep and escape of trapped H_2 gas change the residual stress in a thin film even after the process is completed.

2.3 Residual Stress Reduction

Pulse plating is utilized to reduce the residual stresses in electrodeposited nickel layers instead of traditional DC plating by applying a negative potential to the cathode at a certain frequency that can be followed by the application of a positive potential. During the application of the negative charge portion of the cycle, nickel and other co-deposited materials including halides such as Cl^- ions coming from nickel chloride and hydrogen molecules and other organic, inorganic or gaseous impurities existed in the bath are deposited to form the thin film, whereas the application of a positive potential corresponds to the compensation period at which the built-in stress in the film is reduced by eliminating foreign particles existing in the layer. Pulse plating also has an effect on the microstructure of electroplated thin films as shown by Fritz T. *et al.* [23]. Residual stress in a nickel film can be tuned with the ratio of negative to positive current as shown in Figure 2.5.

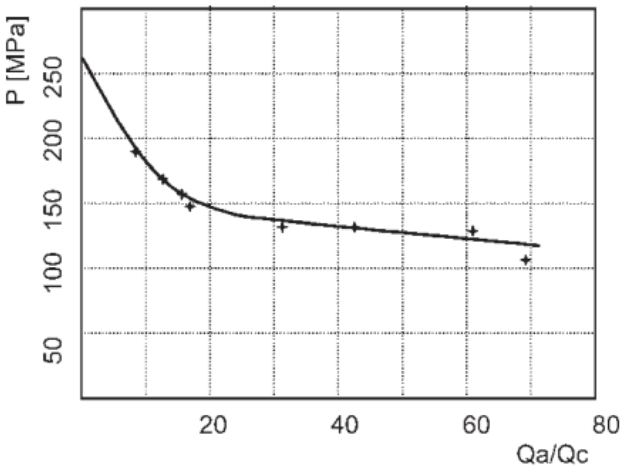

Figure 2.5: Residual stress in a nickel film as a function of the ratio of negative to positive current flow deposited from a Watts bath [74].

Chan, K. C. *et al.* [75] also investigated the influence of the pulse plating on the residual stress and microstructure of electrodeposited nickel films. Pulse plating experiments carried out to determine thin film residual stresses by an x-ray stress analyzer at various pulse frequencies, current densities and duty cycles, *i.e.* ratio of application time of current for a cycle to a period of the cycle ($t_{on}/(t_{on}+t_{off})$). As demonstrated in Figure 2.6, thin films fabricated from a nickel sulfamate-based bath using pulse plating technique have significantly lower residual stresses than the ones deposited by DC plating method.

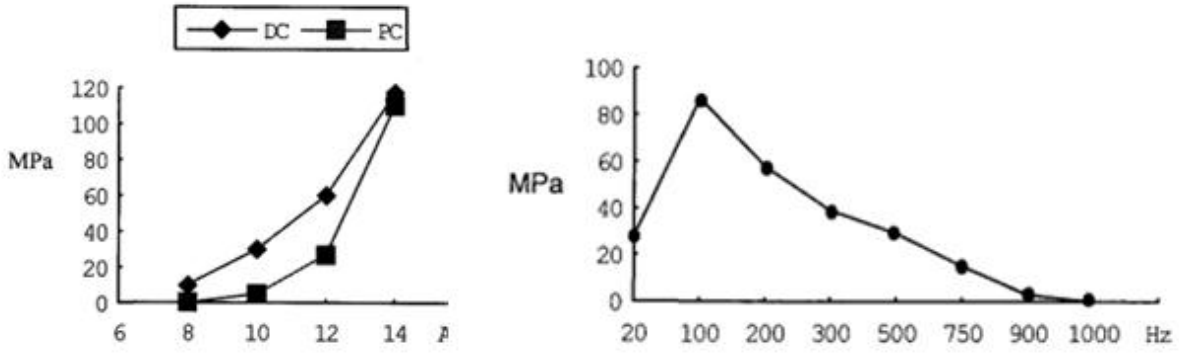

Figure 2.6: The effect of current density on the residual stress for the nickel thin film produced using DC and pulse current plating (on the left) and the effect of pulse frequency on the internal stress of the pulse plated nickel thin film (on the right) [75].

The effect of the employed pulse frequency limited by the capacitive effect formed at the electrode-electrolyte interface on the residual stress of fabricated nickel thin films is also demonstrated in Figure 2.6. The hydrogen content measurement carried out at the current density of 8 A/dm^2 revealed that the pulse plated film had less than one-third of hydrogen content of DC plated film. During the positive or off duration of pulse plating, the higher

diffusion or electron potential of hydrogen molecules over nickel leads to relatively higher hydrogen discharge than nickel discharge which results in lower residual stress in thin nickel films.

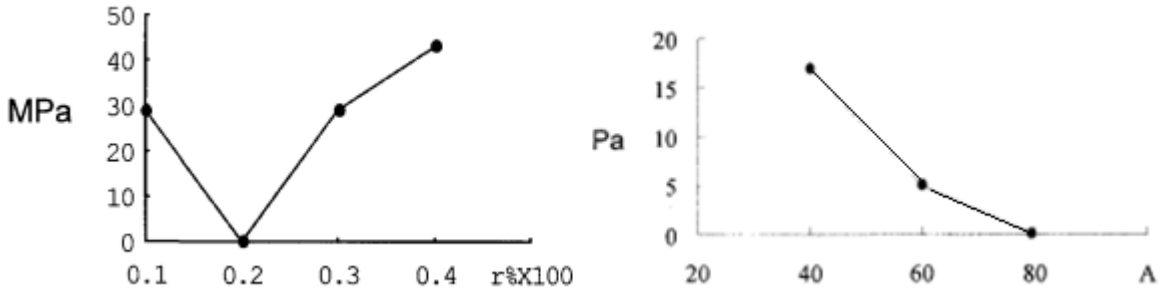

Figure 2.7: Residual stress as a function of the duty cycle (on the left) and positive peak current density (on the right) [75]

The decrease in the duty cycle to a certain point promotes the residual stress reduction as indicated in Figure 2.7. Figure 2.7 also implies that residual stress is inversely proportional to the positive peak current density.

The nickel sulfamate-based concentrated nickel electroplating solution, *i.e.* Ni-speed, may lead to a stress-free nickel thin film if a high state of purity of the solution achieved by continuous filtration/purification of the solution is maintained. The elimination of the foreign particles in the solution may be performed in a separate conditioning tank where the filtration and circulation of the solution are performed continuously.

In nickel electroplating baths, it is almost always valid that the compressive residual stresses in thin films can be obtained only by organic stress reducers. Sulfur is the most investigated and effective element that introduces compressive stresses in the deposited nickel layers. Some sulfur containing aromatic organic compounds such as o-sulphobenzoic imide (saccharin), paratoluene sulphonamide, benzene sulphonamide, benzene monosulphonate (sodium salt), ortho sulphobenzaldehyde (sodium salt) and naphthalene 1, 3, 6-trisulphonate (sodium salt) are used in commercial applications as stress reducing agents.

Among all stress reducing agents, saccharin is the most popular and effective one used in the form of sodium saccharin salt at a concentration of 0.5 – 4.0 g/l. The effect of saccharin additive on the stress evolution profile as thin film grows is also demonstrated with the dashed line in the Figure 2.4. There is a considerable change in the stress state of the fabricated film after the outset of the island coalescence process. The use of saccharin additive in the electroplating bath leads to the development of compressive stresses after the initial

coalescence point. It was claimed that the tensile stress formation during the island coalescence process is prevented by saccharin by decreasing the difference between the grain boundary and surface energies. The decrease in the tensile stress evolution during the coalescence process, which is found proportional with saccharin concentration in the electrolyte, makes the mechanism of compressive stress generation, being unaffected from saccharin, superior [72].

The variation of the residual stress as a function of the applied current density deposited from an electroplating bath containing a certain concentration of saccharin additive as a stress reducing agent can be seen in Figure 2.8. The incorporation of sulfur in a nickel layer during the electroplating process dissolved from any of above organic stress reducers present in the bath results in embrittlement at temperatures over 200 ^{o} C. This embrittlement temperature puts a temperature limit for the safe operation of the sulfur incorporated nickel thin film containing device [73].

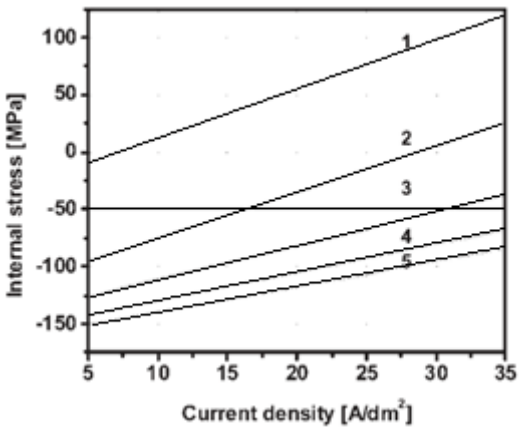

Figure 2.8: Residual stress as a function of current density with a saccharin concentration of 1.0 g/l, 2.0 g/l, 3.1 g/l, 4.2 g/l or 5.3 g/l respectively [73]

Substrate on which a thin electroplated film grows also has an effect on texture and microstructure of electroplated layers influencing the built-in residual stresses in the thin film. As the difference of lattice parameters between the substrate and the electroplated layer increases, the deposited thin film is more likely to have voids, unusual microstructures or textures leading to different mechanical properties such as the modulus of elasticity, residual stress. The substrate effect on the texture and microstructure of growing electroplated nickel microcantilevers was investigated by Fritz, T. *et al*. [23]. Thus it may be an option to use nickel or a layer with similar lattice parameters or microstructure with the nickel as a seed layer to reduce the residual stress in electroplated thin films. But here it should be also noted

that the influence of the substrate introduced into the initial seeds of a growing layer decays as the current density keeps rising [26].

To sum up, some of mentioned techniques employed for the reduction/manipulation of residual stresses in electroplated microstructures are summarized in Table 2.2 with some of representative studies from the literature.

Table 2.2: Some of the techniques can be used to adjust the residual stress in electroplated thin films

Adjusting and maintaining electroplating bath parameters (current density, temperature and pH) accurately	[1]
Pulse electroplating	[75]
Employing organic stress reducing agents	[72]
Sonication	[76]
Compatible substrate employment	[23]
Continuous filtration & circulation	
Elimination or replacement of nickel chloride from the solution with sulfur containing anode	[51]
Employment of an effective anode bag	
The employment of materials with a similar coefficient of thermal expansion for multilayered coatings	[73]

2.4 Derivation of the Residual Stress Gradient for Single Layer Cantilevers

In this subsection, the residual stress gradient for a single layered microcantilever will be derived by employing the small displacement approach. The curvature of the single layered microcantilever demonstrated in Figure 2.9 can be written as follows;

$$\frac{1}{R} = \frac{d^2y}{dx^2} = \frac{M}{EI} \tag{2.3}$$

where M and R are the induced moment along the z axis at any cross section due to the residual stress gradient and the radius of curvature, respectively. E is the modulus of elasticity of the fabricated material. I stands for the moment of inertia. Integrating Eqn. (2.3) twice;

$$\frac{dy}{dx} = \frac{M}{EI}x + c_1 \tag{2.4}$$

The boundary condition of $\frac{dy}{dx}\Big|_{x=0} = 0$ dictates that c_1 equals to zero. Then,

$$y = \frac{M}{2EI}x^2 + c_2 \tag{2.5}$$

The constant of c_2 becomes zero with the boundary condition of $y|_{x=0} = 0$. Thus, the bending of the cantilever along the length of the cantilever will be defined as follows;

$$y = \frac{M}{2EI}x^2 \tag{2.6}$$

or the maximum bending at the tip of cantilever will be;

$$\delta = \frac{M}{2EI}L^2 \tag{2.7}$$

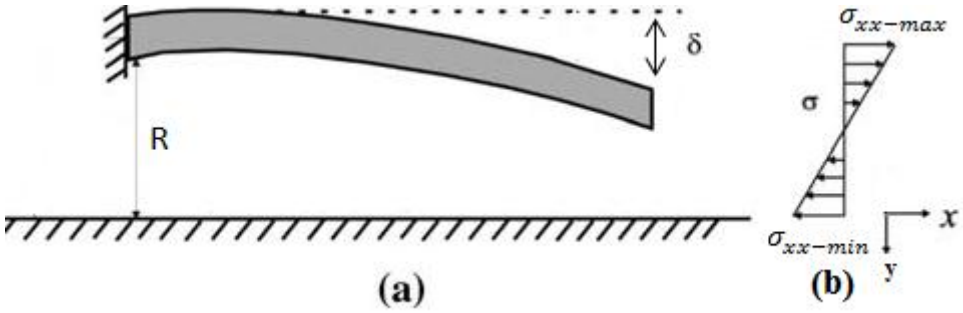

Figure 2.9: The bending of the microcantilever due to negative residual stress gradient (a) and the assumed linear distribution of the residual stress (b)

The force and moment equations for a single layered microcantilever can be expressed as follows;

$$F_x = \iint \sigma_{xx} dA = 0 \tag{2.8}$$

$$M_z = \iint (y - c)\sigma_{xx}\, dy\, dz \tag{2.9}$$

In the above equations the residual stress (σ_{xx}) can be expressed along the y axis, if the distribution of the residual stress across the thickness of the microcantilever is assumed to be linear (Figure 2.9).

$$\sigma_{xx} = \sigma_{xx-max} - \frac{\sigma_{xx-max} - \sigma_{xx-min}}{t}\, y \tag{2.10}$$

The position of the neutral axis along the thickness of the microcantilever will firstly be determined.

$$\sigma_{xx}|_{y=c} = \sigma_{xx-max} - \frac{\sigma_{xx-max} - \sigma_{xx-min}}{t}\, c = 0 \tag{2.11}$$

$$\sigma_{xx-max}\left(1 - \frac{c}{t}\right) + \sigma_{xx-min}\frac{c}{t} = 0 \tag{2.12}$$

Inserting the σ_{xx} into the force equilibrium leads to;

$$F_x = \iint \left(\sigma_{xx-max} - \frac{\sigma_{xx-max} - \sigma_{xx-min}}{t}\, y\right) dA = 0 \tag{2.13}$$

$$= w \int \left(\sigma_{xx-max} - \frac{\sigma_{xx-max} - \sigma_{xx-min}}{t}\, y\right) dy = 0 \tag{2.14}$$

$$= \sigma_{xx-max}\, y|_0^t - \frac{\sigma_{xx-max} - \sigma_{xx-min}}{t}\, \frac{y^2}{2}\Big|_0^t = 0 \tag{2.15}$$

$$\sigma_{xx-max} = -\sigma_{xx-min} \tag{2.16}$$

Plugging of Eq. 2.16 into Eq. 2.12 results in the position of neutral axis along the thickness of the microcantilever.

$$\left(1 - \frac{c}{t}\right)(\sigma_{xx-max}) + \frac{c}{t}(-\sigma_{xx-max}) = 0 \tag{2.17}$$

$$c = \frac{t}{2} \tag{2.18}$$

The moment equation together with Eq. 2.7 provides the deflection at the tip of the cantilever.

$$M_z = w \int \left(y - \frac{t}{2}\right)\left(\sigma_{xx-max} - \frac{2\sigma_{xx-max}}{t} y\right) dy \tag{2.19}$$

$$= w \int_{y=0}^{y=t} \sigma_{xx-max}\, y - \frac{2\sigma_{xx-max}}{t} y^2 - \frac{\sigma_{xx-max} t}{2} + \sigma_{xx-max}\, y \tag{2.20}$$

$$M_z = -\frac{1}{6} w \sigma_{xx-max} t^2 \tag{2.21}$$

$$\delta = \left(-\frac{1}{6} w \sigma_{xx-max} t^2\right) \frac{1}{2E \frac{1}{12} w t^3} L^2 \tag{2.22}$$

$$\delta = -\frac{\sigma_{xx-max} L^2}{Et} \tag{2.23}$$

By utilizing the stress distribution shown in Figure 2.9, the residual stress gradient can be related to the maximum residual stress as follows;

$$\nabla\sigma = -\frac{(\sigma_{xx-max} - \sigma_{xx-\min})}{t} = -\frac{2\sigma_{xx-max}}{t} \tag{2.24}$$

$$\sigma_{xx-max} = -\nabla\sigma \frac{t}{2} \tag{2.25}$$

By replacing the maximum residual stress with the above expression, the residual stress gradient becomes;

$$\delta = \frac{\nabla\sigma L^2}{2E} \tag{2.26}$$

or;

$$\nabla\sigma = E \frac{2\delta}{L^2} \tag{2.27}$$

Thus the residual stress gradient for a monolayer cantilever having a certain length can be determined by determining the tip deflection and the modulus of elasticity of the cantilever. However, both of these parameters depend on employed fabrication technique and operation conditions.

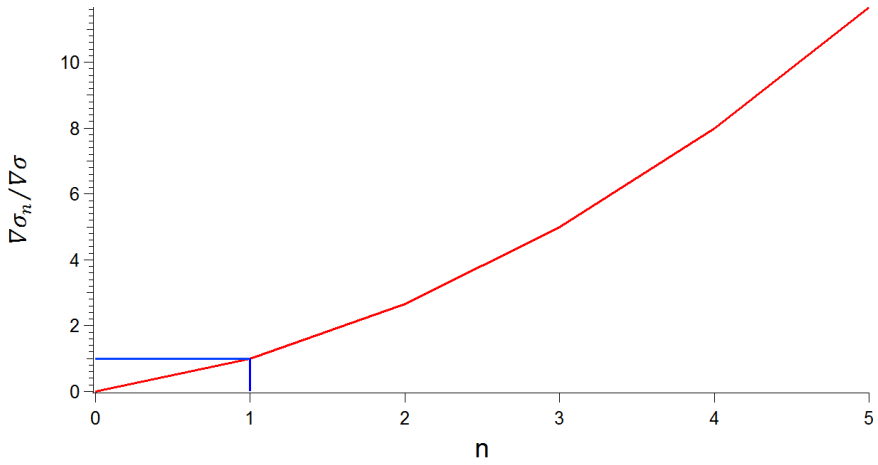

Figure 2.10: The ratio of stress gradients whether n degree nonlinear or linear residual stress is assumed across the thickness

In the above derivation of the stress gradient, the distribution of the residual stress across the thickness of the microcantilever is assumed to be linear (Figure 2.9). If the residual stress is assumed to have the following form across the thickness of the microcantilever;

$$\sigma_{xx} = A(y - c)^n + B \tag{2.28}$$

where *A*, *c* and *B* are constants determined by the application of boundary conditions and *n* is the odd degree of nonlinear distribution of the residual stress over the thickness, then the stress gradient becomes;

$$\nabla\sigma_n = E\frac{2\delta}{L^2}\frac{(n+2)n}{3} \tag{2.29}$$

Figure 2.10 demonstrates the deviation of the stress gradient from the stress gradient derived for the linear residual stress distribution case. As seen in Figure 2.10, while the *n* value approaches 5, the value of this new stress gradient becomes one order of magnitude higher than the value of stress gradient calculated with the linear residual stress distribution assumption. However, it is reasonable to assume the linear stress gradient distribution across very thin films such as in our case of 1-µm-thick single-layer nickel thin films.

Chapter 3: Characterization of the Stress Gradient of Thin Nickel Films

In this chapter, as a major contribution of this thesis to the literature, the residual stress gradients in electroplated 1-µm-thick nickel films are explored as a function of electroplating process parameters of current density and solution temperature. Microcantilevers are employed as a measurement tool for the residual stress characterization experiments by determining tip deflections of microcantilevers and modulus of elasticity of nickel. Zero residual stress gradient, i.e. straight cantilevers, is achieved for certain combinations of fabrication parameters.

Cantilever tip deflection measurements are carried out using various techniques including interferometric lens, optical microscope with a calibrated stage and white light interferometry (WLI) for samples electroplated either by DC or pulse plating. Moreover, temporal evolution of tip deflection of cantilevers under room conditions is demonstrated.

Furthermore, nickel film thickness variation in the range of 700 – 1500 nm due to the employed high current density of 20 mA/cm^2 is correlated with corresponding cantilever tip deflections.

Finally as microstructural analyses, nickel film characteristics together with average grain sizes at preferred crystallographic orientations are determined by XRD measurements of samples having different nickel film thicknesses. Then SEM grain morphology investigation from top surface and cross sections of nickel films are performed.

The following initial brief overview of the employed fabrication flow and utilized mask layout is followed by the experimental results.

3.1 Mask Layout

Since the photolithography technique is used to pattern cantilever structures on silicon wafers, a new mask is designed with a commercial layout editor to work with 4” silicon

wafers and printed on a glass. In order to quantify the stress gradient of micron-sized cantilever more accurately, longer cantilevers are aimed to be produced. The lithography mask is designed to consist of 42 dice of 1 cm x 1cm dimensions in order to carry out electroplating experiments separately. In the layout, three types of cantilevers having widths of 10, 20 or 30 µm are designed with an aspect ratio of 10. Each die consists of only one type of cantilever with a specific width and length. Cantilevers are attached to 250 µm thick anchors at their support to provide adequate support against undercut in release. The designed mask together with the layout of a representative chip and cantilevers is shown in Figure 3.1.

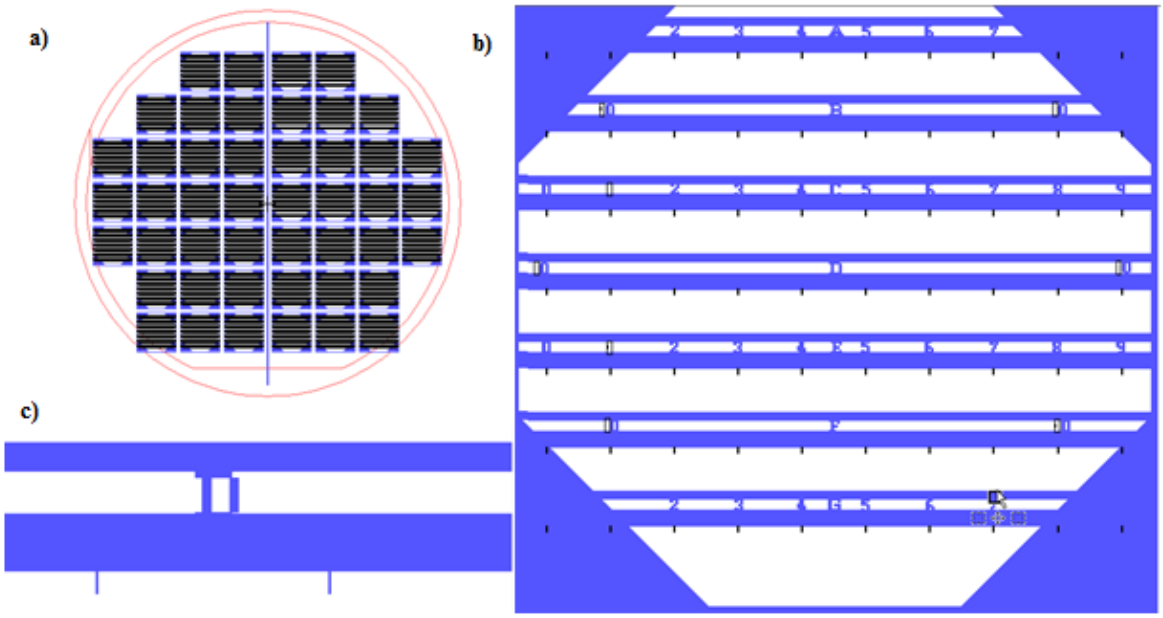

Figure 3.1: a) the designed photolithography mask consisting of microcantilevers having lengths of 100, 200 and 300 um with a 10 aspect ratio b) the layout of a die with cantilever rows and labels c) the close-up picture of cantilevers.

Each die includes 4 contact points to enhance the deposition uniformity in the electroplating process. Anchors on the mask are aligned parallel to the flat of a (100) silicon wafer which is to minimize the undercut problem of silicon supports during wet anisotropic etching of silicon. Each die, labeled with letters and numbers to locate each cantilever and record specific values of them easily, consists of 58 cantilevers which forms several arrays of cantilevers.

3.2 Fabrication Flow

The employed fabrication flow shown in Figure 3.2 is essentially a single-mask lithographic process which mainly consists of RF sputtering, photolithography, nickel

electroplating and wet release of fabricated microcantilever stages. Each step of fabrication flow is broadly elaborated in the theses of Yavuz, S. [77] and Ozturk A. [78],. Here, recent modifications of the employed fabrication flow from previous utilized schemes will be emphasized. The details of the fabrication flow can be found in Appendix A0.

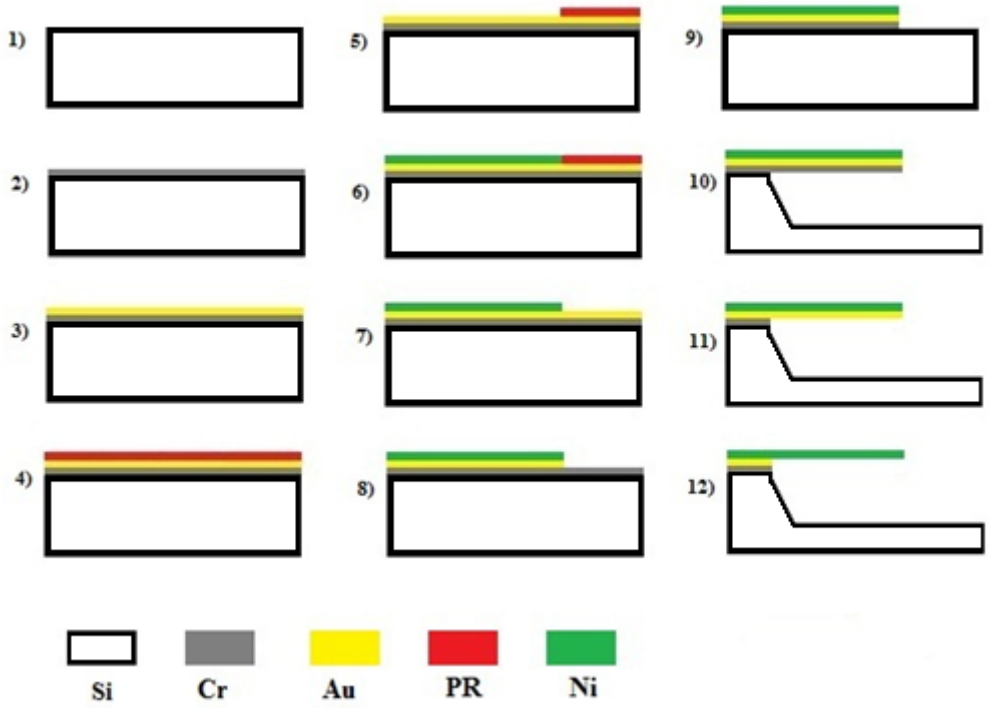

Figure 3.2: The employed fabrication flow to fabricate released single layer nickel microcantilevers. Fabrication flow is composed of wafer cleaning (1), Cr and Au layer deposition by RF sputtering (2,3), spin coating and development of a positive PR (4, 5), electroplating of nickel (6), removal of the PR (7) and release of microstructures (8, 9, 10, 11, 12)

Cleanness of silicon wafers prior to fabrication is ensured with the standard (RCA1) cleaning at 80 °C for 10 minutes followed by the diluted HF (5%) treatment to get rid of organic contamination and oxide layer on the surface, respectively. AZ 1514H positive photoresist rather than AZ 5214 negative photoresist is employed in the fabrication process to enhance lithographic uniformity across a 4" silicon wafer. Soft bake recipe of the employed photoresist is modified from at 110 °C for 10 minutes to 100 °C and 2 minutes in accordance with the product specifications. The photoresist specification proposes 1 minute soft-bake time per each spin-coated 1 µm photoresist film thickness at 100 °C on a hotplate. As a result, shorter development time together with easier removal of photoresist from wafer surface is achieved.

Since electroplating is performed chip by chip, after defining microcantilever patterns on 4" single crystalline silicon wafers by photolithography, wafers are cut into 1 cm x 1 cm

dice using a OEG MR200 type scriber instead of diamond pen. Employment of the scriber increases cutting efficiency with a constant specific force and depth and ensures cuttings at desired precise intervals.

Nickel electroplating is carried out with a nickel sulfamate solution consisting of 600 g/l nickel sulfamate ($Ni(SO_3NH_2)_2.4H_2O$), 10 g/l nickel chloride ($NiCl_2.6H_2O$) and 40 g/l boric acid (H_3BO_3). pH of the employed solution is adjusted from 5.2 to 4.0 by adding approximately 10 g of sulfamic acid.

It is observed that each crocodile results in significant thickness variation at adjacent regions to a contact point. Thus electroplating is performed with two crocodiles placed diagonally rather than four crocodiles in order to enhance nickel thickness uniformity across chips. Furthermore, anode-cathode distance is minimized and fixed to approximately 2 cm to boost nickel deposition rate.

At the end of the fabrication flow, each chip is immersed in water, acetone and IPA subsequently for at least 5 minutes and dried at room temperature on a flat surface to prevent stiction of microcantilevers as much as possible.

The electroplating trials at non-additive pH level of approximately 5.4 of the employed nickel sulfamate solution lead to some contamination on nickel surfaces. The SEM image of an introduced particle on a nickel surface is shown in Figure 3.3.

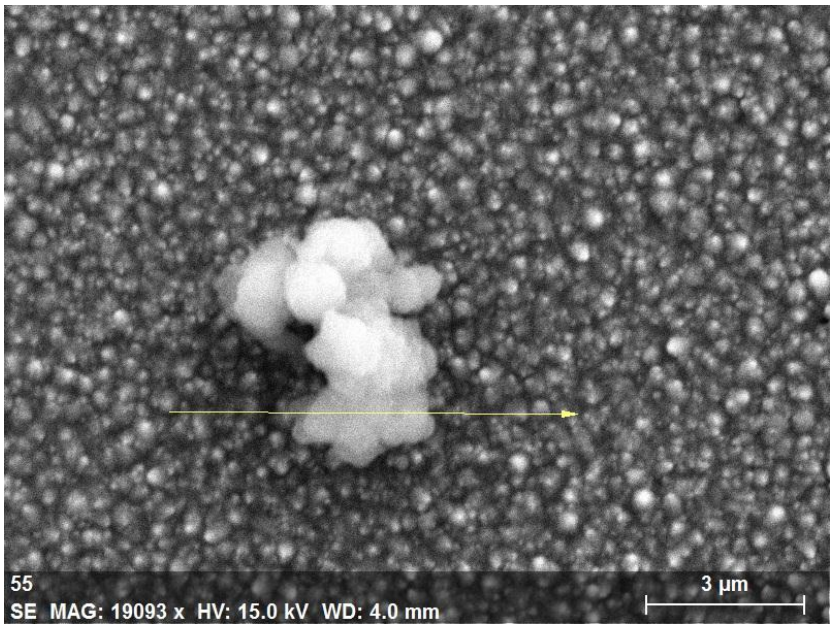

Figure 3.3: The SEM image of a contaminating particle on a nickel surface

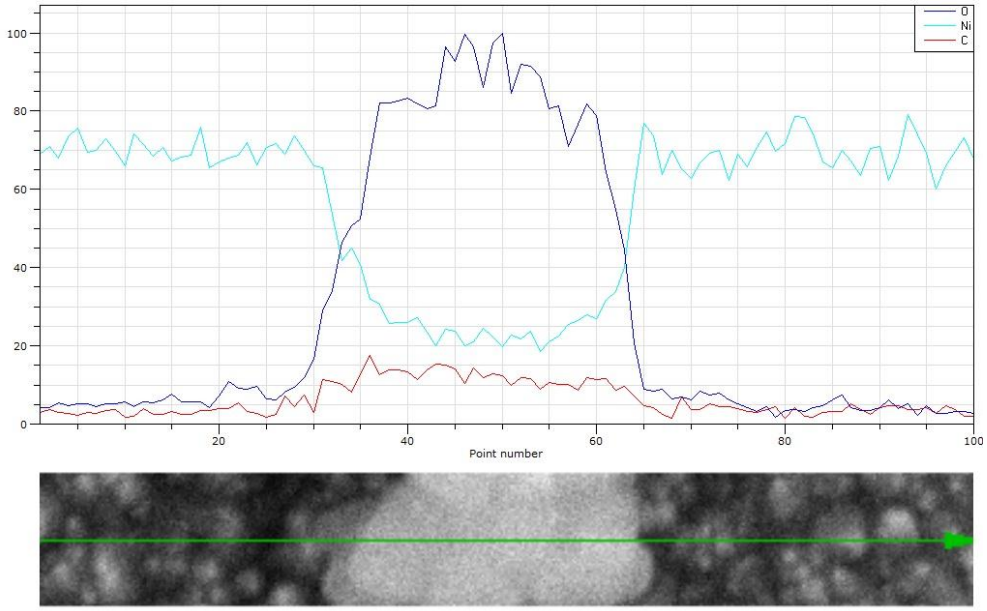

Figure 3.4: EDS elemental analysis of a formed particle on a nickel surface at non-additive electroplating solution

Energy-dispersive X-ray spectroscopy (EDS) analysis is carried out for elemental characterization of emerged particles. As shown in the Figure 3.4, such an analysis demonstrates an oxide formation at proximity of the particle illustrated in Figure 3.3. The EDS spectrum of the same particle also confirms development of nickel oxide particle formation on nickel surfaces (Figure 3.5).

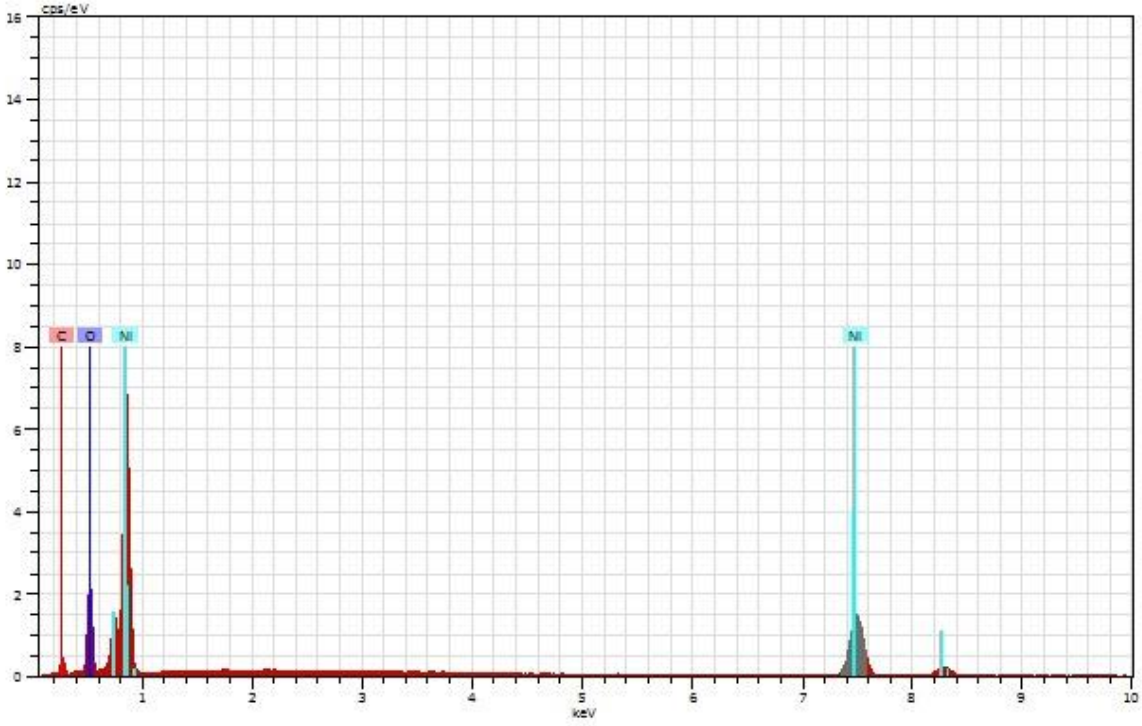

Figure 3.5: EDS spectrum of the same particle demonstrates explicit nickel and oxide peaks

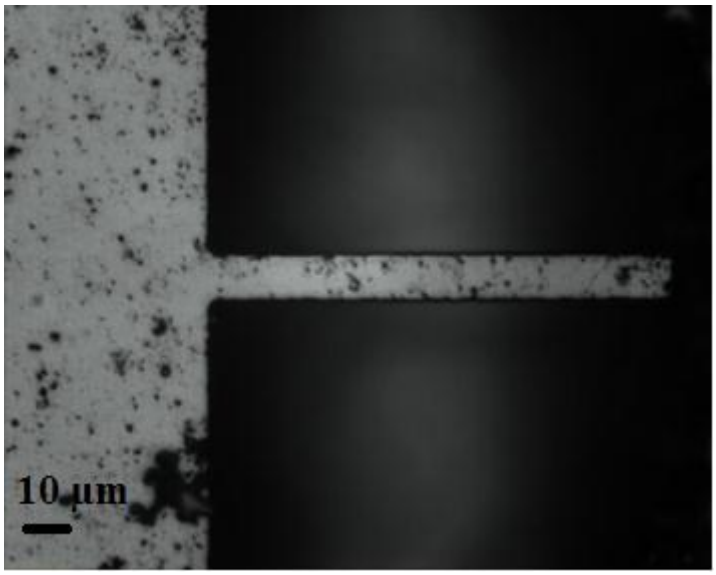

Figure 3.6: Certain operation conditions of electroplating result in oxide precipitation on nickel surfaces during electroplating even at a lesser pH level of 4.0, photo taken from a cantilever fabricated at 60 °C and 1 mA/cm^2 after the electroplating process

Adjusting of the pH of the employed nickel sulfamate solution from approximately 5.40 to 4.00 by addition of sulfamic acid mostly eliminates nickel oxide formation issue for most of the chosen deposition conditions. However, lower current densities and higher temperatures still promote oxide formation on nickel surfaces during electroplating even at pH level of 4.0 of the employed electroplating solution.

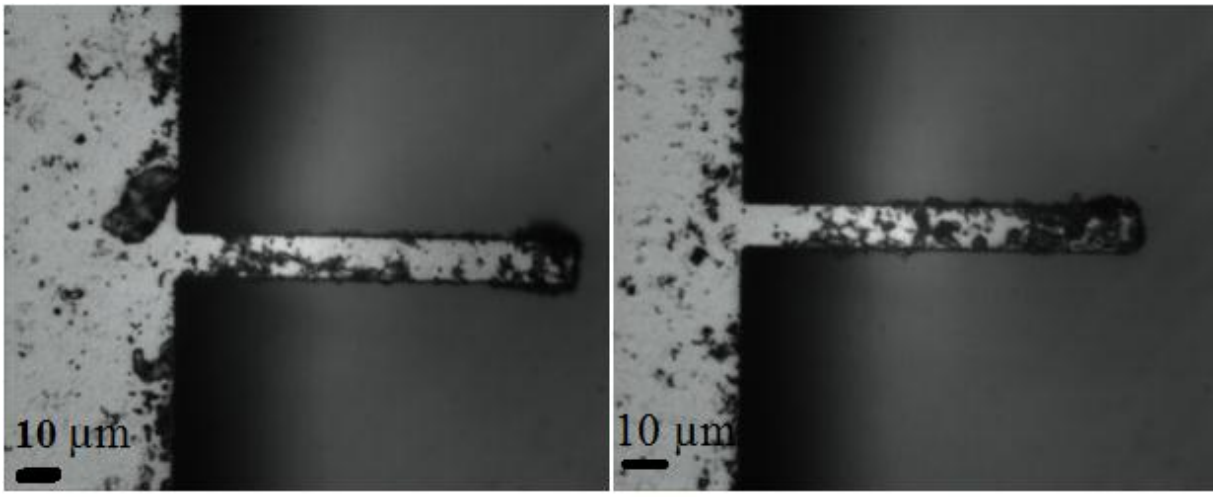

Figure 3.7: Released cantilevers suffered from nickel oxide and iodine precipitation formation on nickel surfaces

Furthermore, if the iodine content within the employed Au etchant does not diffuse properly from nickel cantilevers, such as in the case of removal of gold layer from beneath cantilevers, another precipitation seen in Figure 3.7 results in extra stresses on cantilevers.

This problem can be minimized by employing cantilevers with lesser widths. Therefore cantilevers having the width of 10 µm rather than 20 or 30 µm are preferred in stress gradient characterization experiments. An example of a successfully fabricated cantilever can be seen in Figure 3.8.

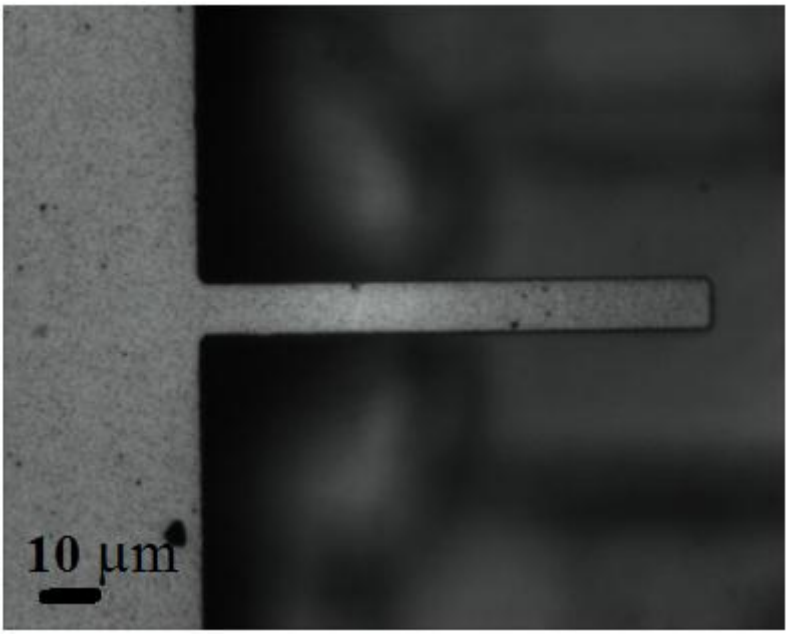

Figure 3.8: A successful cantilever fabrication corresponds to less nickel oxide formation on a nickel surface and no iodine precipitation coming from Au etching process.

3.3 Electroplating Thickness Measurement & Variation

Since the objective of this work is to characterize stress gradient in nickel microcantilevers as a function of current density and temperature, sensitive adjustment of applied current density is necessary. In order to determine applied current density, precise measurement of plated area is required. The plating area is composed of electroplated surfaces on each crocodile and employed chip. As seen in Eq. 2.2, electroplating thickness is proportional to applied current density, i.e. $J=I/A$, thus comparison of electroplating thickness of fabricated nickel layer with electroplating thickness value of similar electroplating bath in literature fabricated at the same temperature and time, applied current density can be approximated. With the knowledge of applied current density, total electroplated area can be calculated from employed current.

In this study, a wide operation range is chosen to investigate stress gradients: three current densities namely 1, 5 and 20 mA/cm^2 and three temperatures namely 30, 45 and 60 °C. Thus there are 9 different cases which are studied with 9 separate samples fabricated both with DC

and pulse electroplating. Samples used to characterize stress gradient of nickel layers are listed in Table 3.1.

Table 3.1: Samples are named after employed solution temperature and current density

Sample Name	Fabrication Parameters	
	Solution Temperature (°C)	Current Density (mA/cm^2)
30-1	30	1
30-5	30	5
30-20	30	20
30-20-2	30	20
45-1	45	1
45-5	45	5
45-20	45	20
60-1	60	1
60-5	60	5
60-20	60	20

Thickness of microcantilevers is tried to be held constant at 1 µm, however, there is considerable thickness variation especially at 20 mA/cm^2 current density. Thus the center of all chips is adjusted to have 1-µm-thick cantilevers. Due to this thickness non-uniformity, 15 cantilevers across each chip are chosen to determine exact plating thickness. Afterwards the deflection and resonance frequency of the same 15 cantilevers are determined to reflect the stress gradient for each case precisely.

Figure 3.9: Employed pulse reverse power supply

The pulse plating experiments are carried out using a pe86cb type reverse pulse power supply from Plating Electronic shown in Figure 3.9. In pulse electroplating, the square wave pattern presented in Figure 3.10 is employed with a duty cycle of 0.5 at the frequency of 1 kHz. The mean current values are matched with DC electroplating currents to fabricated cantilevers at the same current densities.

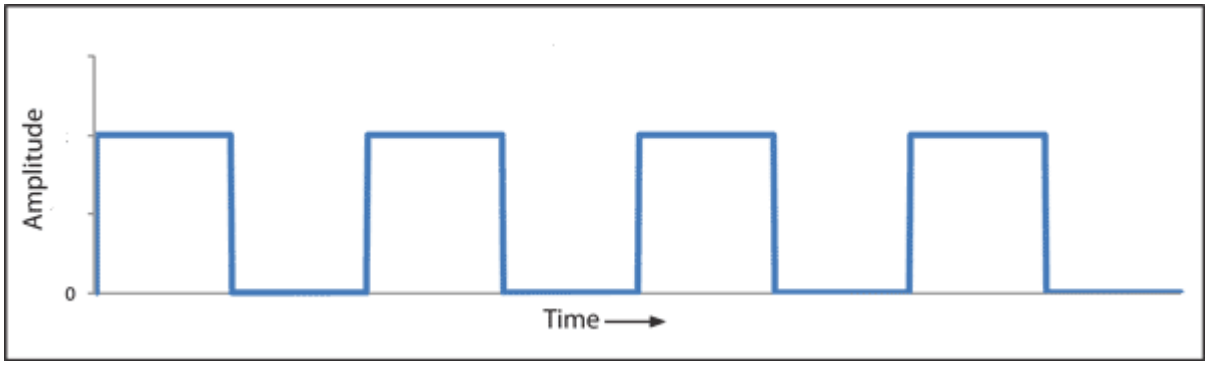

Figure 3.10: Demonstrated positive square wave pattern of current is chosen to perform pulse plating experiments

Unlike DC electroplating, several attempts to fabricate cantilevers at 30 °C and 20 mA/cm^2 are failed with pulse plating. Deposited nickel layers were peeled off from the silicon substrate after the wet release of cantilevers in KOH bath possibly due to higher internal stresses in the deposits. In order to demonstrate cantilever deflection at higher current densities at 30 °C, the current density of 15 mA / cm^2 is chosen to fabricate cantilevers. The same problem also occurred at this current density. Finally, a successful fabrication is performed at 30 °C and 10 mA / cm^2.

Electroplating thickness measurements are carried out using a surface profiler (Veeco, Dektak 8) with a 15 μm/s scan speed. Three electroplating thickness measurements for each cantilever are taken as shown in Figure 3.11 to take into account of the thickness variation along the length of cantilevers. As seen in thickness measurement results in Appendix A1, there is indeed a small amount of change along the length of cantilevers. With this approach, the average value of those three thickness measurements is assigned to each cantilever as its thickness.

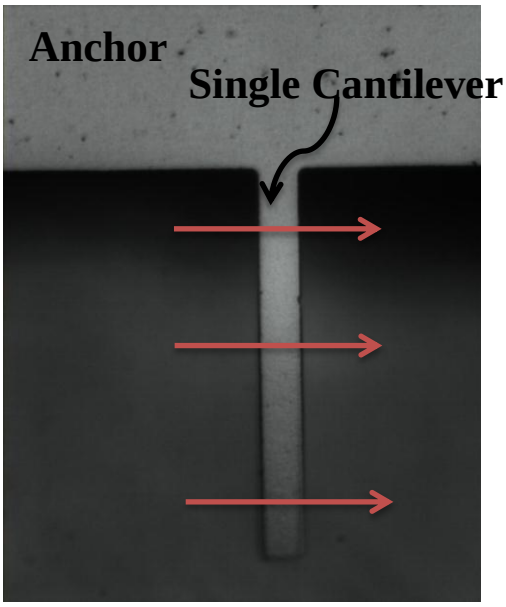

Figure 3.11: Three thickness measurements are carried out along different sections of each microcantilever with a profiler

The electroplated nickel thickness data of those 15 cantilevers are used to draw thickness contour plots of each chip to visualize electroplating thickness distribution for each electroplating case fabricated by either dc or pulse plating. In Figures 3.12-3.14, the representative electroplating thickness variation is illustrated for dc plated chips fabricated with each one of the employed current densities. In the figures, each plus sign indicates actual measurement point and one of the contact points of the chips is taken as a reference origin point to determine x and y coordinates of measured cantilevers. Thus the left bottom and right upper parts of figures are the locations where crocodiles are attached to the samples.

These plots show lines of same electroplated film thicknesses on each sample. These figures imply that even at the lowest applied current density of 1 mA/cm^2, there are still some thickness gradients across each sample. Thickness distributions seem to be symmetrical due to crocodile contacts at two opposite corners. Furthermore this thickness non-uniformity is proportional with increasing current density. Thus it is impossible to assume a single cantilever thickness across each chip. Nickel film thickness values of measured cantilevers need to be noted.

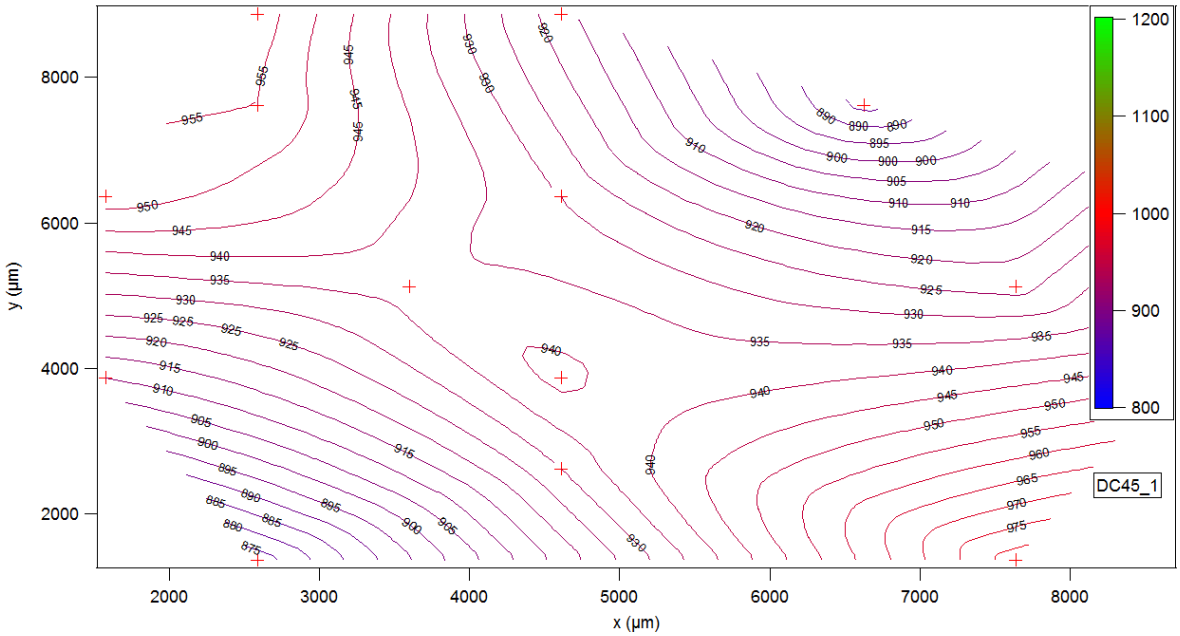

Figure 3.12: Contour plot of the chip fabricated at 45 °C and 1 mA/cm^2 by DC electroplating indicates almost uniform thickness distribution.

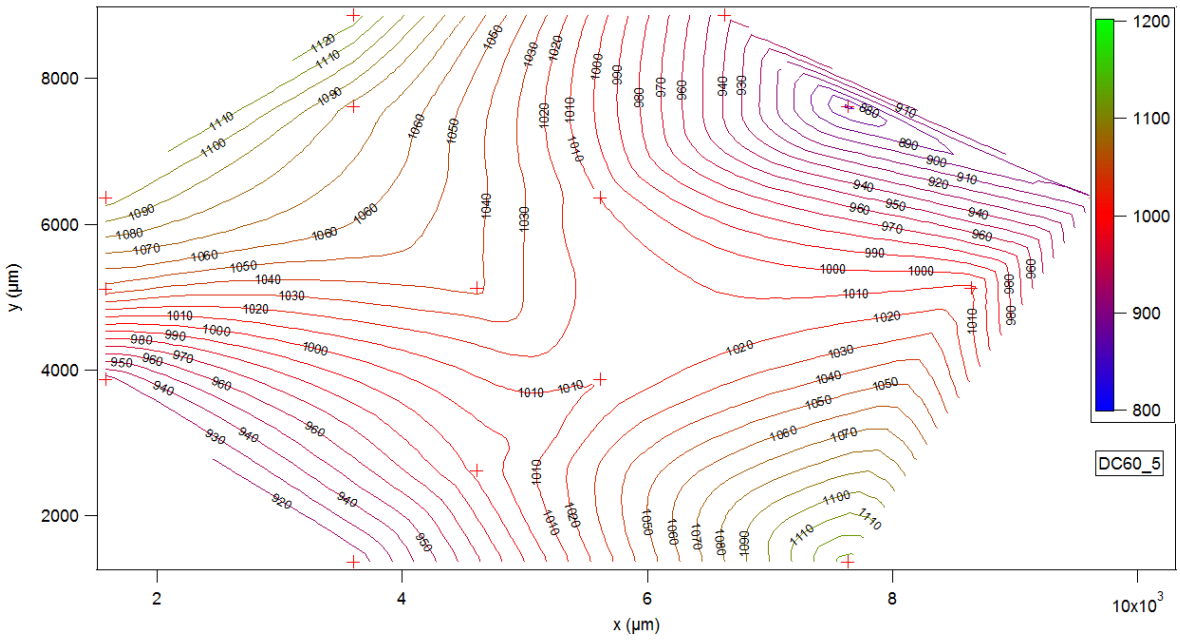

Figure 3.13: Contour plot for the chip fabricated at 60 °C and 5 mA/cm^2 by DC electroplating confirms that as the current density increases, noticeable thickness gradients appear.

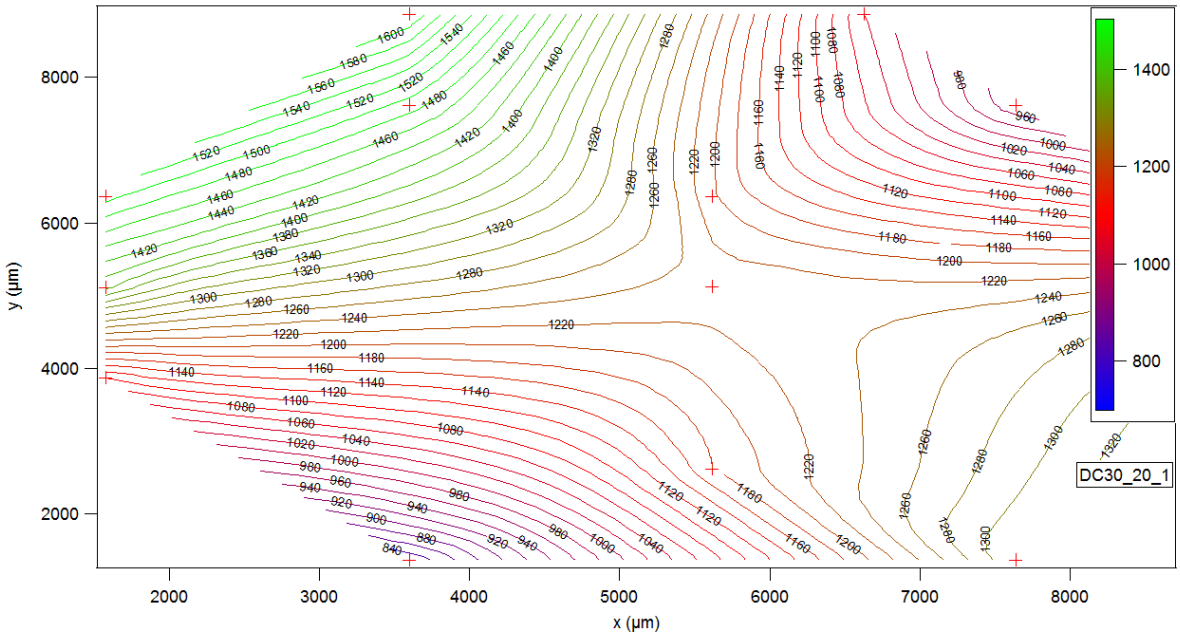

Figure 3.14: 20 mA/cm^2 current density results in excessive thickness non-uniformity. Non-contact corners have considerably higher thicknesses for the case of 20 mA/cm^2 current density

The whole plots corresponding to each electroplating case including chips fabricated either dc or pulse plating can be found in Appendix B1-B2. The Table 3.2 summarizes the mean (µ) thickness and corresponding standard deviation (σ) data of each fabricated chip.

Table 3.2: Increasing current density results in higher deposition rates in exchange of thickness non-uniformity

	DC Plating			Pulse Plating		
Chip	**µ**	**σ**	**%**	**µ**	**σ**	**%**
30_1	968,6	27,6	2,9	1006	37	4
30_5	980,2	89,9	9,2	900	108	12
30_20_1	1231,1	214,5	17,4	960	259	27
30_20_2	1094,6	179,8	16,4			
45_1	931,2	28,6	3,1	1075	20	2
45_5	889,4	102,5	11,5	1005	123	12
45_20	1008,8	135,4	13,4	1072	281	26
60_1	1031,3	33,7	3,3	976	34	4
60_5	1007,0	82,3	8,2	1062	128	12
60_20	1165,1	171,4	14,7	1186	285	24

As seen in the Table 3.2 and Figures 3.12-3.14, there is a noteworthy thickness variation for chips fabricated with 20 mA/cm^2 current density. However, this variation almost diminishes when the 1 mA/cm^2 is employed to fabricate microcantilevers. Contour plots also demonstrate that cantilevers adjacent to contact points have relatively smaller nickel films thicknesses than cantilevers close to free corners of samples. This behavior can be explained with the effect of crocodiles on electroplating. During electroplating, preferential flow of

current directly through crocodiles results in lesser film thicknesses especially on areas close to contact regions than remote areas. However, this effect becomes negligible when current density is decreased to 1 mA/cm^2 as shown in Figure 3.12.

As seen in Table 3.2, two DC electroplated chips are fabricated at 30 °C with 20 mA/cm^2 current density. Since the applied 20 mA/cm^2 current density results in a considerable thickness variation across each chip, it looks reasonable to use both of the samples with different mean nickel thicknesses to investigate to the fabrication case of 20 mA/cm^2 current density and 30 °C solution temperature.

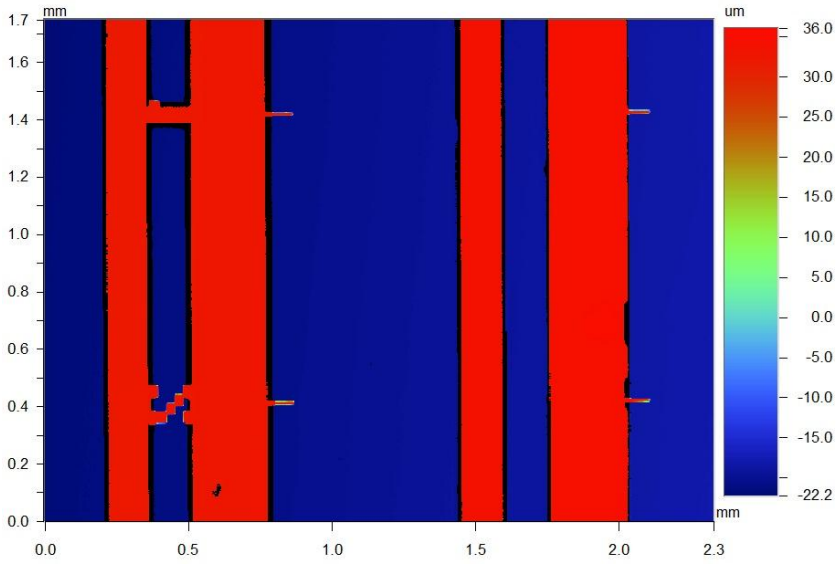

Figure 3.15: There is approximately 50 µm gap between cantilevers and bottom Si substrate surface after the releasing stage

White light interferometry (WLI) measurements are performed with a Brüker model ContourGT 3d optical microscope to visualize 2d and 3d profiles of cantilevers. The WLI picture of some of released cantilevers can be seen in the Figure 3.15. As seen in the figure, approximately 50 – 60 µm silicon etch is required to fully release the designed cantilevers having width of 10 µm with an aspect ratio of 10. The 3d image of the final structure at the end of the fabrication can be seen in the Figure 3.16.

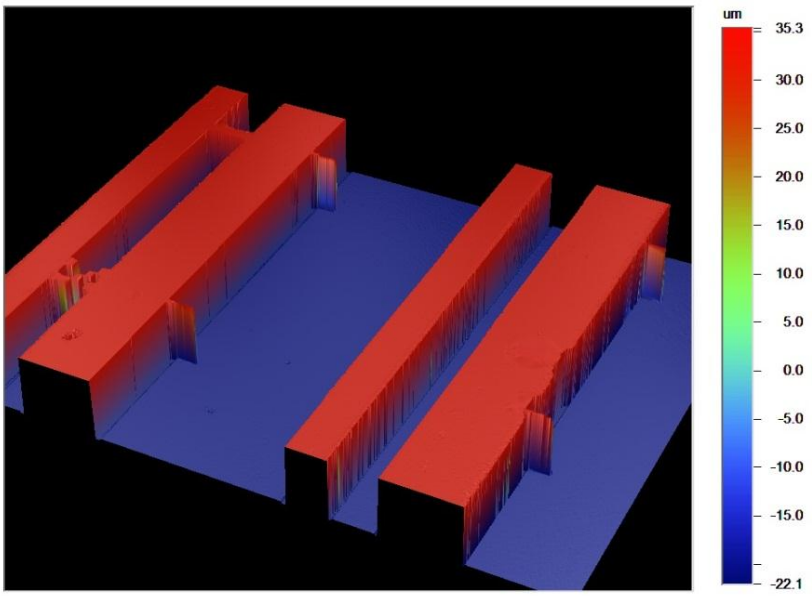

Figure 3.16: The 3d image of released cantilevers together with anchors

3.4 Cantilever Tip Deflection Measurements

Deflections of fabricated single-layer nickel cantilevers are measured by utilizing one of the following techniques: (i) interferometric lens, (ii) optical microscope with a calibrated stage or (iii) WLI techniques.

The interferometric lens (Thorlabs, FD1G model additive dichroic green color filter) is employed to measure deflections of cantilevers relative to anchors by adjusting the x-y stage of a microscope such that nickel anchors become straight. Then the deflection is measured by counting formed fringes between the support and tip of that cantilever. Any distance between two consecutive fringes which corresponds to half wavelength of the employed green light is assumed to be 250 nm. Cantilevers with relatively low deflections are measured with the interferometric microscope. However, it becomes harder to count fringes with bare eyes when deflections of cantilevers are higher than approximately 4 μm. Thus these higher bent cantilevers are measured by utilizing the other employed methods.

Deflections of severely bent cantilevers are measured by utilizing optical microscope (Meiji, VM-1V video microscope) with a calibrated stage (Newport, M-562). A microscope with a 50x lens is used to focus to the tip and support of each cantilever respectively while digital outputs of z coordinate are noted. The difference of z coordinates is calculated to

obtain cantilever deflections. The calibration of the stage is carried out by comparing cantilever deflections readouts of the interferometric microscope and microscope with a calibrated stage. As seen in the measurements results in Appendix C2, the obtained values is converted into deflection values by multiplying with a 0,795 correction factor.

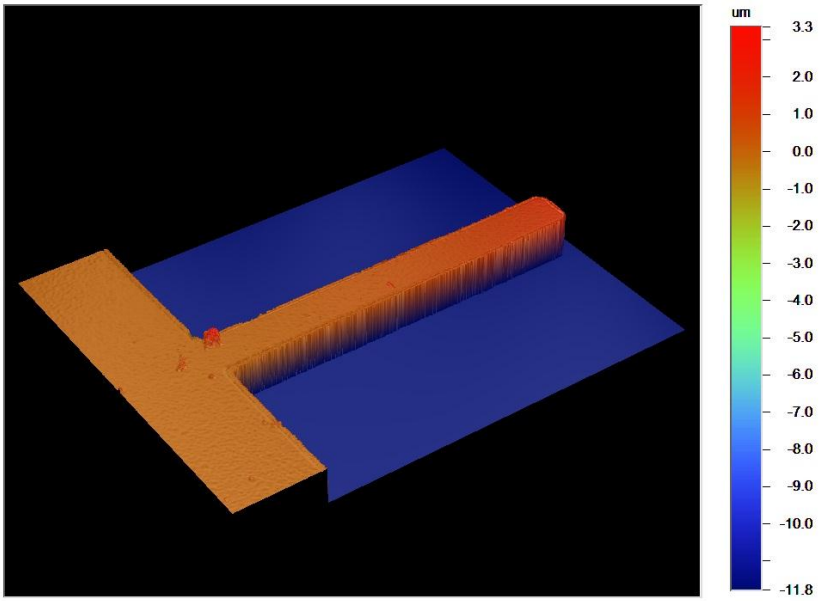

Figure 3.17: Employed fabrication conditions may result in upward cantilever deflections such as this cantilever

WLI provides the highest resolution of deflection among the employed techniques used to measure deflections and also extract 2d and 3d deflection profiles of cantilevers with a nanometer measurement precision. The deflection measurement of highly bent cantilevers becomes more accurate with the WLI technique rather than results obtained by the optical microscope with a calibrated stage.

At the end of fabrication, cantilevers are found to bend either upward or downward depending on the deposition conditions. The 3d image of an upward bent cantilever is shown in Figure 3.17. Moreover, the deflection profile of the same cantilever measured by WLI technique is shown in Figure 3.18.

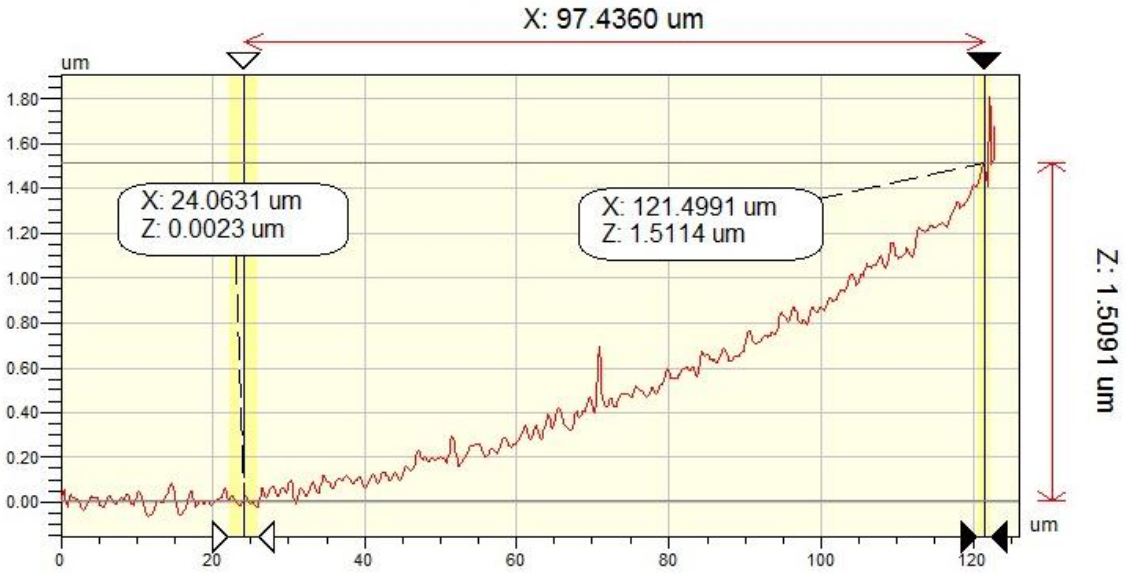

Figure 3.18: This deflection profile of the same cantilever indicates roughly 1,50 µm upward deflection

An example of a downward bent cantilever is illustrated in the Figures 3.19-3.20 with its corresponding 3d image and deflection profile respectively.

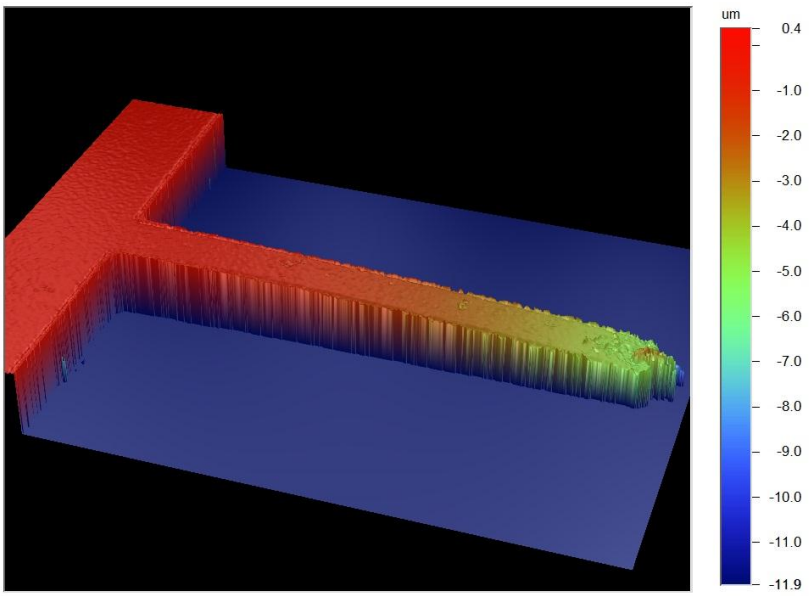

Figure 3.19: A representative 3d image of a downward bent cantilever

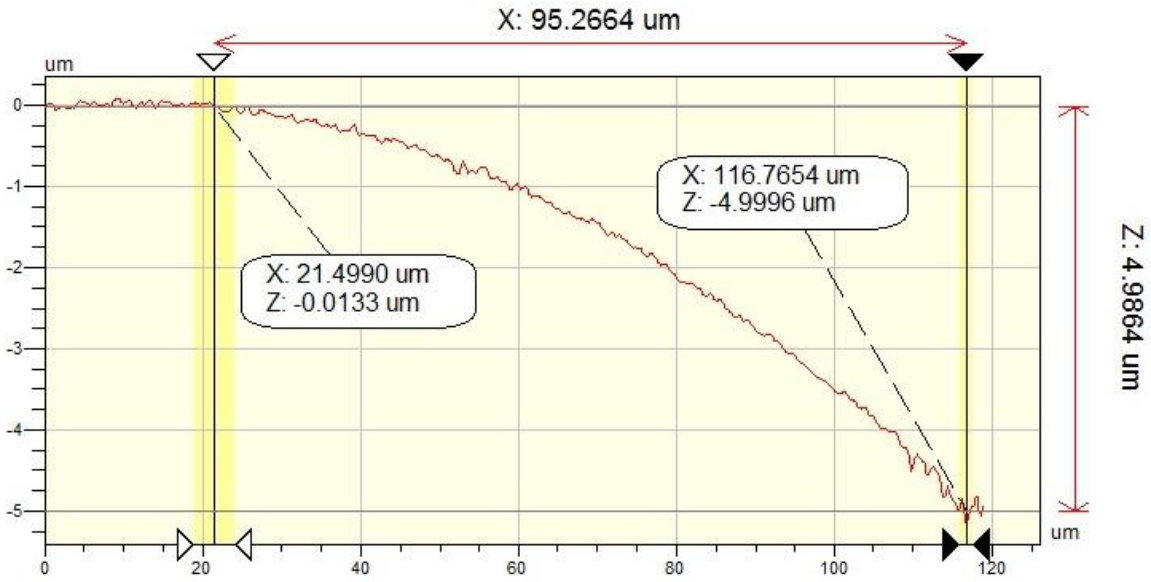

Figure 3.20: Extreme deflections around 5 µm can be obtained by altering deposition conditions

Cantilevers previously used for nickel thicknesses distribution measurements are utilized to perform deflection measurements. More than 12 cantilever deflection measurements are made to reflect the effect of fabrication conditions on the deflection behavior properly. The mean and standard deviation results of measurements for DC and pulse plated cantilevers can be seen in the Table 3.3 and Table 3.4. All of the raw deflection data of cantilevers is presented in Appendix C1 and C2.

Table 3.3: The mean and standard deviation of tip deflections of DC Plated cantilevers

	µ (µm)	σ (µm)	%
30_1	4,53	0,74	16,36
30_5	-0,21	0,84	408,40
30_20_1	-1,80	0,42	23,59
3_20_2	-0,99	0,32	32,48
45_1	4,40	0,39	8,85
45_5	2,65	0,51	19,38
45_20	-2,12	0,75	35,63
60_1	0,83	0,23	27,94
60_5	3,45	0,33	9,57
60_20	2,03	0,51	25,17

Table 3.4: The deflection trends of pulse plated cantilevers follow more or less deflection behavior of DC plated cantilevers

	μ (μm)	σ (μm)	%
30_1	3,17	0,59	18,71
30_5	1,36	0,38	27,64
30_10	0,03	0,81	2581,25
45_1	4,29	1,10	25,71
45_5	2,94	0,48	16,29
45_20	-1,70	0,66	39,09
60_1	0,56	0,24	43,73
60_5	2,70	0,79	29,19
60_20	1,71	0,46	26,79

In the Tables 3.4-3.5, a sign convention is adopted such that positive deflection numbers are downward deflections. Thus deflections of upward bent cantilevers correspond to negative numbers.

DC and pulse electroplating are compared in terms of the internal stress gradient by using cantilevers fabricated under the same fabrication conditions. A comparison of the deflections between DC and pulse plated cantilevers is given in Figure 3.21. Figure 3.21 indicates that the deflection trend of cantilevers as a function of current density fabricated at 60 °C is rather different from those deposited at 45 and 30 °C solution temperatures.

The mean deflection values of pulse plated cantilevers seem to be a bit lower than those fabricated with DC electroplating for most of the cases. However as seen in Table 3.2, there are small mean thickness variations between chips fabricated with DC and pulse plating at the same deposition conditions. As will be seen in Figure 3.25-3.27, deflections are found to change with film thicknesses. So these small deflection differences might be related with those small mean film thickness variations. However, it seems appropriate to state that cantilevers demonstrate much or less similar dependency on the current density, independent on the use of DC or pulse plating.

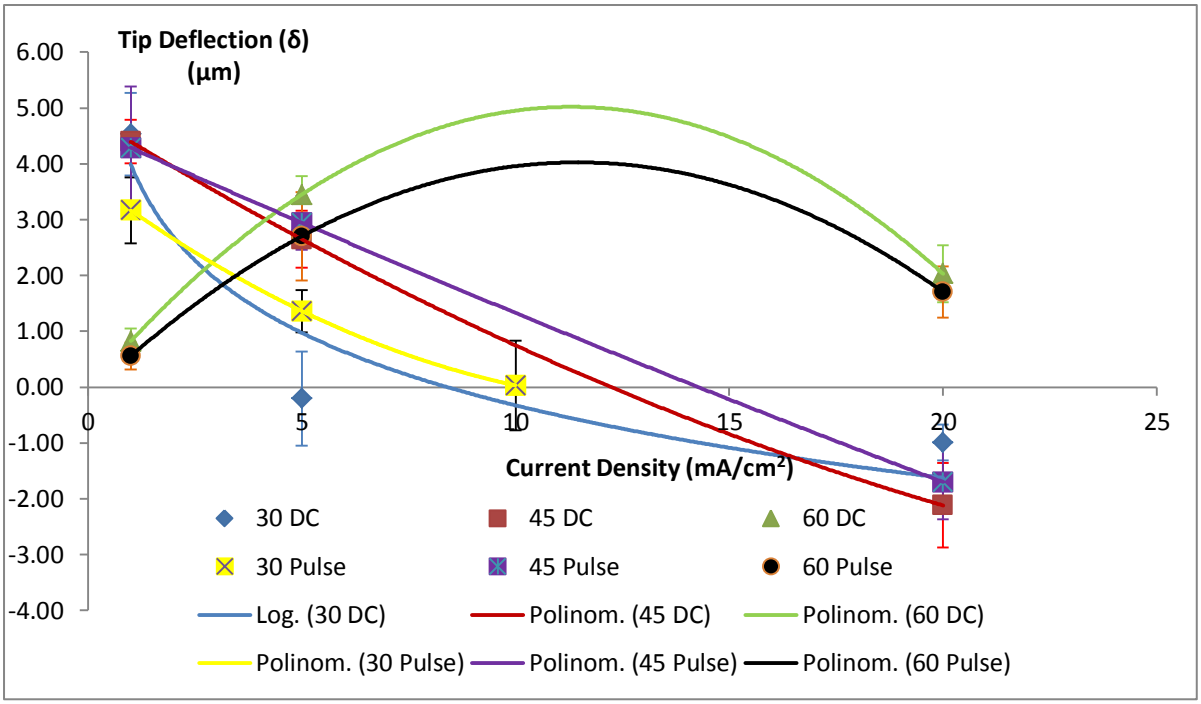

Figure 3.21: There is a zero deflection case at some specific current density for the plating temperatures of 30 and 45 °C for both of the DC and pulse electroplating

Figure 3.21 is divided into Figures 3.22-3.24 to better visualize the current density dependency of deflections of DC and pulse plated cantilevers at a specific temperature.

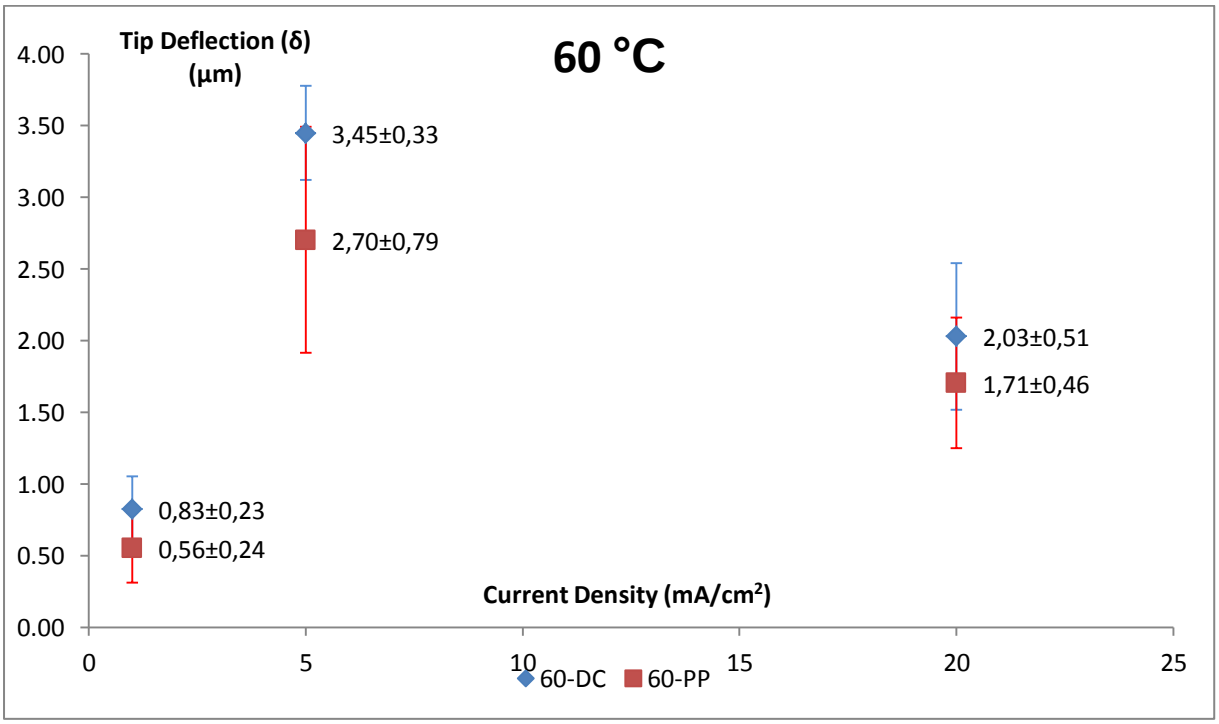

Figure 3.22: Cantilevers fabricated at 60 °C solution temperature seem to have no zero internal stress in the 1 – 20 mA/cm^2 current density range

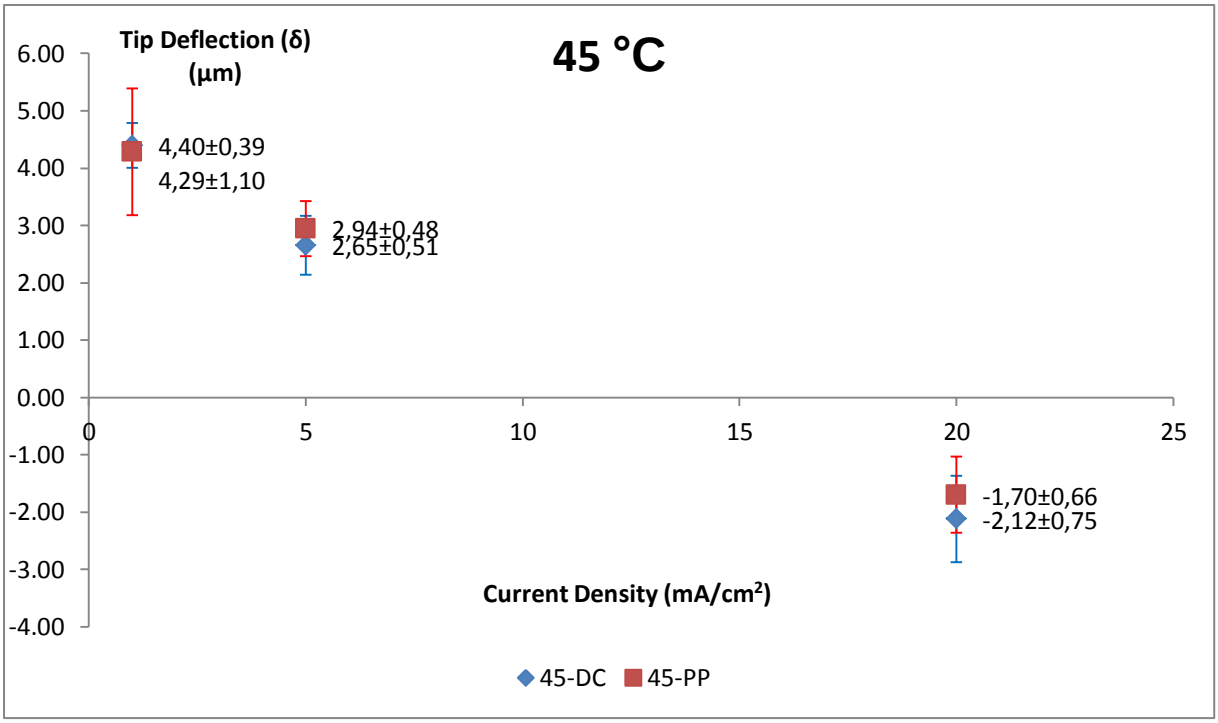

Figure 3.23: As the current density rises, the cantilever deflection turns from downward to upward direction for cantilevers fabricated at 45 °C.

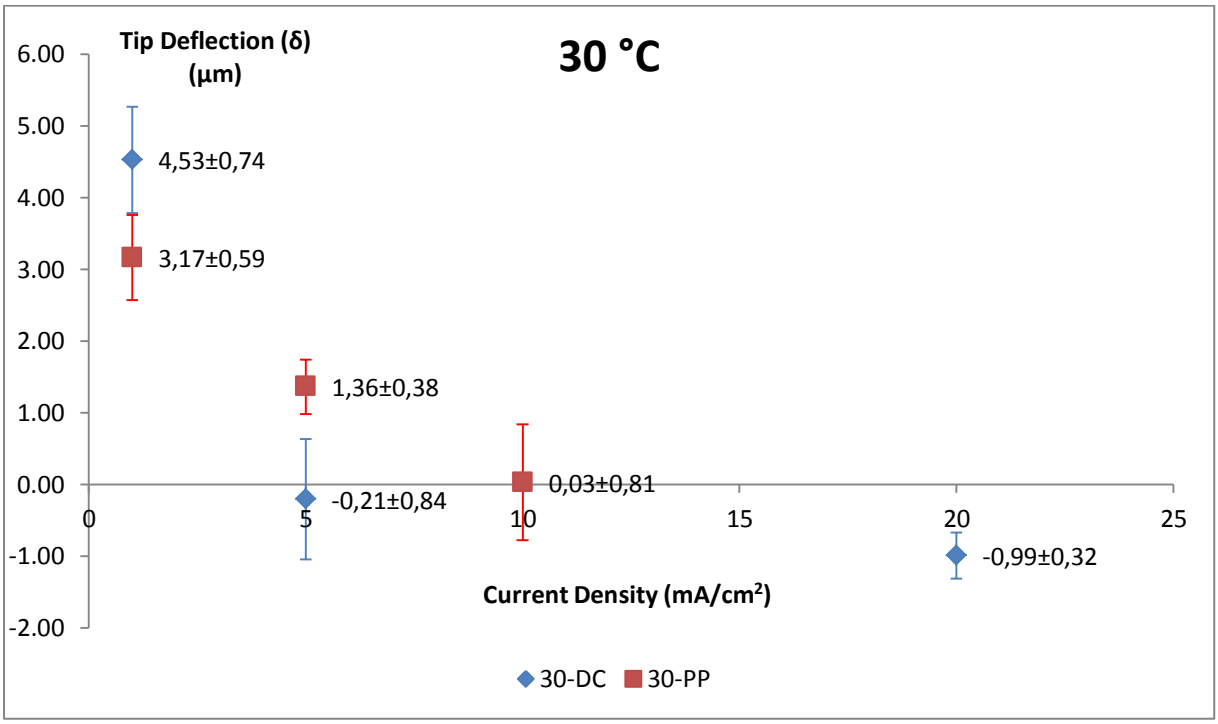

Figure 3.24: Similar deflection-current density behavior exits for both of the 30 and 45 °C electroplating solution temperature cases

In addition to investigating of stress gradients in microcantilevers having a specific thickness, *i.e.* 1 µm, high current density of 20 mA/cm^2 results in considerable thickness variation across fabricated 1 cm x 1cm chips as seen from the standard deviation of the

electroplating data in Table 3.2. These measurements can also be used to observe the relation of cantilever deflection with varying cantilever thicknesses. Since it is stated in the literature that microstructure of thin films may change with film thickness [44], these noteworthy thickness variations may affect the deflection properties of cantilevers. Figures 3.25-3.27 show tip deflection trend of cantilevers, having varying film thicknesses and fabricated with the current density of 20 mA/cm^2.

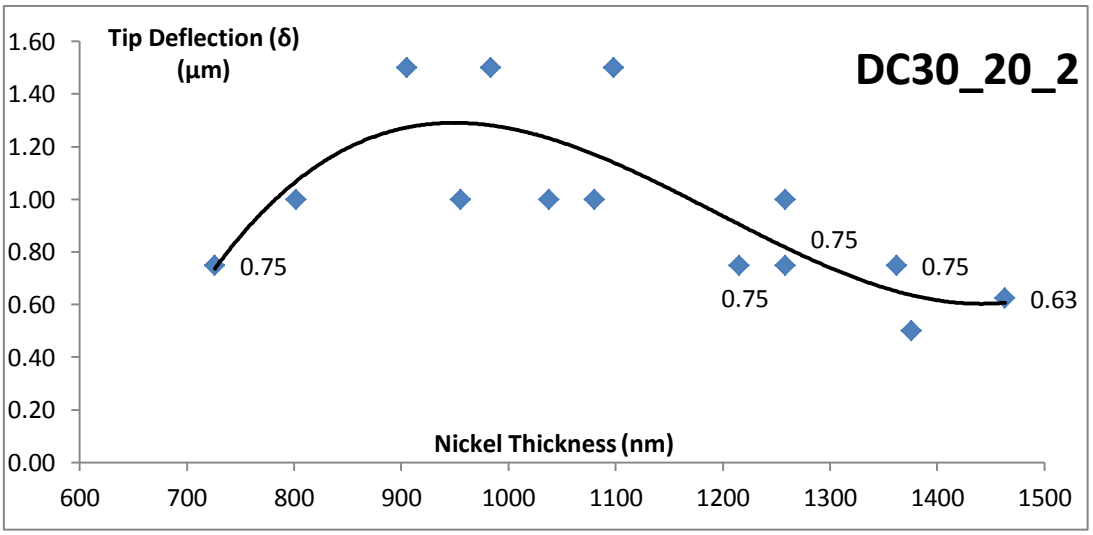

Figure 3.25: Cantilever dip deflections seem to have the highest value around 1000 nm for the chip DC fabricated at 30°C and 20 mA/cm^2.

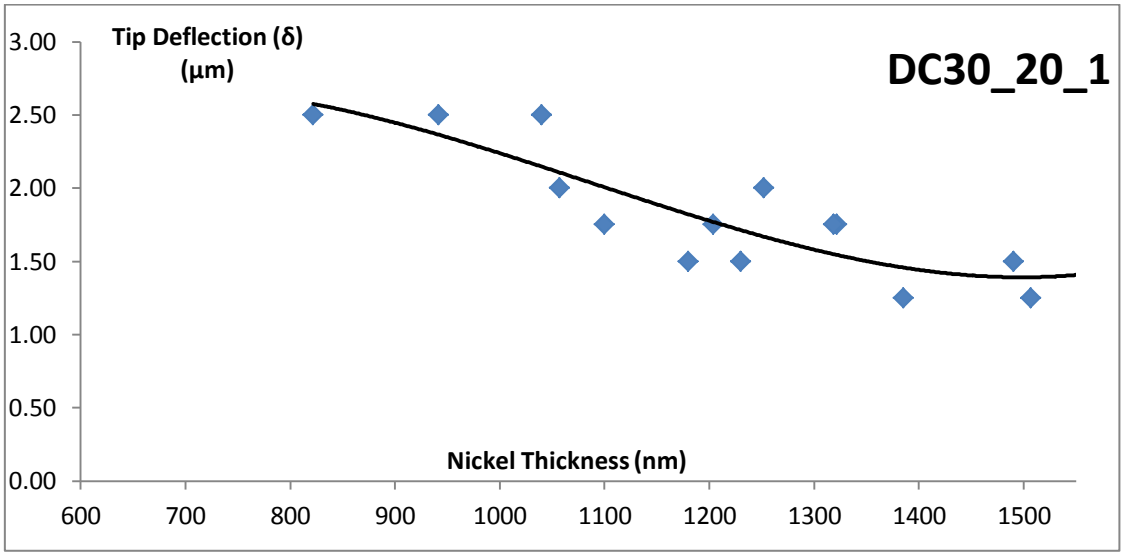

Figure 3.26: Thicker cantilevers have relatively low upward deflection than other cantilevers fabricated at 30 °C and 20 mA/cm^2.

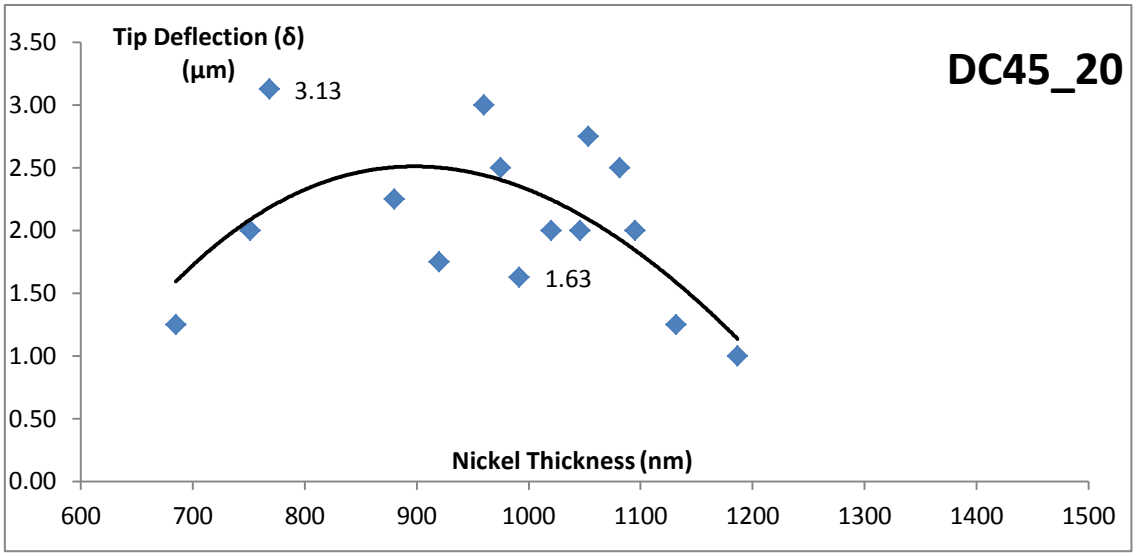

Figure 3.27: A similar behavior is observed for the cantilevers fabricated at 45 °C and 20 mA/cm^2.

As seen in the Figures 3.25-3.27, there is a deflection peak around 1 μm and deflection values seem to decrease while film thicknesses diverge from approximately 1 μm film thickness. Thus it is reasonable to claim that this wide thickness variation increases the standard deviation of cantilever deflection and stress gradient distribution of microcantilevers especially fabricated at 20 mA/cm^2 current density. In other words, these severe film thickness variations can be kept responsible for some part of the standard deviation of deflections of cantilevers fabricated at 20 mA/cm^2 current density shown in Tables 3.3-3.4.

3.5 Modulus of Elasticity Measurements

It is shown in Section 2.4 that the stress gradient of a single layer microcantilever depends also on the modulus of elasticity of the microstructure. Thus the characterization of the stress gradient in a single-layer microcantilever requires the determination of the modulus of elasticity of thin films as a function of process parameters. The modulus of elasticity of thin films is investigated by determining resonance frequencies of microcantilevers in air. Electromagnetic actuation by using an electromagnetic coil and some permanent magnets together with optical readout by using an open-loop LDV setup is utilized to determine resonance frequencies of microcantilevers whose deflection and thickness values are already noted. Various components of the measurement setup are indicated in Figure 3.28.

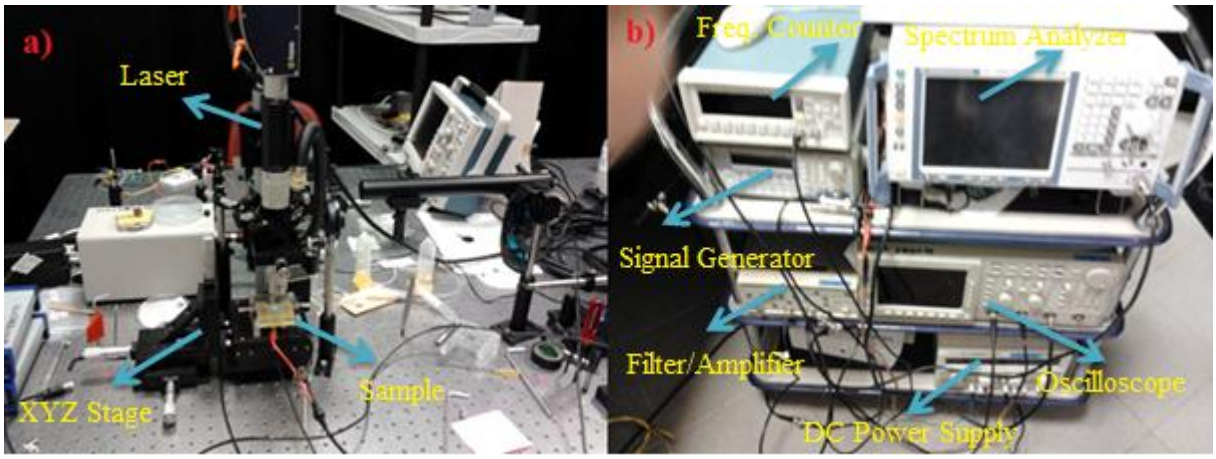

Figure 3.28: The illustration of main components of the frequency measurement setup; (a) sample on a xyz stage and laser source, (b) electronic equipment for optical readout of resonance frequency

The relation of the modulus of elasticity of a single layer microcantilever with its resonance frequency can be derived from the modal analysis of a uniform, homogeneous, rectangular multilayer Bernoulli beam. Such an analysis done by Sandberg, R. [50] leads to the following well-known relation for a single-material homogeneous, rectangular, fixed-free cantilever.

$$f_n = \frac{(\kappa_n L)^2}{4\pi} \frac{h}{L^2} \sqrt{\frac{E}{3\rho}} \tag{3.1}$$

where E, ρ, h and L are the modulus of elasticity and density of nickel; thickness and length of the microcantilever respectively. In the Equation 3.1, the modal parameter is found as $\kappa_1 L = 1{,}8751$ for the first mode. By employing the bulk mass density of nickel as 8908 kg/m^3 and the length of each cantilever as 100 µm, the Equation 3.1 can be reduced to;

$$E = 3{,}4137\ 10^{-11} \frac{f^2}{h^2} \tag{3.2}$$

where the modulus of elasticity (E) in Pa, the resonance frequency (f) in Hz and the thickness of a fabricated cantilever (h) in meters should be used. As seen in the Equation 3.2, the modulus of elasticity of a material is proportional to the square of its resonance frequency for a constant thickness in the case of the fixed-free cantilever.

The modulus of elasticity is also inversely proportional to the square of cantilever film thickness. Due to electroplating thickness variation which is especially emphasized for samples electroplated at the 20 mA/cm^2 current density, particular cantilever thicknesses

measured right after the electroplating step is used to obtain accurate values of the modulus of elasticity of the nickel.

Resonance frequency and, if possible, quality factor data of DC electroplated cantilevers are determined using a specific MATLAB code. More than 12 resonance frequency measurements are carried out for each chip. As seen in Figure 3.29, the mean modulus of elasticity of nickel is found in the range of 128,2 – 175,9 GPa which is smaller than the modulus of elasticity of bulk nickel of approximately 200 GPa. All the modulus of elasticity and quality factor data can be found in Appendix D.

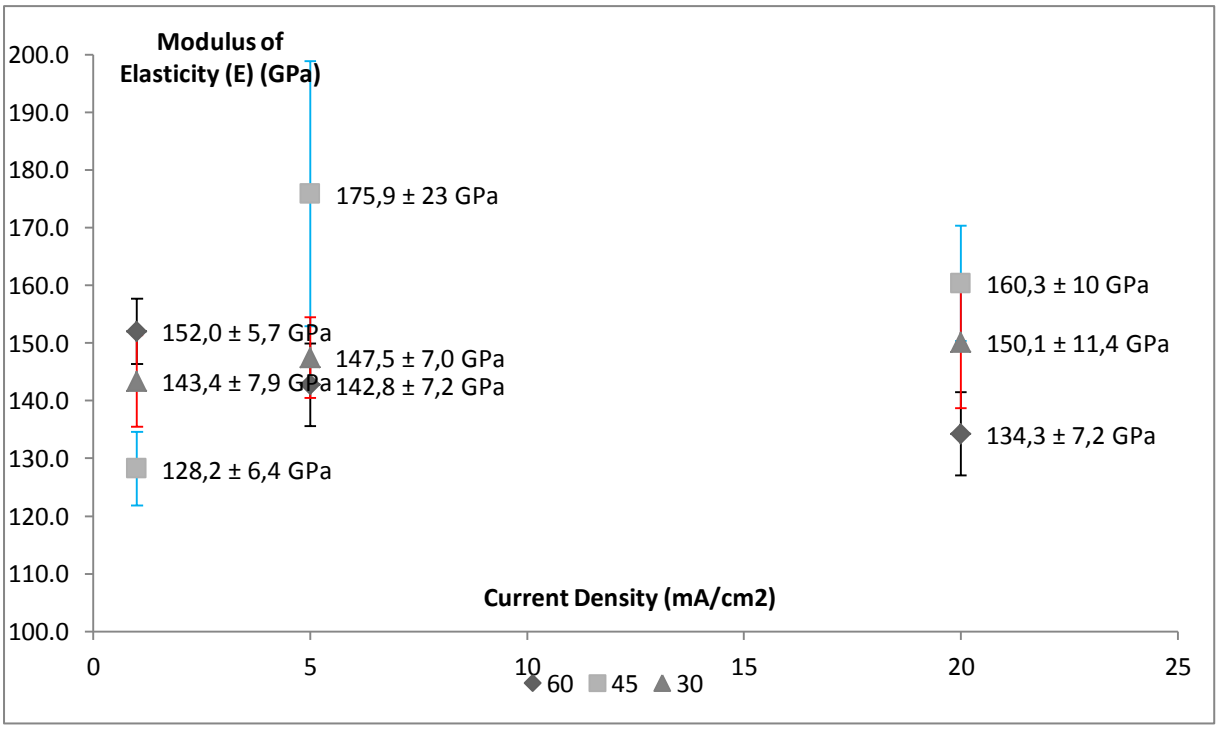

Figure 3.29: The modulus of elasticity measurements of DC plated cantilevers as a function of electroplating bath temperature and employed current density

As seen in the Figure 3.29, there is a relation of the modulus of elasticity with the applied current density for different cases of the electroplating solution temperature. There is an ever-decreasing trend for the modulus of elasticity with the increasing current density at 60 °C. However, the modulus of elasticity of nickel seems to relatively independent from the applied current density in the case of 30 °C nickel solution temperature. Unlike the other two cases, the modulus of elasticity has the highest value at 5 mA/cm^2 current density and 45 °C electroplating solution temperature.

3.6 Stress Gradient Determination of DC-Plated Cantilevers

Since the modulus of elasticity and deflection characterization are performed as a function of the plating parameters for the DC plated cantilevers, it is now possible to relate the stress gradient of single-layer microcantilevers calculated according to Eq. 2.26 with the electroplating parameters. Thus as the prime outcome of this thesis, Figure 3.30 summarizes the residual stress gradient variation with the employed fabrication conditions.

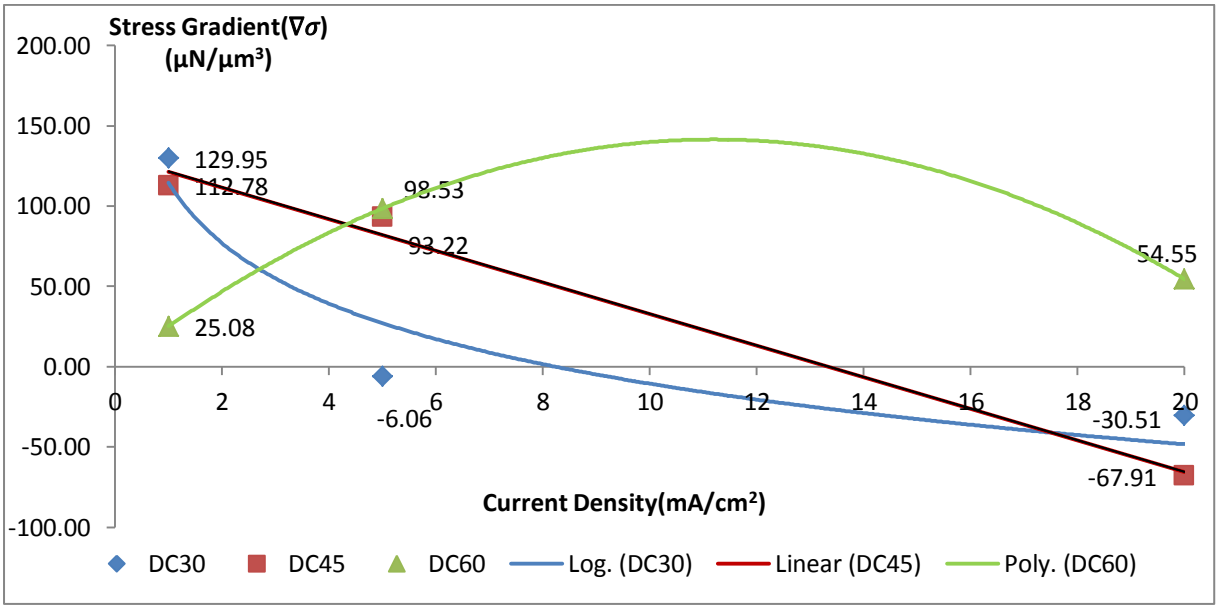

Figure 3.30: The mean stress gradients as a function of the electroplating solution temperature and applied current density.

The negative stress gradient values in the Figure 3.30 come from the notation of the cantilever tip deflection that upward deflections are assumed to be negative numbers. The stress gradients are found to vary in the range of 129.95 to -67.91 µN/µm^3. Figure 3.30 implies that mean stress gradient values decrease monotonously with increasing current densities for the cases of 30 and 45 °C electroplating solution temperatures. However unlike the previous two cases, the mean stress gradient has the highest value at 5 mA/cm^2 current density for the 60 °C solution temperature.

As seen in the Figure 3.30, there is a some specific current density value which results in zero stress gradient, i.e. straight cantilevers, for each of the 30 and 45 °C electroplating solution temperatures. On the other hand, the measurements demonstrate no stress gradient free nickel thin films for the current density range of 1 – 20 mA/cm^2 at the 60 °C electroplating solution temperature.

3.7 Temporal Evolution of Tip Deflection under Room Conditions

The cantilever deflection variation with time is also studied by measuring deflections of the same cantilevers used previously to determine stress gradients. The deflections of previously measured cantilevers are evaluated with an interferometric microscope and white light interferometry (WLI) and compared to previous results.

Four DC plated chips with more than 11 deflection measurements per each chip are employed to investigate temporal effects on cantilever deflections. The deflection measurement raw data can be found in Appendix E.

Table 3.5: The deflection of same cantilevers shifts with time

Chip	M0 (μm)	M1 (μm)	WLI	M1-M0 (μm)
30_5	-0,08±0,81	-0,38±0,89	-0,39±0,96	-0,30
30_20_1	-1,93±0,40	-2,24±0,52	-2,58±0,63	-0,31
30_20_2	-0,99±0,32	-1,23±0,36	-1,35±0,42	-0,24
60_1	0,87±0,17	0,64±0,23	-	-0,23

In Table 3.5, M0 and M1 columns designate the mean deflection measurement results obtained by using an interferometric microscope right after the fabrication in February 2012 and later in July 2012 respectively. The last column in Table 3.5 *i.e.* the difference in mean deflection of cantilevers, points out that cantilevers bend approximately 300 nm to the upward direction with time. The deflection measurement results seen in the table imply that there is a recurring shift in deflection of cantilevers with time among different chips.

The deflection shift of cantilevers may be attributed to the mean temperature variation of the ambient atmosphere, oxidation of nickel cantilevers with time or a stress relief mechanism of electroplated films such as by the elimination of hydrogen trapped in the growing nickel layer during electrodeposition or recrystallization of grains with time.

The Table 3.5 also shows that WLI measurements of the samples give very similar mean deflection values with those taken by using the interferometric lens. These results validate consistency of cantilever tip deflection measurements obtained by the mentioned two techniques.

3.8 Microstructural Analysis of Electroplated Ni Films

The motivation of the microstructural analysis of fabricated nickel films is to understand film characteristics and correlate them with the mechanical properties. The microstructural analysis includes X-ray diffraction (XRD) measurement of nickel films to investigate growing film characteristics and measure average grain size at particular directions and scanning electron microscope (SEM) investigation of surface morphology of fabricated nickel thin films.

Growing film microstructure will be studied by fabricating nickel films at various thicknesses to investigate the film thickness effect on deflections of cantilevers. As seen in Figures 3.25-3.27, there is consistent trend for the cantilever tip deflection with increasing cantilever thicknesses. Cantilevers seem to have highest deflection at approximately 1 μm of electroplating thickness.

Thus, thin nickel films on 1 cm x 1cm silicon substrates with different mean nickel thicknesses are prepared at 1 mA/cm^2 and 45 C. The current density of 1 mA/cm^2 is deliberately chosen to make sure the maximum nickel uniformity across sample surfaces.

The employed fabrication flow and illustration of the microstructure of a fabricated nickel layer with a certain thickness can be seen in respectively Figure 3.31 and Figure 3.32.

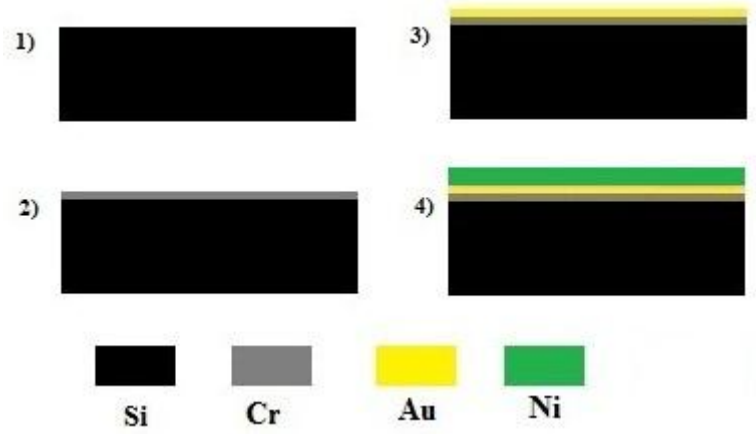

Figure 3.31: The fabrication flow of samples employed to investigate the microstructure of fabricated nickel layers.

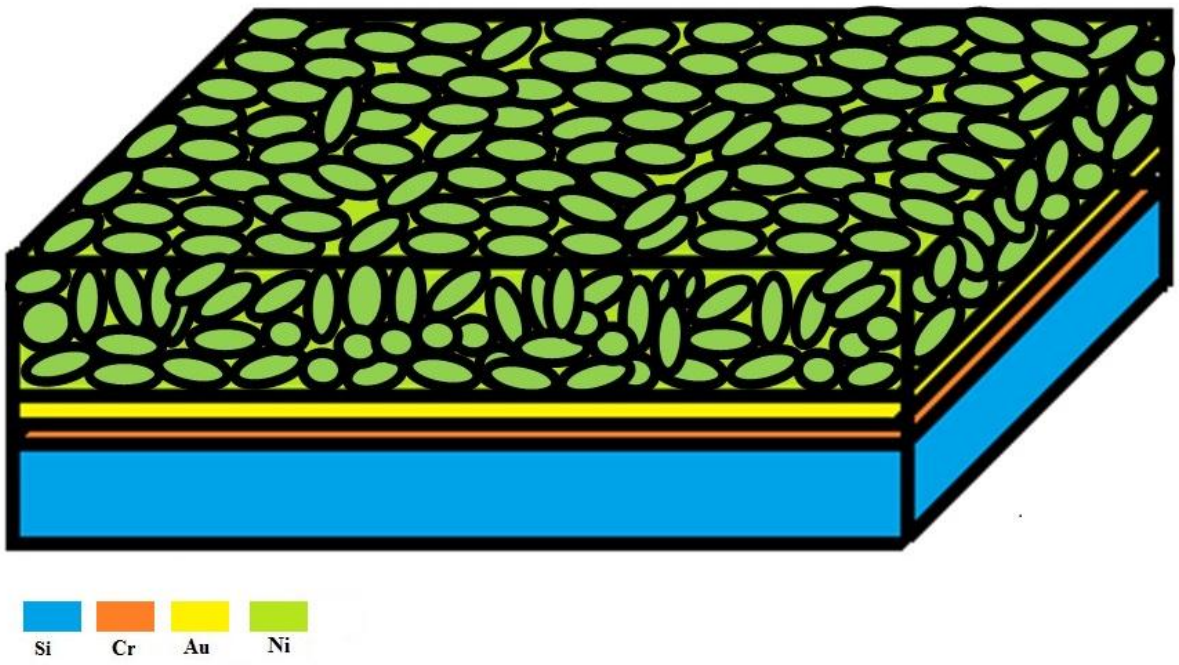

Figure 3.32: The representative microstructure of investigated polycrystalline nickel layer. In addition to in-plane grain orientation variation, the growing nickel layer can show different characteristics due to various factors such as substrate effect.

The preferred orientations of the substrate layers and of the DC electroplated nickel layers having approximately 500, 1000 or 1500 nm thicknesses are investigated by XRD measurements using a Brüker AXS D8 Advance diffractometer. The characteristic peaks of each layer are demonstrated in Figures 3.33-3.34 together with the corresponding Miller indices.

In Figure 3.33, the preferred orientations of the substrate Si and seed Au layer can be seen. The gold layer shows a strong (111) crystalline orientation whereas the substrate Si layer has a (400) preferred orientation. The crystallographic orientations of substrate layers are in consistency with studies in the literature [23].

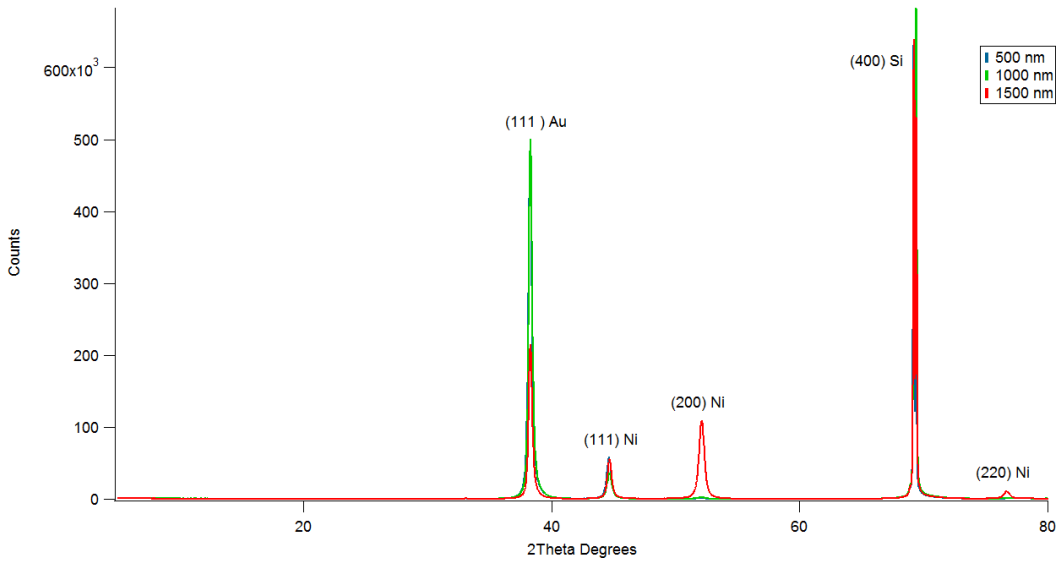

Figure 3.33: XRD scans of DC electroplated nickel samples on silicon substrates with the indicated Miller indices for different nickel film thicknesses

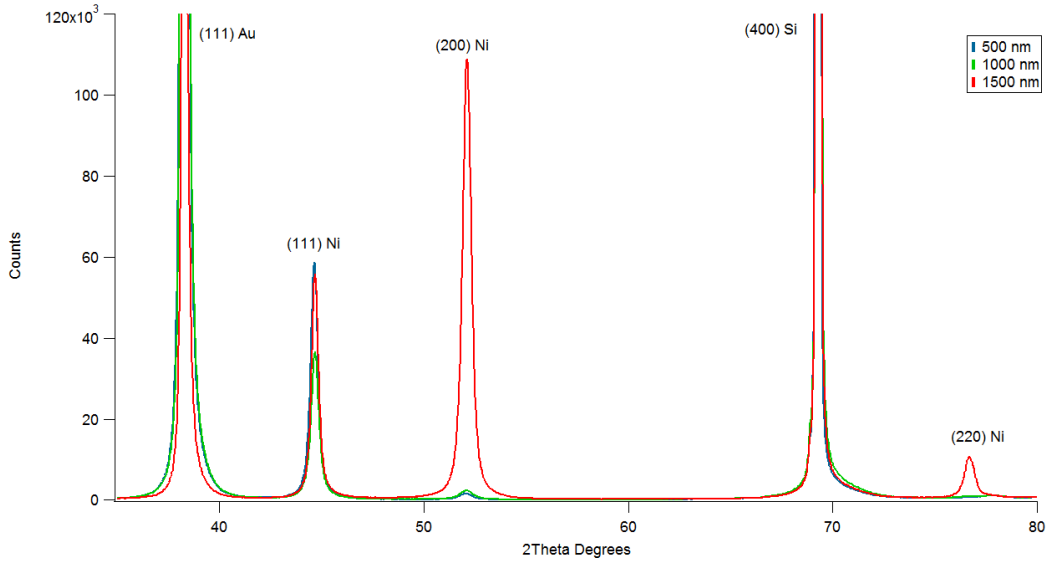

Figure 3.34: This close-up view of the same XRD scan displays the preferred crystallographic directions of electroplated nickel layers having different nickel thicknesses

XRD measurements indicate numerous nickel peaks. Beside of weak, low amplitude peaks of (222) and (311) appeared beyond 90°, the nickel crystallographic orientations of (200), (111) and (220) are mainly emphasized. For the discussion of peak intensities, the peak intensities of nickel should be compared to the values of a polycrystalline high purity nickel. XRD measurements of a nearly isotropic polycrystalline nickel demonstrate the relative peak intensities of 1.00, 0.46 and 0.26 at crystalline orientations of (111), (200) and (220) respectively.

Table 3.6 summarizes peaks intensities of fabricated samples having different nickel thicknesses normalized to the maximum intensity of (111) crystallographic orientation.

Table 3.6: The normalized peak intensities of samples having different nickel layer thicknesses

Ni Thickness (nm)	(111)	(200)	(220)
500	1,00	0,03	0,02
1000	1,00	0,07	0,03
1500	1,00	1,95	0,19

As seen in the Table 3.6, approximately 500 and 1000 nm thick nickel layers have a strong preferred orientation in (111) direction. On the other hand, there is a dominant presence of (200) grain orientation in the case of approximately 1500 nm thick nickel layer.

The XRD measurement data can also be used to compute average grain sizes of different layers at certain directions using the following equation known as the Debye-Scherrer formula in the literature.

$$t = \frac{K\lambda}{B\cos\theta_B} \tag{3.3}$$

where K is a dimensionless constant in the range of 0.89 to 1.39 depending on the specific geometry, λ is the wavelength of the incident beam. B and θ_B terms, as shown in the Figure 3.35, correspond to the full width at half maximum intensity and the half of the degree where the maximum intensity appears respectively.

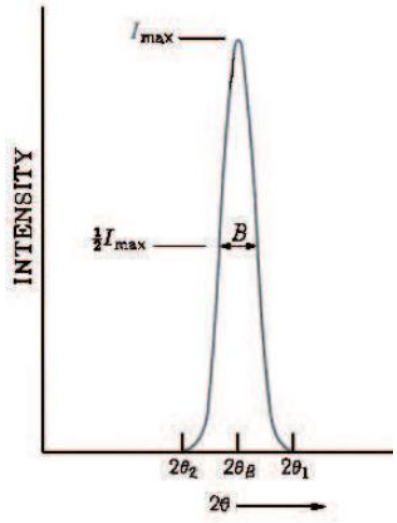

Figure 3.35: The full width at half maximum intensity, i.e. B, for a crystal

By employing 0,94 for *K* as proposed in the literature for describing 3d cubic crystals and 0,154060 nm for the wavelength of the beam, the average grain size of nickel layers having different nickel thickness calculated at preferred orientations is summarized in the Table 3.7.

Table 3.7: The calculated average grain sizes at preferred orientations for the fabricated samples

Nickel Thickness (nm)	(111)	(200)	(220)
500	21,17 nm	12,33 nm	3,96 nm
1000	20,09 nm	11,52 nm	3,28 nm
1500	22,26 nm	18,23 nm	17,00 nm

The microstructural analysis is supported by taking scanning electron micrographs of top nickel surface and cross sections of prepared samples. The micrographs of the top nickel surface of the prepared three samples can be seen in the Figures 3.36-3.38. These micrographs show the surface morphology of the fabricated nickel films of various thicknesses. Compatible with the grain size predictions by XRD measurements of samples, each sample has a similar grain size of around 20 nm comprehended by comparing dimensions of grains of each sample with the scale bar on the micrograph.

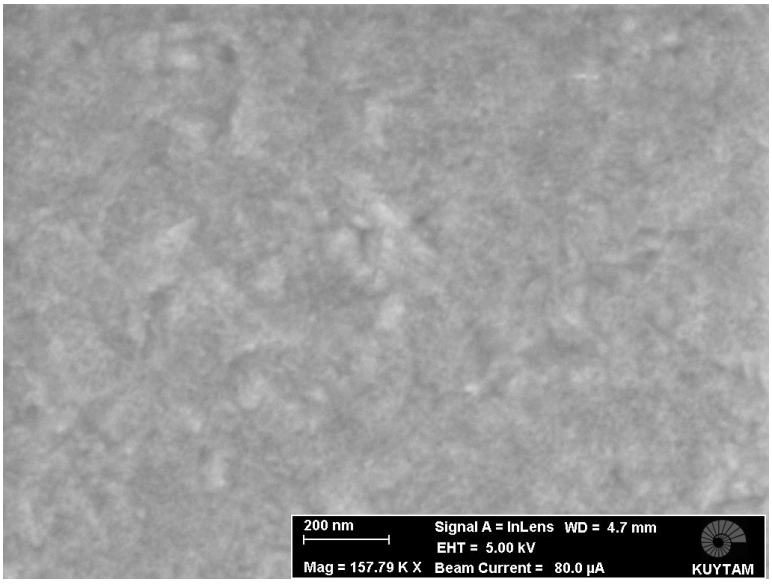

Figure 3.36: The surface morphology of the 1500 nm thick nickel layer

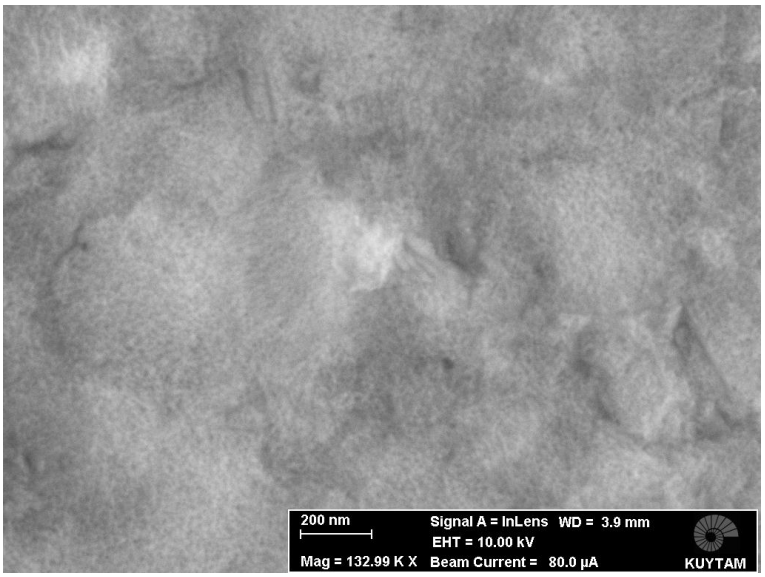

Figure 3.37: The SEM photo taken from the sample with a 1000 nickel thickness

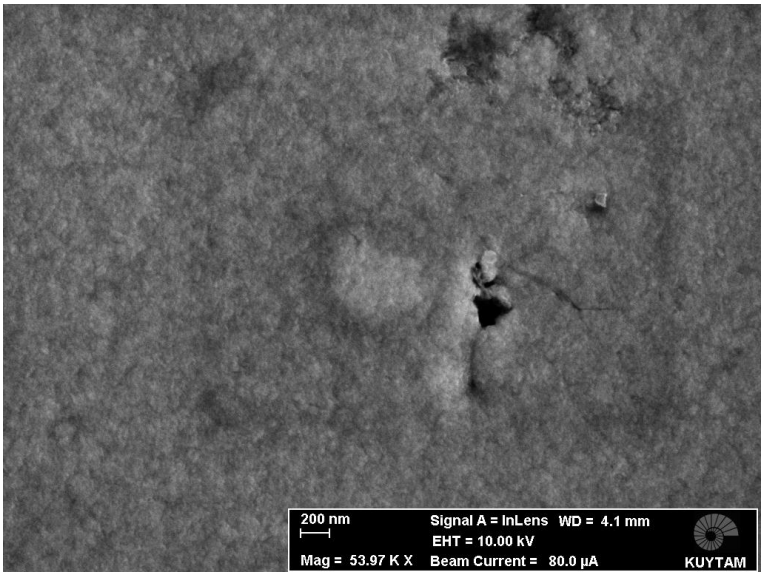

Figure 3.38: This microstructure of 500 nm thick nickel layer seems to have similar grain size with the other two samples

The structural analysis of fabricated nickel layers is finalized by investigating nickel layer growth characteristics by taking SEM pictures from cross sections of samples. However unlike silicon, it is impossible to cut prepared nickel samples into two pieces by simply using a diamond pen due to the ductile fracture nature of nickel. Nickel layers together with the gold seed layer underneath are delaminated from silicon substrates during cutting of samples. Thus it is impossible to obtain SEM samples of cross sections of nickel layers through employment of a diamond pen.

Thus, the following well-known metallographic method is chosen to overcome this problem and prepare samples for the SEM microstructural analysis.

Samples prepared with a similar fashion to XRD samples are fabricated for this analysis. Then those specimens are encased with an epoxy material in an epoxy bath to limit the delamination problem occurred during the cutting process. Then new epoxy-sample composite structures are cut into two pieces with a diamond saw operating at a minimum cutting speed to protect microstructure of nickel layers as much as possible.

The cutting process is followed by the coarse and fine polishing of cross sections of samples by using a metallographic polishing machine with several polishing abrasive discs and diamond suspensions respectively. The polishing stage of the prepared samples takes several hours.

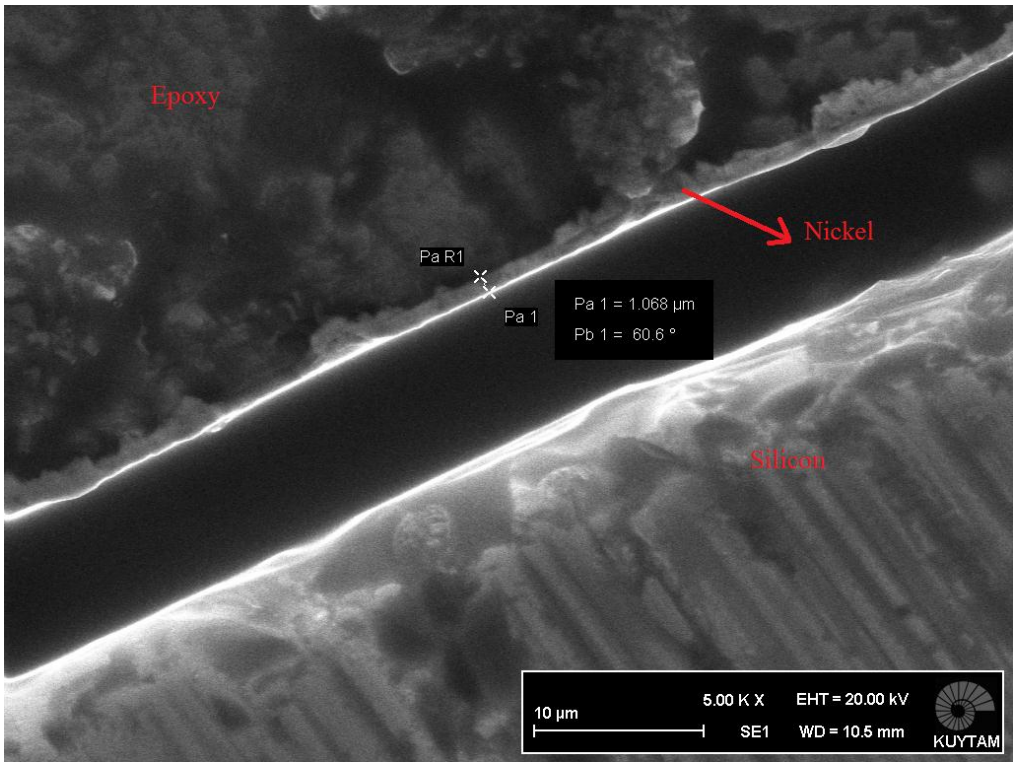

Figure 3.39: Polished nickel cross section peeled off from the substrate silicon during the polishing process and contaminated with epoxy particles

As seen in Figure 3.39, cross sections of prepared nickel samples are damaged and contaminated with epoxy particles during the polishing step, thus SEM microstructural analysis of cross section of nickel layers is failed due to improper samples.

Then instead of cutting nickel films and polishing of cross sections of samples, side surfaces of the fabricated nickel films are examined by tilting the samples and investigating

microstructures of the samples at sample sides in SEM. With this method, the following SEM pictures of Figures 3.40-3.42 are taken. However in this case, side surfaces instead of cross sections are analyzed.

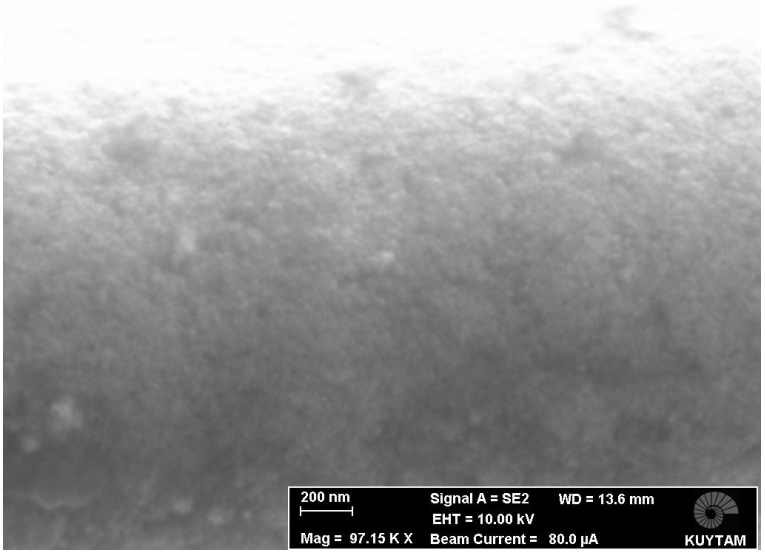

Figure 3.40: The side view photo of the nickel film having approximately 1500 nm mean thickness indicates very smooth surface

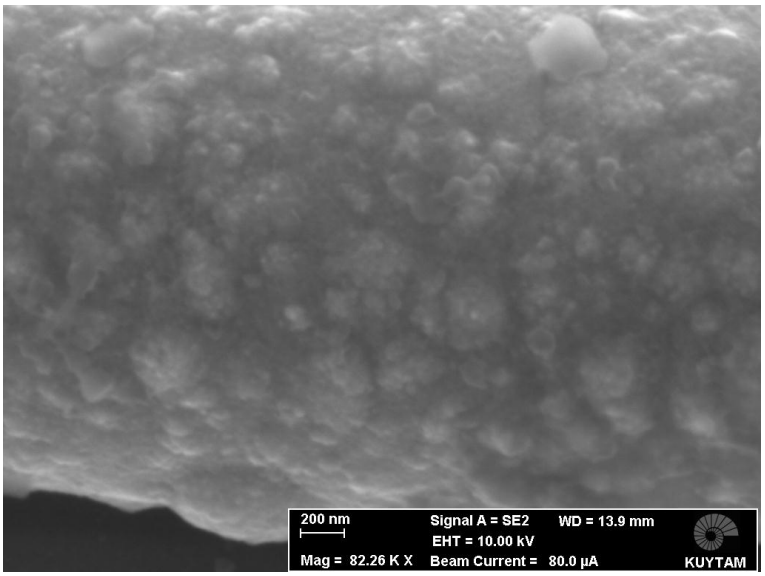

Figure 3.41: The cross section of the 1000 nm approximately thick nickel film

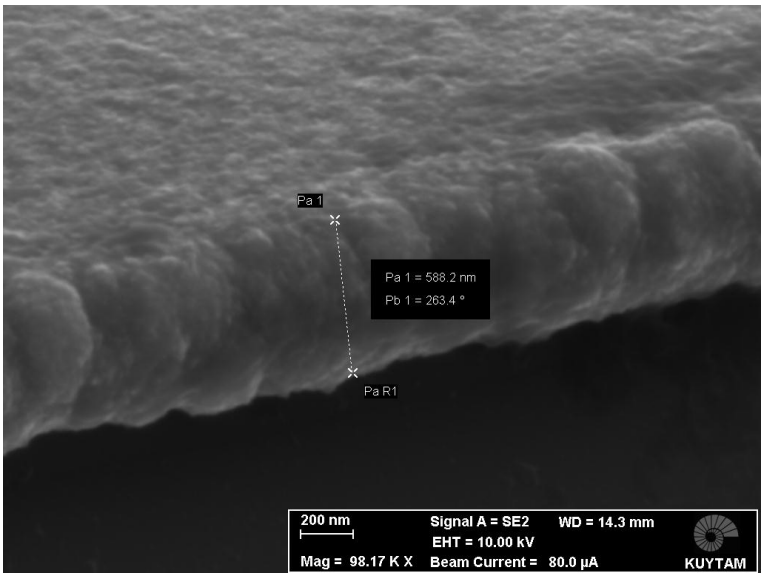

Figure 3.42: The grains of the approximately 500 nm thick nickel layer show a granular structure along the cross section of the layer just like the other two samples.

The Figures 3.40-3.42 indicate that grains have a granular structure throughout the thickness of each one of the electroplated films.

Chapter 4: Conclusions & Future Work

In this thesis, residual stress gradient characterization in electroplated thin films having 1 μm nickel thickness is accomplished by investigating the effect of electroplating parameters of current density and temperature using microcantilevers. The fabrication flow, mainly consisting of the steps of RF sputtering, single-mask photolithography, electroplating and release of fabricated microstructures by wet bulk micromachining, is utilized to fabricate microcantilevers.

The processes involved in previous fabrication flows are enhanced in many ways to increase productivity and repeatability of fabricated microstructures. Positive photoresist (PR) of AZ1514H rather than the previously used negative PR of AZ5214 is employed to enhance the lithographic resolution of microstructures and increase yield of successfully developed microstructures. Together with the new PR, the soft bake parameters are modified from at 110 °C for 10 minutes to at 100 °C for 2 minutes to attain shorter development time together with easier removal of photoresist from wafer surface.

The integration of the scriber machine into the fabrication flow enables the increase of cutting efficiency with a constant specific force and depth and cutting at desired precise intervals.

The pH of electroplating solution is adjusted from the non-additive pH level of 5.4 to 4.0 by the addition of sulfamic acid to eliminate nickel oxide formation, especially realized at higher pH levels of electroplating bath, for most of the chosen deposition conditions. Thus less contaminated electroplating layers are fabricated with continuous stirring during electroplating. Moreover, the characterization experiments are carried out by paying attention to electroplated areas on employed crocodiles to calculate applied current density accurately.

Released cantilevers are immersed in water, acetone and IPA subsequently for at least 5 minutes and dried at room temperature on a flat surface to prevent stiction of microcantilevers as much as possible. At the end of the fabrication flow, single layer cantilevers are fabricated by eliminating gold seed layer underneath.

From the point of view of device design and fabrication, determination of residual stresses in thin films is necessary to optimize device performance and to lower fabrication

costs. Initial in-plane and out-of-plane displacements of a thin film, designed as a moving part in a MEMS application, must be particularly controlled to ensure the performance and life-time of fabricated products.

In addition to well-studied uniform residual stresses in nickel thin films that control in-plane displacements, stress gradients that determine out-of-plane deflections of components need to be characterized to obtain straight microstructures. Thus during preliminary design stage, more realistic estimation of behaviors of an component containing electroplated nickel microcantilevers would be made with the knowledge of residual stress gradient by accounting for initial out-of-plane deflection of microcantilevers.

The residual stress gradient characterization of 1-μm-thick nickel films are performed systematically by varying the electroplating parameters of applied current density and solution temperature in the range of 1 – 20 mA/cm^2 and 30 – 60 °C respectively. In accordance with the derived formulation, cantilever deflection and modulus of elasticity measurements are made for each electroplating case to determine the residual stress gradient of electroplated nickel film from monolayer cantilevers.

Electroplating of cantilevers is performed by either DC or pulse electroplating. In pulse electroplating, a square wave pattern is employed with a duty cycle of 0.5 at the frequency of 1 kHz. The mean deflection values of pulse plated cantilevers seem to be a bit lower than those fabricated with DC electroplating for most of the cases studied. However, pulse plated cantilevers might undergo less deflection if the pulse plating is optimized by studying the effects pulse plating parameters, such as duty cycle, frequency and integration of the positive current to applied wave pattern, on resultant residual stress. Nevertheless, cantilever deflections demonstrate much or less similar dependency on the current density, independent on the type of plating.

Electroplating thickness measurement data are used to draw a thickness contour plot of each sample to visualize electroplating thickness distribution for each electroplating case fabricated by either dc or pulse plating. Considerable electroplating thickness variation for samples fabricated with 20 mA/cm^2 current density is almost diminished when the current density of 1 mA/cm^2 is employed to fabricate microcantilevers.

Cantilever deflection measurements are carried out by using various methods including interferometric lens, microscope with a calibrated stage and WLI. Cantilevers, bent

either downward or upward, are fabricated. The 3D deflection profiles of microcantilevers are also obtained.

Modulus of elasticity of DC-electroplated thin nickel films is investigated by determining resonance frequencies of microcantilevers in air. Electromagnetic actuation by using an electromagnetic coil and some permanent magnets together with an optical readout by using an open-loop LDV setup is utilized to determine resonance frequencies of microcantilevers. The modulus of elasticity of nickel is found in the range of 128,2 – 175,9 GPa which is smaller than the modulus of elasticity of bulk nickel of approximately 200 GPa.

Finally as the prime outcome of this thesis, the stress gradient of DC-plated cantilevers is found to vary from 129.95 to -67.91 MPa/μm. The zero residual stress gradient, *i.e.* straight cantilever, is achieved for each of the 30 and 45 °C electroplating temperatures in the current density range of 1 – 20 mA/cm^2. On the other hand, the measurements demonstrate no stress-gradient-free nickel thin films in the current density range of 1 – 20 mA/cm^2 at the 60 °C electroplating temperature.

Since the applied high current density of 20 mA/cm^2 results in considerable thickness variation across fabricated 1 cm x 1 cm chips as seen from the standard deviation of the electroplating data, cantilever deflections are investigated with varying cantilever thicknesses. There is a deflection peak around 1 μm and deflection values seem to decrease while film thicknesses diverge from approximately 1 μm film thickness.

Temporal evolution of tip deflection of cantilevers under room conditions is also studied. The interferometric lens measurements right after the fabrication in February 2012 and later in July 2012 of the same cantilevers point out that cantilevers bend approximately 300 nm to the upwards with time.

The microstructural analysis includes XRD measurement of nickel films to investigate film characteristics and to measure average grain size at particular directions and SEM investigation of surface morphology of fabricated nickel thin films.

Film microstructure is studied by fabricating nickel films having thicknesses of approximately 500, 1000 and 1500 nm. XRD measurements of fabricated nickel films demonstrate the nickel crystallographic orientations of (200), (111) and (220). Approximately 500 and 1000 nm thick nickel layers have a strong preferred orientation in (111) direction. On the other hand, there is a strong presence of (200) grain orientation in the case of

approximately 1500-nm-thick nickel layer. The preferred crystallographic orientation of (111) for the samples having approximately 500 and 1000 nm thick nickel film thicknesses might be explained as a substrate effect. Because the same XRD measurements show (111) crystalline orientation for the RF-sputtered gold seed layer. However, while thickness of nickel film increases, the (200) crystallographic orientation becomes the dominant grain orientation. XRD measurements also demonstrate approximately 20 nm grain size at preferred crystallographic orientations.

The microstructural analysis is supported by taking scanning electron micrographs of top nickel surface and cross sections of prepared samples. SEM sample preparation for microstructural analysis of cross section of nickel layers by cutting samples with a diamond pen or a diamond saw is failed. However, side surfaces of the fabricated nickel films are examined by tilting the samples. Then microstructures of the samples are investigated at sample sides in SEM. SEM pictures indicate that grains have a granular structure throughout the thickness of each one of the electroplated films.

Understanding of microstructural changes of nickel films, fabricated at certain combinations of current density and temperature that lead to extreme residual stress gradient values, is left as a future work. Nickel films will be electroplated on Au RF-sputtered silicon samples whose half surface is coated with a photoresist layer. In order to eliminate nickel thickness variation on samples which is emphasized at higher current densities, the current density of 1 mA/cm^2 will be used to deposit 500, 1000 and 1500-nm-thick nickel layers at each chosen fabrication condition that results in extreme residual stress gradient. Texture analyses of fabricated samples will be performed to determine preferred crystallographic orientations and average grain sizes at those directions. Then morphologies of cross sections of fabricated films will be investigated by removing spin-coated photoresist layer and studying previous interface of nickel film – photoresist layer in SEM.

This study primarily serves as a basis for further investigations such as the reduction of residual stresses by employing pulse plating or additives, or residual stress modeling of multilayered structures including nickel layers.

Appendix

A0: Fabrication Flow

Step #	Description	Equipment	Parameters	Target
0	**WAFER PREPARATION**			
0.1	RCA1		H_2O_2:NH_4OH:H_2O (3:2:10)	10 min 80 °C
0.2	Diluted HF		HF:H_2O (5:100)	40 s
1	**RF SPUTTERING**			
1.1	Cr Deposition	Vaksis PVD-Handy/2S		20 μm
1.2	Au Deposition	Vaksis PVD-Handy/2S		100 μm
2	**PHOTOLITHOGRAPHY**			
2.1	PR Coating	SPS Spin 150	Program #1 AZ5214	1.3-1.6 μm
2.2	PR Bake	EchoTherm Digital Hotplate		2 min 100 °C
2.3	PR Expose	Rein Raum Technik Lanz MA 45	22 mW/cm^2	17.5 s
2.4	PR Development		AZ351B:H_2O (1:4)	
2.5	Inspection	Veeco Dektak 8	PR Thickness	
2.6	Scribing	OEG MR200		
3	**NI ELECTROPLATING**			
3.1	Ni Electroplating	EchoTherm Digital Hotplate	Nickel Sulfamate Solution	1 μm
3.2	Inspection	Veeco Dektak 8	Ni Thickness	
3.3	PR Stripping		AZ100 Remover	5 min
4	**WET RELEASE**			
4.1	Au Wet Removal		Transene Inc. GE-8148:H_2O (1:3)	2,5 min
4.2	Cr Wet Removal		Microchrome Inc. CEP-200:H_2O (1:3)	40 s
4.3	Si Wet Removal	EchoTherm Digital Hotplate	KOH:H_2O (4:5)	60 °C 50-60 μm
4.4	Cr Wet Removal #2		Microchrome Inc. CEP-200:H_2O (1:3)	80 s
4.5	Rinsing #1		Water	5 min
4.6	Rinsing #2		Acetone	5 min
4.7	Rinsing #3		IPA	5 min
4.8	Drying in Air			

A1: DC Electroplated Nickel Thickness Data

	30-1			Avg	30-5			Avg	30-20-1			Avg	30-20-2			Avg	45-1			Avg	45-5			Avg	45-20			Avg	60-1			Avg	60-5			Avg	60-20			Avg	
A2	935	930	935	933																	725	720	710	718	1250	1235	1225	1237	1000	980	950	977					1360	1360	1360	1360	A2
A3					1040	1055	1045	1047	1030	1045	1045	1040	1470	1470	1450	1463									1060	1055	1045	1053					935	950	945	943					A3
A4																																									A4
A5																	915	915	920	917	910	905	900	905																	A5
A6	905	915	940	920	840	830	825	832	1610	1630	1620	1620	960	955	950	955																	1120	1125	1130	1125	1060	1070	1060	1063	A6
A7																	955	960	960	958									1070	1060	1040	1057									A7
B1																																									B1
B2	970	965	955	963					930	955	940	942									760	755	755	757									870	870	865	868	1330	1340	1345	1338	B2
B3																	885	880	885	883									1020	1020	980	1007									B3
B4					1025	1005	990	1007					1220	1225	1220	1222					875	880	870	875	1090	1100	1095	1095													B4
B5	950	960	955	955																																					B5
B6					915	900	895	903	1490	1490	1490	1490																	1060	1050	1045	1052	1070	1075	1085	1077	1030	1055	1060	1048	B6
B7													805	800	800	802	960	955	950	955	940	940	935	938	1195	1190	1175	1187													B7
B8																																									B8
C0																									970	960	950	960					895	905	900	900	1530	1540	1570	1547	C0
C1	980	980	980	980					1050	1060	1060	1057					920	925	935	927	925	915	930	923					1020	1020	1010	1017									C1
C2					1025	1025	1015	1022					1305	1300	1300	1302																									C2
C3																									1030	1020	1010	1020													C3
C4									1150	1220	1240	1203																	1050	1050	1045	1048	995	1010	1025	1010					C4
C5	925	960	960	948	1000	985	985	990					1090	1080	1070	1080	925	930	935	930	920	925	930	925	1080	1070	1065	1072									1090	1125	1130	1115	C5
C6																																									C6
C7													910	905	900	905													1060	1060	1050	1057									C7
C8	930	940	930	933	910	910	895	905	1500	1510	1510	1507					940	950	970	953	910	905	895	903	1140	1130	1125	1132					1105	1105	1105	1105	885	905	910	900	C8
C9																																									C9
D0																													1030	1025	1020	1025					1420	1425	1445	1430	D0
D1	970	960	985	972	990	985	975	983	1245	1250	1260	1252	1270	1250	1255	1258									980	975	970	975					1005	1010	1025	1013					D1
D2																	920	925	925	923	1030	1035	1045	1037																	D2
D3																																									D3
D4									1240	1230	1220	1230																	1040	1040	1025	1035									D4
D5	970	980	975	975	1020	1020	1010	1017					1090	1090	1080	1087																	1035	1045	1045	1042	1110	1110	1130	1117	D5
D6																	935	935	940	937	910	915	910	912	990	995	990	992													D6
D7																																									D7
D8	980	980	990	983					1390	1385	1380	1385	990	985	975	983													1050	1060	1060	1057	1045	1050	1045	1047	990	990	985	988	D8
D9					1030	1035	1025	1030													805	810	800	805	1090	1090	1065	1082													D9
E0																																									E0
E1					895	875	875	882	1325	1320	1320	1322					945	950	950	948					930	935	920	928	1065	1060	1045	1057									E1
E2																																					1130	1145	1145	1140	E2
E3	1000	990	990	993									1065	1060	1050	1058					1065	1075	1060	1067																	E3
E4					1005	1005	995	1002																									980	1020	1030	1010					E4
E5																	940	940	945	942																					E5
E6																																					1090	1100	1125	1105	E6
E7	990	990	980	987									1115	1090	1090	1098									880	885	875	880	1030	1020	990	1013									E7
E8					1110	1105	1090	1102	1110	1100	1090	1100					895	915	920	910	740	730	725	732									915	930	930	925					E8
E9																																									E9
F1																																									F1
F2	970	975	970	972	850	835	825	837																																	F2
F3																													1070	1060	1050	1060									F3
F4									1185	1180	1175	1180																									1110	1110	1140	1120	F4
F5													1130	1110	1105	1115	925	935	930	930													990	990	1000	993					F5
F6																					845	840	835	840	780	765	760	768													F6
F7	1010	990	975	992																																					F7
F8																																									F8
G2									1315	1320	1320	1318					975	985	990	983									1070	1045	1055	1057	1130	1130	1145	1135					G2
G3													855	825	815	832																					1080	1095	1105	1093	G3
G4																									755	755	745	752													G4
G5	1025	1030	1010	1022																	1000	1005	1010	1005																	G5
G6					1155	1140	1145	1147	825	825	815	822																					900	915	920	912					G6
G7													1265	1250	1260	1258	860	875	880	872									960	950	950	953					1085	1110	1140	1112	G7

μ	968,6				980,2				1231,1				1094,6				931,2				889,4				1008,8				1031,3				1007,0				1165,1				μ
σ	27,6				89,9				214,5				179,8				28,6				102,5				135,4				33,7				82,3				171,4				σ
	30-1			Avg	30-5			Avg	30-20-1			Avg	30-20-2			Avg	45-1			Avg	45-5			Avg	45-20			Avg	60-1			Avg	60-5			Avg	60-20			Avg	

A2: Pulse Electroplated Nickel Thickness Data

	30-1			Avg	30-5			Avg	30-10	45-1_2			Avg	45-5			Avg	45-20			Avg	60-1			Avg	60-5			Avg	60-20			Avg	
A2	1040	1065	1070	1058										755	765	765	762									1090	1110	1070	1090					A2
A3					735	725	715	725	1470	920	890	870	893					1230	1245	1235	1237									785	805	810	800	A3
A4																						930	930	930	930									A4
A5	980	990	1000	990																														A5
A6														1115	1125	1110	1117	675	665	670	670													A6
A7					1075	1045	1025	1048	745	910	905	900	905									985	975	965	975	855	855	830	847	1465	1470	1480	1472	A7
B1	1050	1055	1050	1052										780	790	790	787	1365	1330	1350	1348													B1
B2					740	720	725	728	1345																					730	740	745	738	B2
B3										940	920	910	923																					B3
B4																										1145	1140	1145	1143					B4
B5																						930	925	930	928									B5
B6																		775	775	790	780													B6
B7									720	890	890	885	888	1115	1110	1110	1112																	B7
B8	955	960	970	962	1080	1055	1040	1058														990	970	970	977	905	920	920	915	1345	1370	1400	1372	B8
C0										960	945	925	943					1565	1545	1550	1553					1270	1265	1270	1268	1015	1025	1050	1030	C0
C1	1025	1045	1045	1038	785	775	765	775	1340													925	910	910	915									C1
C2														955	960	970	962																	C2
C3																																		C3
C4	1005	1005	1000	1003	885	885	845	872						1025	1015	1025	1022					970	960	965	965									C4
C5									945	900	885	885	890					965	975	985	975					1080	1090	1090	1087	1160	1185	1200	1182	C5
C6																																		C6
C7																																		C7
C8					1030	1010	1000	1013	660					1100	1070	1070	1080																	C8
C9	940	930	910	927						870	870	860	867					825	825	835	828	990	960	965	972	1040	1070	1070	1060	1315	1325	1320	1320	C9
D0	1030	1015	1005	1017	890	870	860	873						1060	1065	1075	1067	1325	1320	1310	1318					1080	1070	1085	1078					D0
D1									1155	895	860	840	865									960	950	945	952					1290	1340	1350	1327	D1
D2																																		D2
D3																																		D3
D4	1020	1010	1010	1013	910	905	885	900	980					1040	1040	1045	1042	1025	1040	1025	1030	985	985	970	980	1110	1110	1120	1113	1200	1205	1230	1212	D4
D5										905	885	875	888																					D5
D6																																		D6
D7																																		D7
D8									785																					1090	1100	1105	1098	D8
D9	975	960	950	962	1010	995	965	990		855	810	845	837	1000	990	995	995	1160	1180	1185	1175	990	985	980	985	1180	1170	1190	1180					D9
E0																																		E0
E1																														1560	1610	1630	1600	E1
E2	990	985	990	988	945	925	915	928	865	910	905	895	903	1095	1100	1105	1100									1005	1020	1030	1018					E2
E3																						1000	1000	990	997									E3
E4																																		E4
E5																		1020	1020	1020	1020													E5
E6					910	905	880	898																		1110	1130	1140	1127	1090	1110	1125	1108	E6
E7	1000	990	985	992					900					965	970	970	968					1005	1000	990	998									E7
E8										845	830	825	833																					E8
E9																		1420	1420	1430	1423													E9
F1																																		F1
F2																		710	710	690	703													F2
F3																																		F3
F4	1020	1020	990	1010					835	915	905	885	902									1040	1020	1030	1030	1030	1040	1045	1038					F4
F5					905	885	875	888						1030	1035	1030	1032													1215	1240	1250	1235	F5
F6																																		F6
F7																																		F7
F8																																		F8
G2	1040	1045	1035	1040	1010	1005	990	1002		930	930	930	930	1195	1195	1190	1193					1040	1030	1030	1033	780	775	780	778					G2
G3									655									730	725	720	725													G3
G4																														1590	1640	1670	1633	G4
G5																																		G5
G6	1045	1040	1015	1033	815	790	785	797		805	790	775	790									1005	1010	990	1002	1165	1200	1205	1190					G6
G7									1000					835	825	835	832	1290	1305	1280	1292									665	665	660	663	G7
μ	1006				900				960	884				1005				1072				976				1062				1186				μ
σ	37				108				259	41				123				281				34				128				285				σ
	30-1			Avg	30-5			Avg	30-10	45-1_2			Avg	45-5			Avg	45-20			Avg	60-1			Avg	60-5			Avg	60-20			Avg	

B1: DC Electroplated Nickel Thickness Contour Plots

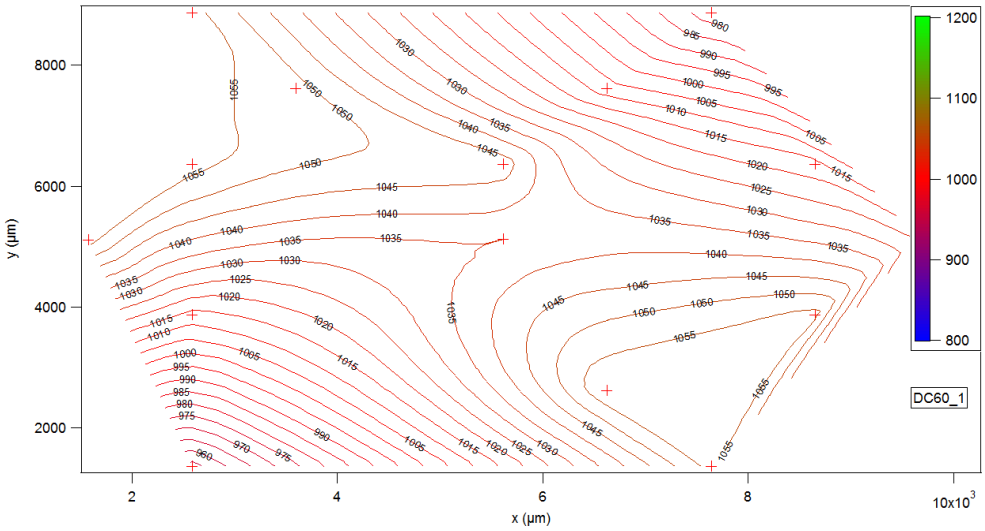

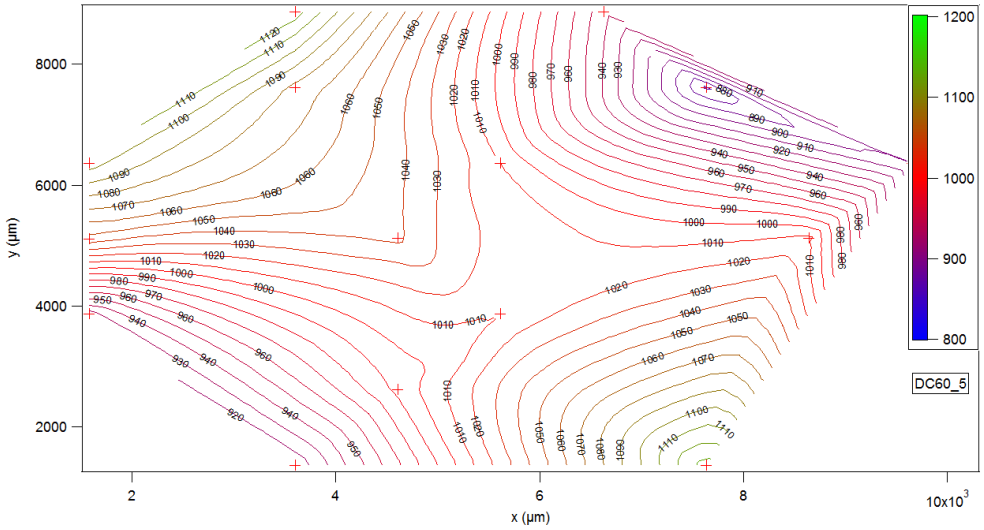

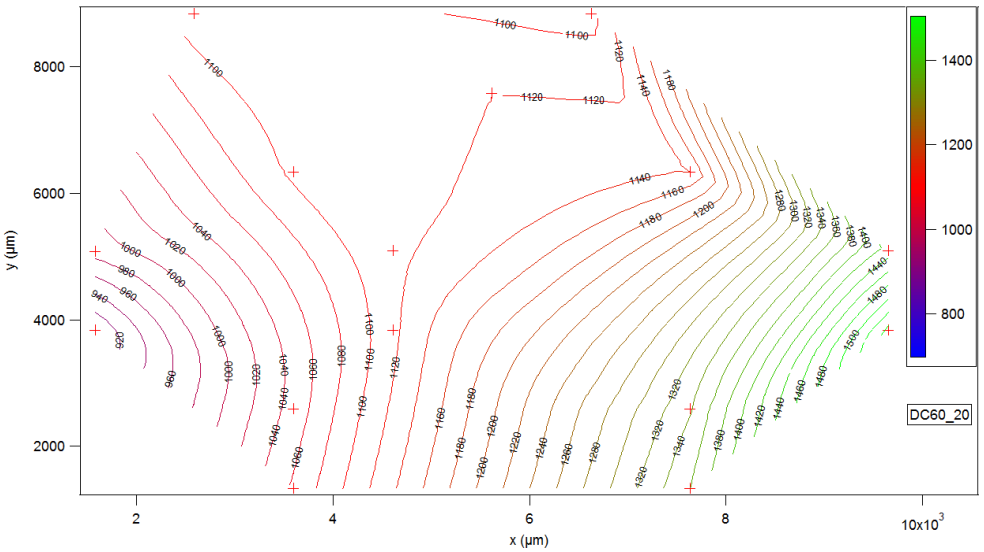

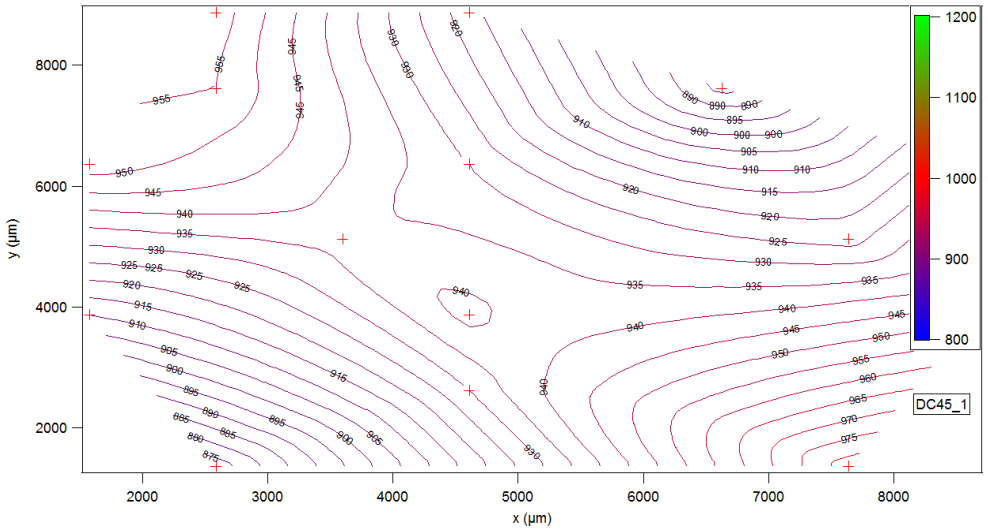
y (µm)
x (µm)
DC45_1

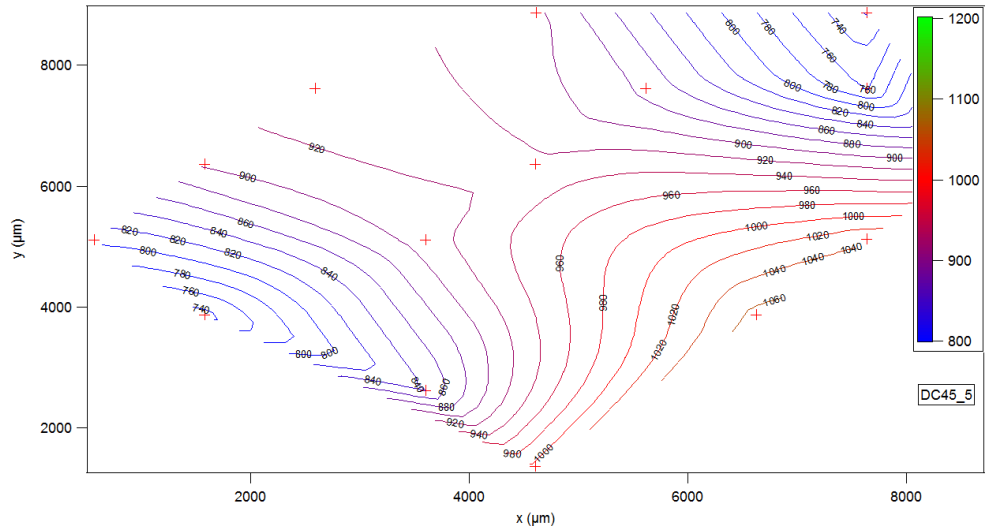
y (µm)
x (µm)
DC45_5

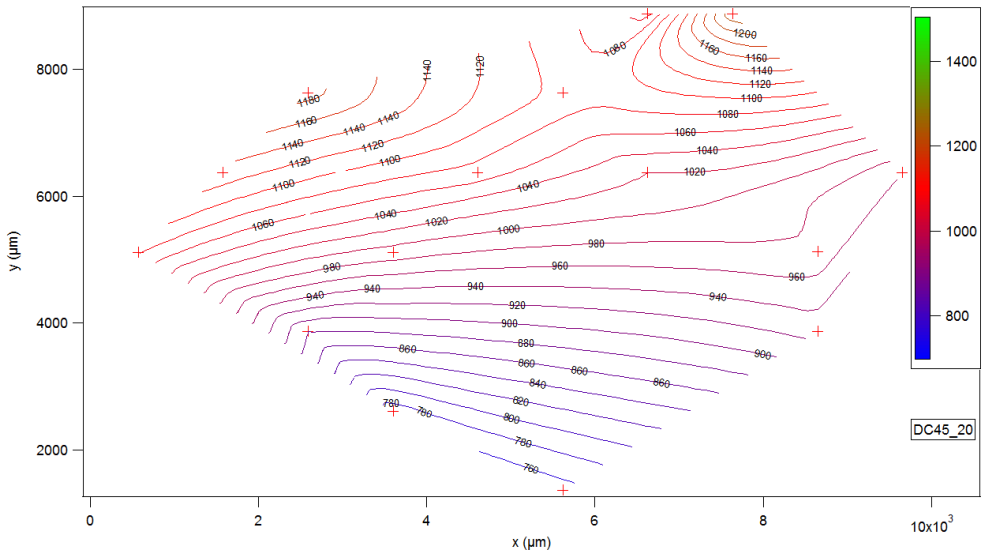
y (µm)
x (µm)
10x10^3
DC45_20

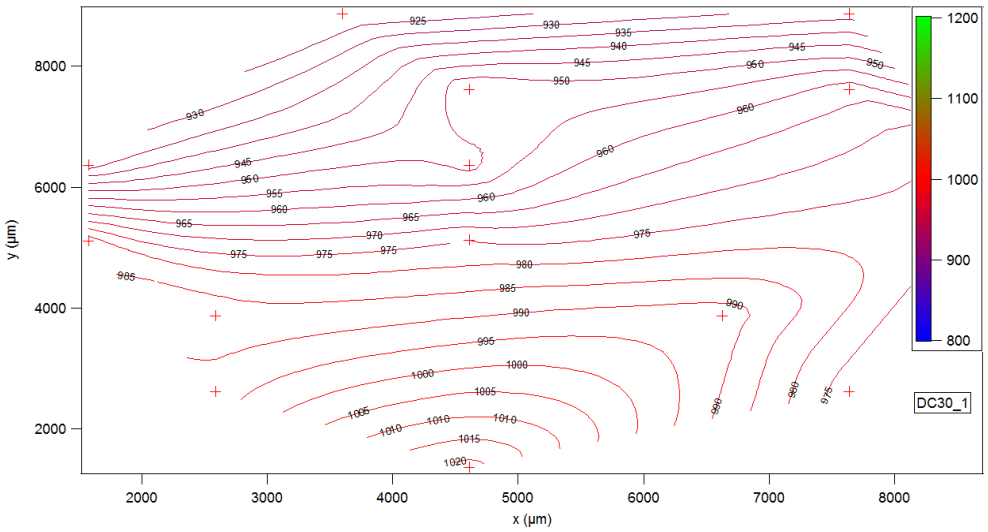
y (µm)
x (µm)
DC30_1

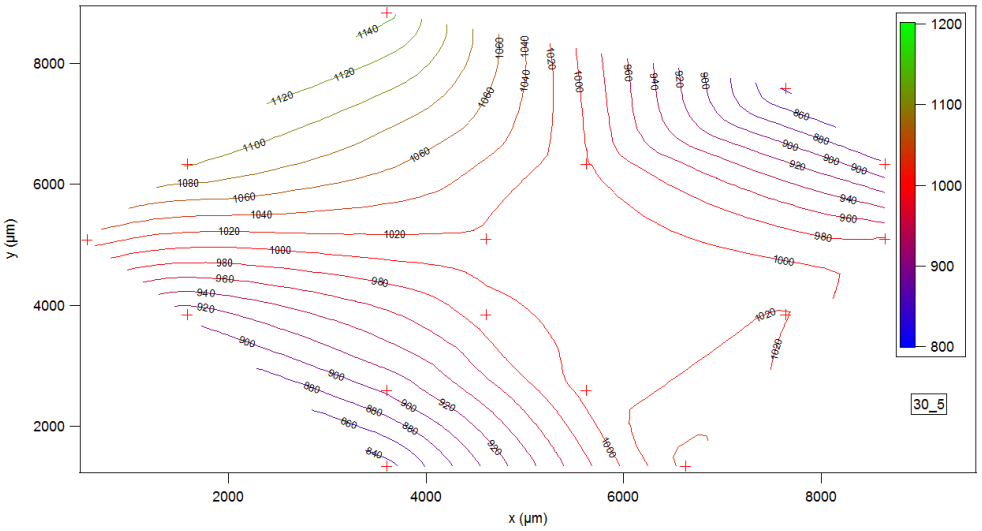
y (µm)
x (µm)
30_5

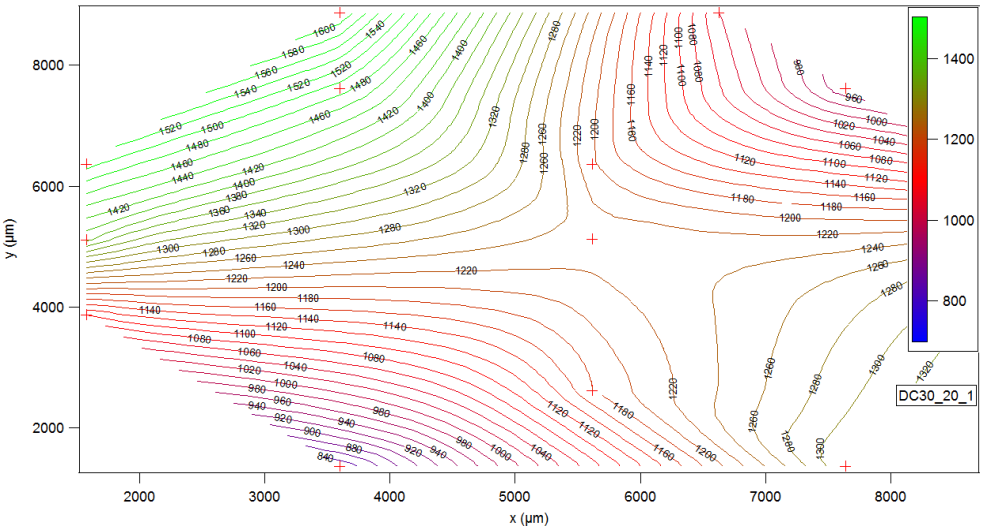
y (µm)
x (µm)
DC30_20_1

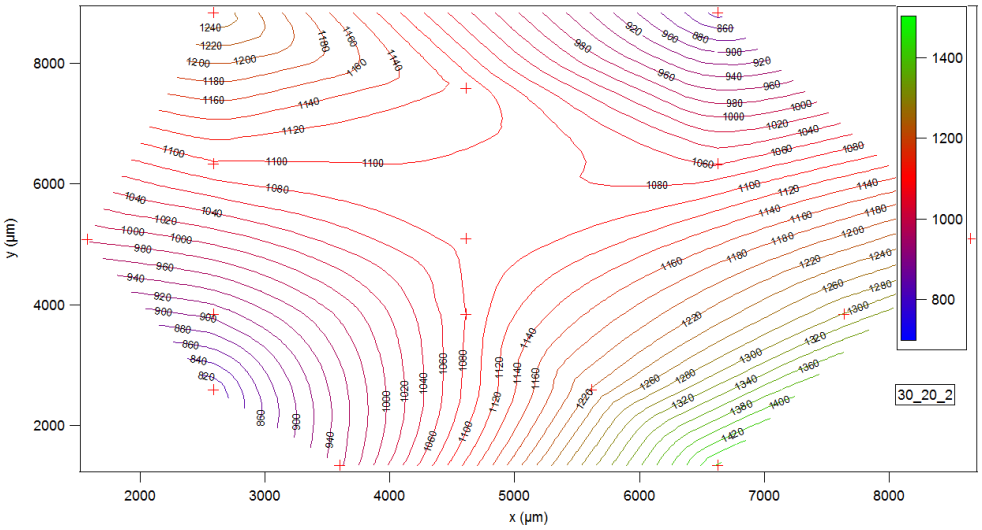
y (µm)
x (µm)
30_20_2
1400
1200
1000
800

B2: Pulse Electroplated Nickel Thickness Contour Plots

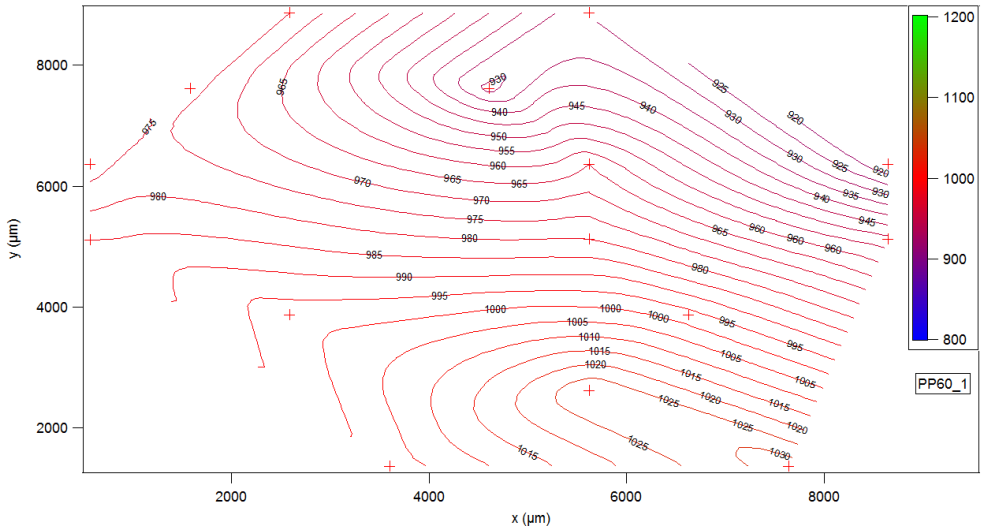

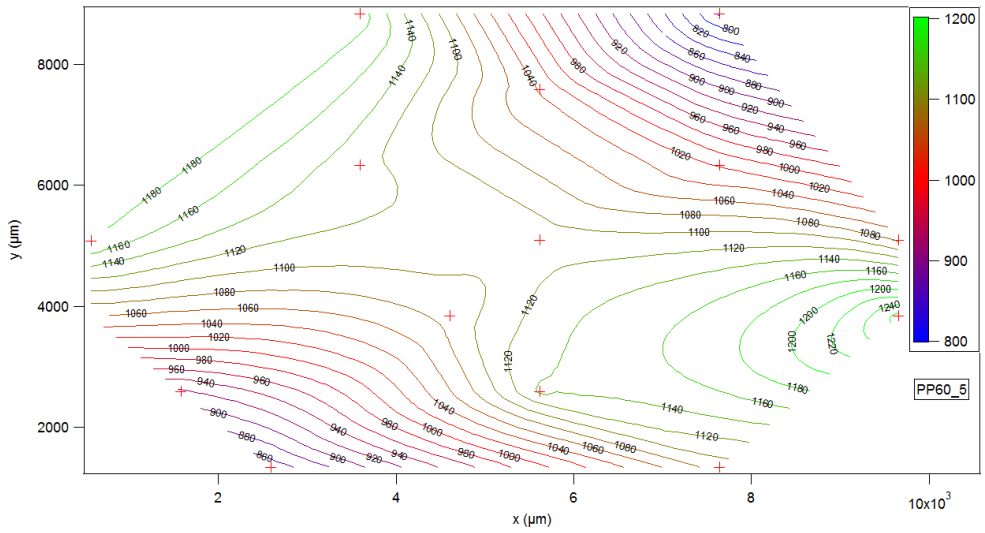

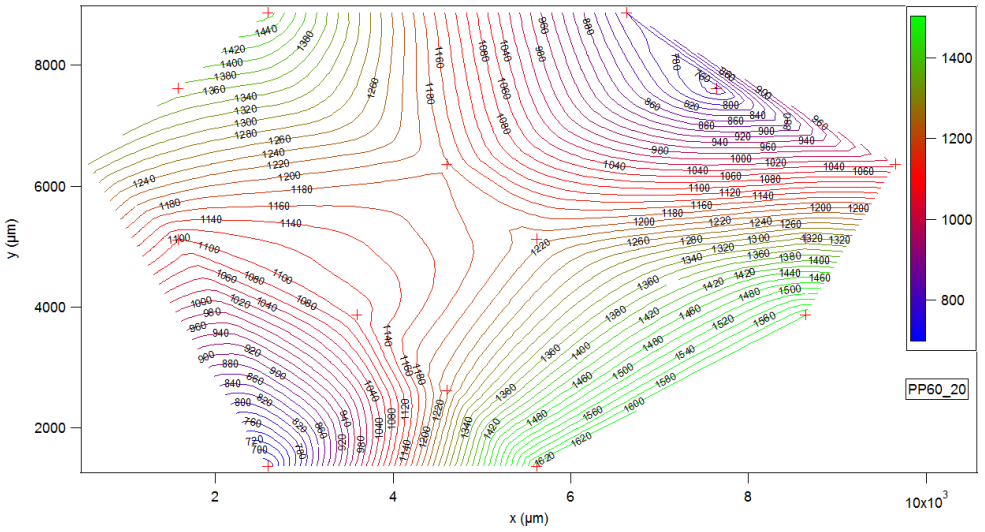

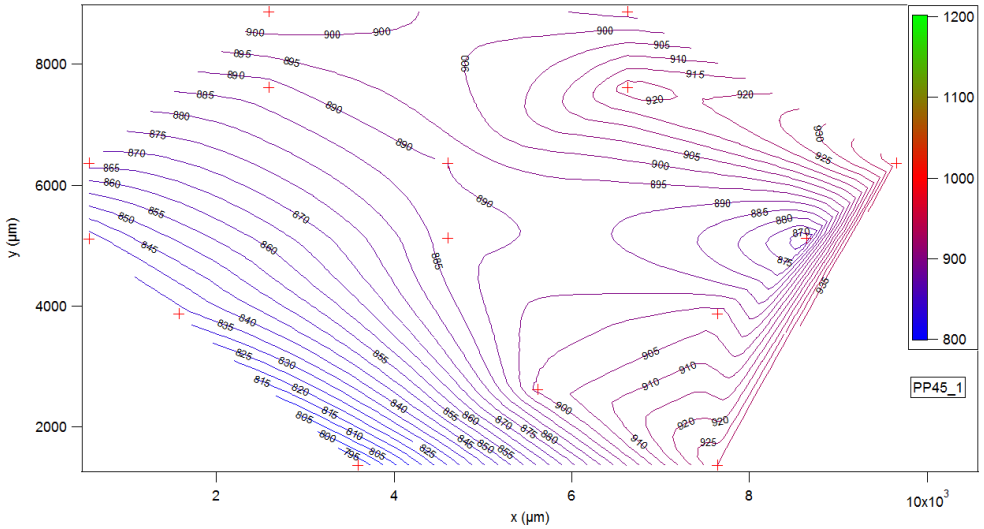
y (µm)
x (µm)
10x10^3
PP45_1

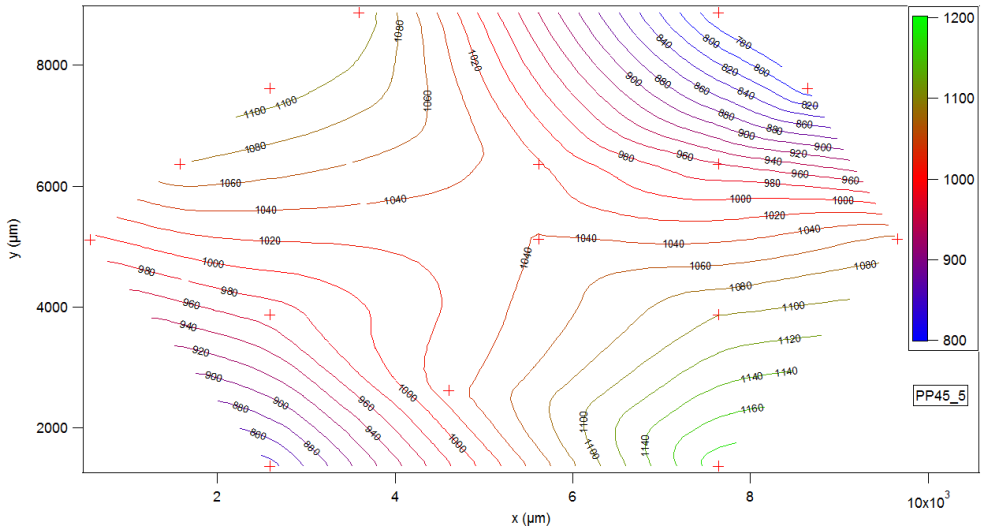
y (µm)
x (µm)
10x10^3
PP45_5

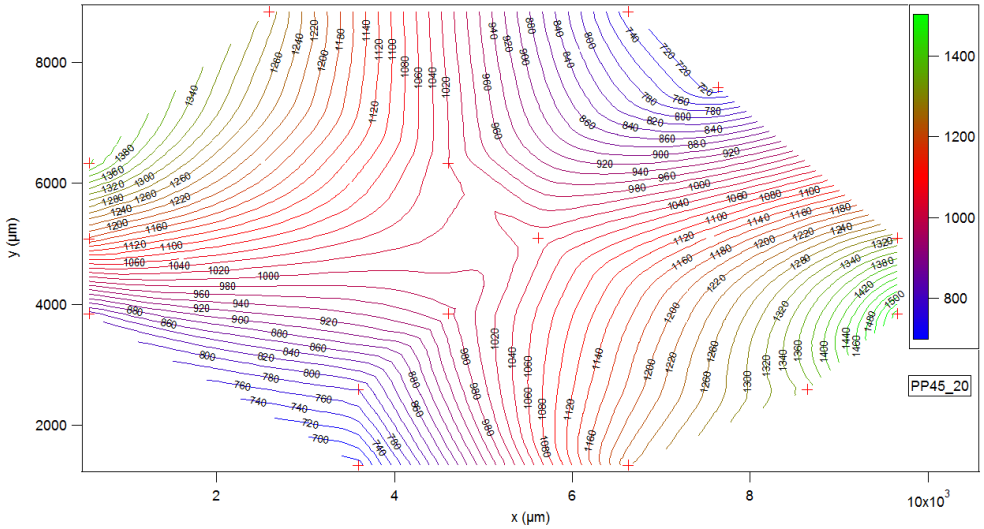
y (µm)
x (µm)
10x10^3
PP45_20

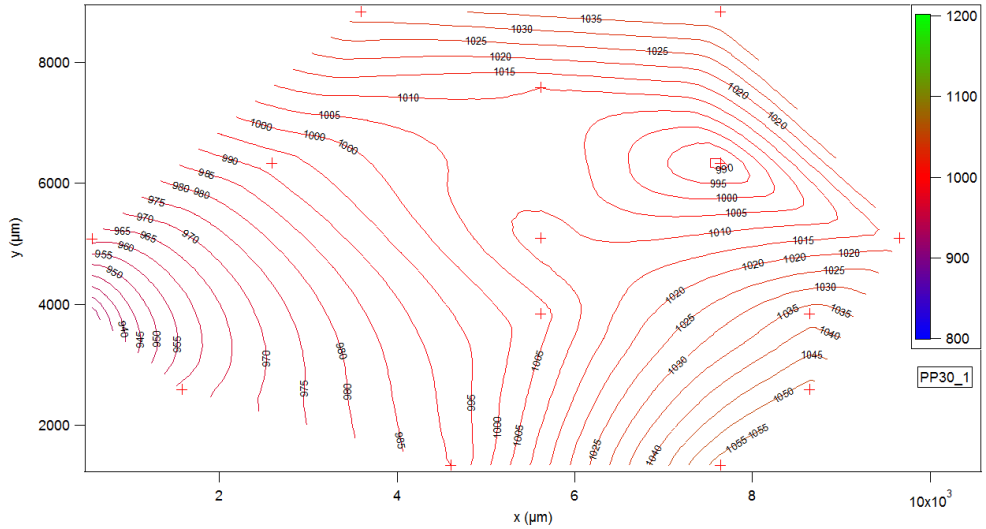
y (µm)
x (µm)
10x10^3
PP30_1

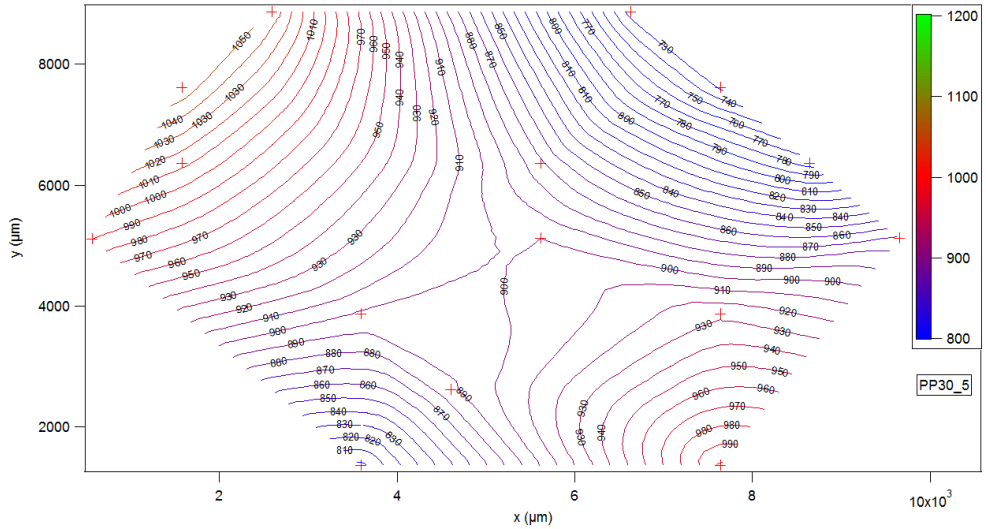
y (µm)
x (µm)
10x10^3
PP30_5

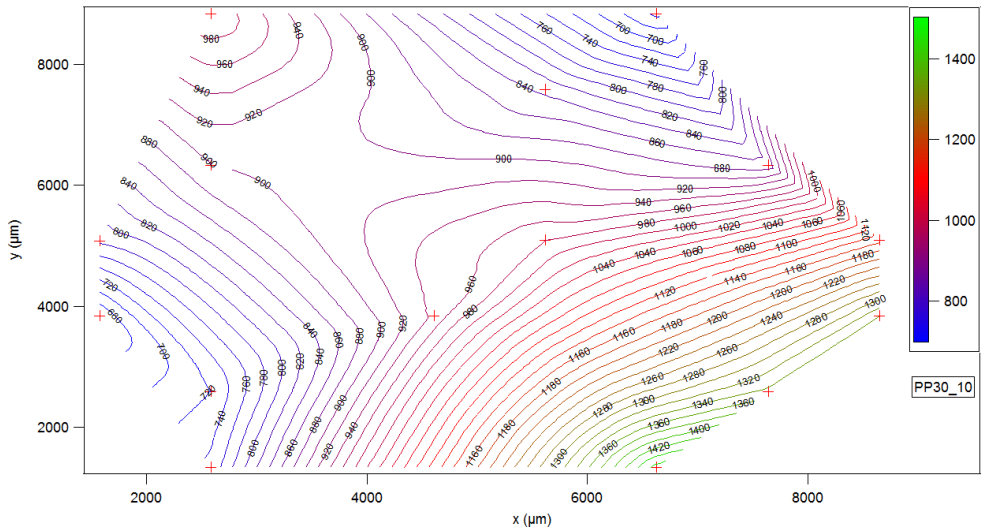
y (µm)
x (µm)
PP30_10

C1: Deflections of DC and Pulse Plated Cantilevers in terms of number of fringes

	The number of fringes of cantilevers																
	DC30_5	DC30_20_1	DC30_20_2	DC45_5	DC45_20	DC60_1	DC60_5	DC60_20	PP30_1	PP30_5	PP30_10	PP45_5	PP45_20	PP60_1	PP60_5	PP60_20	
A2				13		4		7,5				9,5					A2
A3	-3	10	2,5		11		16		13							8,5	A3
A4									14						13,5		A4
A5				12	5												A5
A6		6	4				13	11		5	4	12,5	-5			9	A6
A7	-6					4						12			18	10	A7
B1									10			15,5					B1
B2		10		8			15	8	13	6							B2
B3			3			4			9	7		9,5			15		B3
B4	-2,5			9	8				12							6	B4
B5													-7				B5
B6	-1	6				4,5	14	12				10,5			11	5	B6
B7			4	9	4							11		2		7	B7
B8									14					2		9	B8
C0				14	12	2,5	15	7					-4		12		C0
C1		8	2						15	4							C1
C2	-3											11	-10			4	C2
C3					8						1						C3
C4		7			8	4	14						-3		10,5	4	C4
C5	-2		4	8				9			1				12		C5
C6												9					C6
C7			6			4			15,5			10,5					C7
C8	3,5	5		7	5		15	10					-10	3			C8
C9														1	10		C9
D0						3,5		6,5	16			15			13,5		D0
D1	-4	8	3		10		12								10,5		D1
D2			3	12													D2
D3						3,5						11		2		6,5	D3
D4		6								5							D4
D5	-1						13	9	11								D5
D6				10,5	6,5					6	5		-9				D6
D7										5		12					D7
D8		5	6			3	13	7									D8
D9	5			11	10									3	7		D9
E0											-2						E0
E1	-1,5	7	4			3,5				4	-4				9		E1
E2					7			8	11	9	-1		-9				E2
E3				11								10	-7			5,5	E3
E4							13							1		6	E4
E5									15,5								E5
E6								10	10						7	6	E6
E7			6		9	3											E7
E8	4	7		10,5			13					13					E8
E9									16						7		E9
F1										5							F1
F2	-3								12		-3	14					F2
F3			5			3		7									F3
F4		6											-4			7	F4
F5							13										F5
F6				11	12,5				9					2			F6
F7									12							5,5	F7
F8															7		F8
G2		7	3		5			3,5				12					G2
G3						2	12							4	10	8	G3
G4					8			6,5								9	G4
G5				13								14					G5
G6	3	10			15		16	8		4							G6
G7			4			1											G7
μ (μm)	-0,21	1,80	0,99	2,65	2,12	0,83	3,45	2,03	3,17	1,36	0,03	2,94	-1,70	0,56	2,70	1,71	μ (μm)
σ (μm)	0,84	0,42	0,32	0,51	0,75	0,23	0,33	0,51	0,59	0,38	0,81	0,48	0,66	0,24	0,79	0,46	σ (μm)
	DC30_5	DC30_20_1	DC30_20_2	DC45_5	DC45_20	DC60_1	DC60_5	DC60_20	PP30_1	PP30_5	PP30_10	PP45_5	PP45_20	PP60_1	PP60_5	PP60_20	

C2: Deflections of DC and Pulse Plated Cantilevers determined by focus difference

	DC30_1				DC45_1				PP45_1				
	Support	Tip	Difference	Corrected	Support	Tip	Difference	Corrected	Support	Tip	Difference	Corrected	
A2													A2
A3	23,8	29,5	5,7	4,53	44,60	50,00	5,40	4,29					A3
A4													A4
A5					46,60	51,80	5,20	4,13					A5
A6	24,9	30,5	5,6	4,45									A6
A7					43,40	48,30	4,90	3,90					A7
B1													B1
B2	31	37	6	4,77									B2
B3					44,60	50,50	5,90	4,69					B3
B4													B4
B5	31,9	37,5	5,6	4,45									B5
B6													B6
B7					43,40	48,40	5,00	3,98					B7
B8													B8
C0													C0
C1	30,1	35,5	5,4	4,29	39,30	44,30	5,00	3,98					C1
C2													C2
C3													C3
C4					45,80	50,60	4,80	3,82					C4
C5	30,9	35,9	5	3,98									C5
C6													C6
C7													C7
C8	28,1	32,2	4,1	3,26									C8
C9					37,90	43,80	5,90	4,69					C9
D0					41,40	47,50	6,10	4,85					D0
D1	29,5	33,3	3,8	3,02					29,70	35,70	6,00	4,77	D1
D2													D2
D3													D3
D4									35,30	38,90	3,60	2,86	D4
D5	24,9	31,5	6,6	5,25									D5
D6									39,60	43,70	4,10	3,26	D6
D7					53,20	58,10	4,90	3,90					D7
D8	24,9	30,4	5,5	4,37									D8
D9													D9
E0					54,80	60,50	5,70	4,53					E0
E1													E1
E2													E2
E3	26,9	32,9	6	4,77									E3
E4									17,50	21,90	4,40	3,50	E4
E5					52,00	58,10	6,10	4,85					E5
E6									43,10	47,80	4,70	3,74	E6
E7													E7
E8	24	30,5	6,5	5,17	57,80	63,70	5,90	4,69					E8
E9													E9
F1									47,50	52,00	4,50	3,58	F1
F2													F2
F3	26,7	32,5	5,8	4,61									F3
F4					53,30	59,00	5,70	4,53					F4
F5									45,40	50,30	4,90	3,90	F5
F6													F6
F7													F7
F8	21,3	28,8	7,5	5,96					46,00	51,40	5,40	4,29	F8
G2					51,60	57,70	6,10	4,85					G2
G3													G3
G4													G4
G5	27	33,4	6,4	5,09					45,60	52,00	6,40	5,09	G5
G6									30,40	38,40	8,00	6,36	G6
G7					46,40	52,30	5,90	4,69	45,90	53,20	7,30	5,80	G7
μ (μm)				4,53				4,40				4,29	μ (μm)
σ (μm)				0,74				0,39				1,10	σ (μm)
	DC30_1				DC45_1				PP45_1				

D: Modulus of Elasticity Measurment Data of DC Plated Cantilevers

	30_1				30_5				30_20_1				30_20_2				45_5				45_1				45_20				60_1				60_5				N60-20			60_20				
	t (nm)	f (Hz)	E (GPa)	Q	t (nm)	f (Hz)	E (GPa)	Q	t (nm)	f (Hz)	E (GPa)	Q	t (nm)	f (Hz)	E (GPa)	Q	t (nm)	f (Hz)	E (GPa)	Q	t (nm)	f (Hz)	E (GPa)	Q	t (nm)	f (Hz)	E (GPa)	Q	t (nm)	f (Hz)	E (GPa)	Q	t (nm)	f (Hz)	E (GPa)	Q				t (nm)	f (Hz)	E (GPa)	Q	
A2																													977	66488	157,3	154					1360	1360	1360	1360	86850	138,4	192	A2
A3	930	60537	143,8						1040	67717	143,9	115													1053	70904	153,8						943	60660	140,4									A3
A4													1294	90251	165,1	168																												A4
A5					904	61619	157,7	143									905	62360	161,2	110	917	56396	128,5																					A5
A6	920	58936	139,3						1620	104227	140,5	259																					1125	70123	131,9		1060	1070	1060	1063	68996	142,9	138	A6
A7																					958	60285	134,3	169					1057	71557	155,7	147										A7
B1																																												B1
B2	963	62511	142,9	135					942	62597	150,0	118									866	53368	128,9	73													1330	1340	1345	1338	84909	136,6		B2
B3																													1007	68126	155,5	134										B3
B4					1007	66487	148,1	133					1222	82275	154,0	164	875	68636	208,9	126					1095	73860	154,4	158	1022	70019	159,3	123										B4
B5									1353	89744	149,3	215																																B5
B6					903	60157	150,5	118																									1077	68869	138,9		1030	1055	1060	1048	65398	132,1	128	B6
B7	950	59754	134,3														938	67344	174,8	129	955	59724	132,8	94	1187	78424	148,2	164															B7
B8																																												B8
C0																									960	63657	149,2						900	57560	138,8		1530	1540	1570	1547	95517	129,5	234	C0
C1	980	61809	135,0						1057	68458	142,5	160									927	52236	107,9	78					1017	65047	138,9	131										C1
C2																																												C2
C3													1228	82609	153,6	174									1020	70897	164,0	125															C3
C4																									1046	71454	158,4	155	1048	70578	153,8	165	1010	65032	140,7								C4
C5	948	61833	144,3		990	65980	150,8	128					1080	71452	148,6	149	925	72906	210,9	144	930	57648	130,4													1090	1125	1130	1115	70103	134,2	132	C5
C6									1355	88829	145,9	225																																C6
C7													905	61370	156,1	137													1057	70954	153,0	144										C7
C8	933	57801	130,2	101	905	59085	144,7	139									903	63371	167,0	114	953	59231	131,0	104	1132	76491	155,1	166					1105	74259	153,3		885	905	910	900	58038	141,2	114	C8
C9																																												C9
D0																													1025	68135	150,0	148	1006	64838	141,0		1420	1425	1445	1430	90652	136,4	190	D0
D1					983	65898	152,4	140					1258	87033	162,4	251									975	68672	168,4												1382	81405	117,8	171	D1
D2	973	64067	147,2		992	65672	148,8	151									1037	68063	146,3	138	923	56114	125,4	135																			D2
D3																																												D3
D4									1230	80586	145,7	157																	1035	67965	146,4	140										D4
D5	975	63891	145,8		1017	67575	150,0	148					1087	69661	139,5	242									989	71837	179,1	104									1110	1110	1130					D5
D6																	912	68531	191,8	140	937	57624	128,5	140																			D6
D7																																												D7
D8	983	63111	139,8	131																									1057	70397	150,7	150	1047	67901	142,9		990	990	985	988	62746	136,8	104	D8
D9																	805	52122	142,3	103					1082	72967	154,5	116															D9
E0									1354	94427	165,1	220																																E0
E1					882	57888	146,3	119	1322	83163	134,4	163									948	57874	126,4	107					1057	71273	154,4	137										E1
E2																									920	66235	175,9	101									1130	1145	1145	1140	73562	141,3	152	E2
E3	993	63899	140,5		962	64027	150,4	129					1058	73095	161,9	184	1067	82329	202,2	159																								E3
E4																																												E4
E5																					942	58567	131,3	84																			E5
E6	989	65115	147,1	125									1088	73619	155,4	184																					1090	1100	1125	1105	71107	140,6	116	E6
E7					1077	71548	149,8	132																					1013	66781	147,4	154										E7
E8					1102	73301	150,3	124									732	50571	162,2	88	910	56504	130,9	104	872	60449	163,1	110															E8
E9																																	904	61798	158,6									E9
F1																																												F1
F2	972	67580	164,2		837	52657	134,4	116																																				F2
F3																													1060	69484	145,9	139										F3
F4																																					1110	1110	1140	1120	68355	126,4	152	F4
F5													1115	68871	129,5	168					930	57531	129,9										993	65398	147,1									F5
F6																	840	60409	175,5	115																							F6
F7	992	65685	148,9																																								F7
F8																																												F8
G2									1318	84364	139,0										983	61284	131,8	143					1057	72573	160,1	140										G2
G3																																	1079	68763	137,9		1080	1095	1105	1093	66556	125,8	109	G3
G4													939	67728	176,6	138																											G4
G5	1022	67344	147,5														1005	70619	167,6	121	916	54640	120,8	90									968	62629	142,1			1123					G5
G6					1147	71224	131,0	150													894	55987	133,1	109																			G6
G7													1258	81846	143,6	195													953	63745	151,8	137					1085	1110	1140					G7
μ			143,4				147,5				145,6				153,9				175,9				128,2				160,3				152,0				142,8			1164,2			134,3			μ
σ			7,9				7,0				8,3				12,5				23,0				6,4				10,0				5,7				7,2			169,6			7,2			σ
	30_1				30_5				30_20_1				30_20_2				45_5				45_1				45_20				60_1				60_5							60_20				

E: Cantilever Deflection Evolution with Time

	M0	M1	WLI		M0	M1	WLI		M0	M1	WLI		M0	M1
	30_5				30_20_1				30_20_2				60_1	
A2													1	0,75
A3	-0,8	-1	-1,464		-2,5	-3	-3,454		-0,625	-0,75	-0,72			
A4														
A5														
A6					-1,5	-1,5	-1,5		-1	-1,25	-1,4372			
A7													1	1
B1														
B2					-2,5	-2,875	-3,269							
B3									-0,75	-0,75	-0,7846		1	0,75
B4	-0,6	-0,9	-0,802											
B5														
B6	-0,3	-0,5	-0,48										1,125	1
B7									-1	-1,5	-1,653			
B8														
C0													0,625	0,25
C1					-2	-2,375	-2,82		-0,5	-0,625	-0,7065			
C2	-0,8	-1,1	-1,301											
C3														
C4					-1,75	-2,125	-2,9						1	0,75
C5	-0,5	-0,8	-0,78						-1	-1,25	-1,309			
C6														
C7									-1,5	-1,5	-1,6624		1	0,75
C8	0,88	0,63	0,503											
C9														
D0													0,875	0,75
D1	-1	-1,5	-1,451		-2	-2,25	-2,492		-0,75	-0,875	-0,8747			
D2									-0,75	-1	-1,213			
D3													0,875	0,5
D4					-1,5	-1,75	-2,007							
D5	-0,3	-0,5	-0,494											
D6														
D7														
D8									-1,5	-1,75	-1,817		0,75	0,5
D9	1,25	1,13	1,104											
E0														
E1									-1	-1,375	-1,517		0,875	0,625
E2														
E3														
E4														
E5														
E6														
E7									-1,5	-1,75	-2,083		0,75	0,5
E8	1	0,75	0,855		-1,75	-1,875	-2,148							
E9														
F1														
F2	-0,8	-1,3	-1,215											
F3									-1,25	-1,5	-1,713		0,75	0,625
F4					-1,5	-1,875	-2,098							
F5														
F6														
F7														
F8														
G2					-1,75	-2	-2,339		-0,75	-1,25	-1,452			
G3													0,5	0,25
G4														
G5														
G6	0,75	0,5	0,786		-2,5	-3	-3,374							
G7									-1	-1,25	-1,327			
μ (μm)	-0,08	-0,38	-0,39		-1,93	-2,24	-2,58		-0,99	-1,23	-1,35		0,87	0,64
σ (μm)	0,81	0,89	0,96		0,40	0,52	0,63		0,32	0,36	0,42		0,17	0,23
	30_5				30_20_1				30_20_2				60_1	

Bibliography

[1] S. A. Watson, "Nickel Sulfamate Solutions," 1998.

[2] E. Slavcheva*, et al.*, "Electrodeposition and properties of NiW films for MEMS application," *Electrochimica Acta,* vol. 50, pp. 5573-5580, 2005.

[3] A. Chakraborty and C. Luo, "Fabrication and application of metallic nano-cantilevers," *Microelectronics Journal,* vol. 37, pp. 1306-1312, 2006.

[4] J. K. Luo*, et al.*, "Young's modulus of electroplated Ni thin film for MEMS applications," *Materials Letters,* vol. 58, pp. 2306-2309, 2004.

[5] S.-H. Kim*, et al.*, "Mechanical behavior of mismatch strain-driven microcantilever," *Microelectronics Journal,* vol. 38, pp. 371-380, 2007.

[6] B.-H. Kim*, et al.*, "Process effects of double step DRIE and Ni–Co electroplating for a trench-type cantilever probe for a fine-pitched MEMS probe card," *Sensors and Actuators A: Physical,* vol. 152, pp. 252-260, 2009.

[7] Y.-h. Zhang*, et al.*, "Electroplating of low stress permalloy for MEMS," *Materials Characterization,* vol. 57, pp. 121-126, 2006.

[8] Y. B. Wu*, et al.*, "Fabrication of low-stress low-stiffness leveraged cantilever beam for bistable mechanism," *Microelectronic Engineering,* vol. 87, pp. 2035-2041, 2010.

[9] J. Matovic*, et al.*, "Bimaterial infrared detector with efficient suppression of interference from ambient temperature," in *Microelectronics, 2004. 24th International Conference on*, 2004, pp. 349-352 vol.1.

[10] S. Peraud*, et al.*, "Determination of young's modulus by a resonant technique applied to two dynamically ion mixed thin films," *Thin Solid Films,* vol. 292, pp. 55-60, 1997.

[11] K. Yong-Jun and M. G. Allen, "In situ measurement of mechanical properties of polyimide films using micromachined resonant string structures," *Components and Packaging Technologies, IEEE Transactions on,* vol. 22, pp. 282-290, 1999.

[12] Y. Chisheng*, et al.*, "Comments on determining the elastic modulus of a thin film using the micromachined free–free beam," *Journal of Micromechanics and Microengineering,* vol. 15, p. 351, 2005.

[13] C.-L. Dai and Y.-M. Chang, "A resonant method for determining mechanical properties of Si3N4 and SiO2 thin films," *Materials Letters,* vol. 61, pp. 3089-3092, 2007.

[14] L. Kiesewetter*, et al.*, "Determination of Young's moduli of micromechanical thin films using the resonance method," *Sensors and Actuators A: Physical,* vol. 35, pp. 153-159, 1992.

[15] J. McCarthy*, et al.*, "FIB micromachined submicron thickness cantilevers for the study of thin film properties," *Thin Solid Films,* vol. 358, pp. 146-151, 2000.

[16] L. Sekaric*, et al.*, "Nanomechanical resonant structures in silicon nitride: fabrication, operation and dissipation issues," *Sensors and Actuators A: Physical,* vol. 101, pp. 215-219, 2002.

[17] O. Kraft and C. A. Volkert, "Mechanical Testing of Thin Films and Small Structures," *Advanced Engineering Materials,* vol. 3, pp. 99-110, 2001.

[18] J.-Å. Schweitz and F. Ericson, "Evaluation of mechanical materials properties by means of surface micromachined structures," *Sensors and Actuators A: Physical,* vol. 74, pp. 126-133, 1999.

[19] V. Srikar and S. Spearing, "A critical review of microscale mechanical testing methods used in the design of microelectromechanical systems," *Experimental Mechanics,* vol. 43, pp. 238-247, 2003.

[20] Y. Taechung and K. Chang-Jin, "Measurement of mechanical properties for MEMS materials," *Measurement Science and Technology,* vol. 10, p. 706, 1999.

[21] R. P. Vinci and J. J. Vlassak, "Mechanical behavior of thin films," *Ann. Rev. Mater. Sci.,* vol. 26, pp. 431-462 1996.

[22] H. Majjad*, et al.*, "Dynamic determination of Young's modulus of electroplated nickel used in LIGA technique," *Sensors and Actuators A: Physical,* vol. 74, pp. 148-151, 1999.

[23] T. Fritz*, et al.*, "Material characterisation of electroplated nickel structures for microsystem technology," *Electrochimica Acta,* vol. 47, pp. 55-60, 2001.

[24] J. Amblard*, et al.*, "Inhibition and nickel electrocrystallization," *Journal of Applied Electrochemistry,* vol. 9, pp. 233-242, 1979.

[25] S. Abel, "PhD Thesis," Universitat Kaiserslautern, 1996.

[26] E. Budevski*, et al.*, "Electrochemical phase formation and growth VCH," *Journal of Electroanalytical Chemistry,* vol. 433, pp. 227-228, 1997.

[27] T. Fritz*, et al.*, "Determination of Young's modulus of electroplated nickel," *Electrochimica Acta,* vol. 48, pp. 3029-3035, 2003.

[28] K. P. Larsen*, et al.*, "MEMS device for bending test: measurements of fatigue and creep of electroplated nickel," *Sensors and Actuators A: Physical,* vol. 103, pp. 156-164, 2003.

[29] C. Hsu*, et al.*, "Measuring thin film elastic modulus using a micromachined cantilever bending test by nanoindenter," *Journal of Micro/Nanolithography, MEMS and MOEMS,* vol. 6, pp. 033011-7, 2007.

[30] H. C. Nathanson*, et al.*, "The resonant gate transistor," *Electron Devices, IEEE Transactions on,* vol. 14, pp. 117-133, 1967.

[31] D. Son*, et al.*, "Film-thickness considerations in microcantilever-beam test in measuring mechanical properties of metal thin film," *Thin Solid Films,* vol. 437, pp. 182-187, 2003.

[32] W. Fang*, et al.*, "Determining thermal expansion coefficients of thin films using micromachined cantilevers," *Sensors and Actuators A: Physical,* vol. 77, pp. 21-27, 1999.

[33] S.-H. Lee*, et al.*, "Evaluation of elastic modulus and yield strength of Al film using an electrostatically actuated test device," *Thin Solid Films,* vol. 408, pp. 223-229, 2002.

[34] K. E. Petersen and C. R. Guarnieri, "Young’s modulus measurements of thin films using micromechanics," *Journal of Applied Physics,* vol. 50, pp. 6761-6766, 1979.

[35] S. G. Nilsson*, et al.*, "Size effect on Young’s modulus of thin chromium cantilevers," *Applied Physics Letters,* vol. 85, pp. 3555-3557, 2004.

[36] Z. M. Zhou*, et al.*, "Residual Strains in a Nanometer Thick Cr Film Measured on Micromachined Beams," *J. Mater. Sci. Technol.,* vol. 25, pp. 77-80, 2009.

[37] J. Zhang, "Determination of Young's modulus of electroplated nickel–iron (Ni/Fe) and micro-machined Si thin films by the balance method," *Journal of Materials Processing Technology,* vol. 123, pp. 329-335, 2002.

[38] M. P. de Boer*, et al.*, "On-chip laboratory suite for testing of free-standing metal film mechanical properties, Part II – Experiments," *Acta Materialia,* vol. 56, pp. 3313-3326, 2008.

[39] T. Itoh*, et al.*, "Electroplated Ni microcantilever probe with electrostatic actuation," *Sensors and Actuators A: Physical,* vol. 123–124, pp. 490-496, 2005.

[40] V. Ostasevicius*, et al.*, "Hybrid numerical—experimental approach for investigation of dynamics of microcantilever relay system," *Optics and Lasers in Engineering,* vol. 43, pp. 63-73, 2005.

[41] A. Ozturk*, et al.*, "A Magnetically Actuated Resonant Mass Sensor With Integrated Optical Readout," *Photonics Technology Letters, IEEE,* vol. 20, pp. 1905-1907, 2008.

[42] E. Timurdogan*, et al.*, "Detection of human κ-opioid antibody using microresonators with integrated optical readout," *Biosensors and Bioelectronics,* vol. 26, pp. 195-201, 2010.

[43] S. He*, et al.*, "Characterization of Young's modulus and residual stress gradient of MetalMUMPs electroplated nickel film," *Sensors and Actuators A: Physical,* vol. 154, pp. 149-156, 2009.

[44] C. W. Baek and Y.-K. Kim, "Measurment of mechanical properties of electroplated gold films using micromachined beam structures," *Sensors and Actuators,* vol. 117, pp. 17-27, 2005.

[45] V. Mulloni*, et al.*, "Controlling stress and stress gradient during the release process in gold suspended micro-structures," *Sensors and Actuators A: Physical,* vol. 162, pp. 93-99, 2010.
[46] S. H. Hong*, et al.*, "Characterization of elastic moduli of Cu thin films using nanoindentation technique," ed: Elsevier, 2005.
[47] E. M. Chow*, et al.*, "High voltage thin film transistors integrated with MEMS," *Sensors and Actuators A: Physical,* vol. 130–131, pp. 297-301, 2006.
[48] Q. He*, et al.*, "Comparison of residual stress measurement in thin films using surface micromachining method," *Thin Solid Films,* vol. 516, pp. 5318-5323, 2008.
[49] *Modern Electroplating*, Fourth ed.: John Wiley & Sons, Inc, 2000.
[50] R. Sandberg*, et al.*, "Temperature and pressure dependence of resonance in multi-layer microcantilevers," *Journal of Micromechanics and Microengineering,* vol. 15, p. 1454, 2005.
[51] Y. Tsuru*, et al.*, "Effects of chloride, bromide and iodide ions on internal stress in films deposited during high speed nickel electroplating from a nickel sulfamate bath," *Journal of Applied Electrochemistry,* vol. 30, pp. 231-238, 2000.
[52] C. B. Sanborn, "Electroforming applications-why they exists," 1972.
[53] W. A. Wesley, "Nickel atoms, ions and electrons," *Trans. Institude of Metal Finishing* vol. 33, 1956.
[54] G. A. DiBari, "Notes on nickel anode materials," *Plating Surf. Finish.,* vol. 66, 1979.
[55] M. E. Thomas*, et al.*, "The use of surface profilometers for the measurement of surface curvature," *J. Micromechanics and Microengineering,* vol. 6, p. 2570, 1998.
[56] T. Ikehara*, et al.*, "New method for an accurate determination of residual strain in polycrystalline silicon films by analysing resonant frequencies of micromachined beams," *Journal of Micromechanics and Microengineering,* vol. 11, p. 55, 2001.
[57] S. Suresh*, et al.*, "Spherical indentation of compositionally graded materials: Theory and experiments," *Acta Materialia,* vol. 45, pp. 1307-1321, 1997.
[58] U. Welzel*, et al.*, "Stress analysis of polycrystalline thin films and surface regions by X-ray diffraction," *Journal of Applied Crystallography,* vol. 38, pp. 1-29, 2005.
[59] P. Chi Shiang and H. Wensyang, "A microstructure for in situ determination of residual strain," *Microelectromechanical Systems, Journal of,* vol. 8, pp. 200-207, 1999.
[60] E. Fredric*, et al.*, "High-sensitivity surface micromachined structures for internal stress and stress gradient evaluation," *Journal of Micromechanics and Microengineering,* vol. 7, p. 30, 1997.
[61] J. F. L. Goosen*, et al.*, *Transducers,* p. 783, June 7-10 1993.
[62] Z. M. Zhou, "Residual Strains in a Nanometer Thick Cr Film Measured on Micromachined Beams," *Journal of materials science & technology,* vol. 25, p. 77, 2009.
[63] C. Genzel, "X-ray stress analysis in presence of gradients and texture," *International Centre for Diffraction Data,* vol. 44, 2001.
[64] A. Atkinson and S. C. Jain, "Spatially resolved stress analysis using Raman spectroscopy," *Journal of Raman Spectroscopy,* vol. 30, pp. 885-891, 1999.
[65] S. Massl*, et al.*, "A direct method of determining complex depth profiles of residual stresses in thin films on a nanoscale," *Acta Materialia,* vol. 55, pp. 4835-4844, 2007.
[66] W. Fang and J. A. Wickert, "Determining mean and gradient residual stresses in thin films using micromachined cantilevers," *Journal of Micromechanics and Microengineering,* vol. 6, p. 301, 1996.
[67] H. Guckel*, et al.*, "A simple technique for the determination of mechanical strain in thin films with applications to polysilicon," *J. Appl. Phys.,* vol. 57, p. 1671 1985.
[68] W. Fang and J. A. Wickert, "Post buckling of micromachined beams," *Journal of Micromechanics and Microengineering,* vol. 4, p. 116, 1994.
[69] S. M. Carr and M. N. Wybourne, "Elastic instability of nanomechanical beams," *Applied Physics Letters,* vol. 82, pp. 709-711, Feb 2003.
[70] A. T. Vagramyan and Y. S. Petrova, *The mechanical properties of electrolytic deposits*. New York, 1962.

[71] R. Weil, "The origins of stress in electrodeposits," *Plating,* vol. 58, pp. 137-146, 1971.

[72] A. Bhandari*, et al.*, *Microstructural Origins of Saccharin-Induced Stress Reduction in Electrodeposited Ni* vol. 156. Pennington, NJ, ETATS-UNIS: Electrochemical Society, 2009.

[73] J. Matovic, "Application of Ni electroplating techniques towards stress-free microelectromechanical system-based sensors and actuators," *Proceedings of the Institution of Mechanical Engineers, Part C: Journal of Mechanical Engineering Science,* vol. 220, pp. 1645-1654, 2006.

[74] P. T. Tang, "Fabrication of Micro Components by Electrochemical Deposition," 1998.

[75] K. C. Chan*, et al.*, "Effect of reverse pulse current on the internal stress of electroformed nickel," *Journal of Materials Processing Technology,* vol. 63, pp. 819-822, 1997.

[76] A. Mallik and B. C. Ray, "Evolution of Principle and Practice of Electrodeposited Thin Film: A Review on Effect of Temperature and Sonication," *International Journal of Electrochemistry,* vol. 2011, 2011.

[77] S. Yavuz, "Metallic microcantilever resonators: Fabrication and mechanical property measurements," KOC Universiy, İstanbul, 2010.

[78] A. Ozturk, "Development of a diffraction-gratic-based micro-gravimetric sensing method for biologcal applications," KOC University, Istanbul, 2008.